Water Leakage Mapping in Concrete Railway Tunnels using LiDAR Generated Point Clouds

Chad J Hawley

A dissertation submitted in partial fulfilment of the requirements for

the degree of

MASTER OF ENGINEERING (TRANSPORTATION ENGINEERING)

in the

FACULTY OF ENGINEERING, BUILT ENVIRONMENT &
INFORMATION TECHNOLOGY

UNIVERSITY OF PRETORIA

November 2021

SUMMARY

Identifying and Mapping Water Leakage Areas in Underground Tunnels using Intensity Information of Point Clouds

Chad J Hawley

Supervisor: Professor PJ Gräbe

Department: Civil Engineering

University: University of Pretoria

Degree: Master of Engineering (Transportation Engineering)

Light detection and ranging (LiDAR) is a key non-destructive testing (NDT) method used in modern civil engineering inspections and commonly known for its ability to generate high-density coordinated point clouds of scanned environments. In addition to the coordinates of each point an intensity value, highly dependent on the backscattered energy of the laser beam, is recorded. This value has proven to vary largely for different material properties and surfaces.

In this study properties such as surface colour, roughness and state of saturation are reviewed. Different coloured and concrete planar targets were scanned using a mobile LiDAR scanning system to investigate the effect distance, incidence angle and ambient lighting have on targets of differing properties. The study comprised controlled laboratory scans and field surveying of operational concrete railway tunnels. The aim of field tests was to automatically extract water leakage areas, visible on tunnel walls, based on the intensity information of points.

Laboratory results showed that darker coloured targets resulted in a lower recorded intensity value and larger standard deviation of range. Black targets recorded the lowest intensities (0 - 4 units) with 50% higher standard deviations of range, on average, compared to all other coloured targets which recorded standard deviations of around 12 mm. The roughness of each coloured target showed to largely

influence the recorded intensity, with smooth surfaces recording higher standard deviations of measurements.

Concrete targets proved that a difference in roughness and saturation was detectable from intensity data. The biggest change was seen with saturated targets where a 70 to 80 % lower intensity value was recorded, on average, when compared to the same targets in their dry state. The difference in target roughness showed to have no effect on intensity when saturated. The laboratory data provided an important reference for the interpretation and filtering of field point clouds. Ambient lighting had no significant effect on all measurements for both the coloured and concrete targets.

Field tests conducted on an operational concrete railway tunnel confirmed and demonstrated the ability to rapidly identify, extract and record areas of water leakage based on the intensity and spatial information of point cloud data. This is particularly useful as water ingress is known to degrade concrete, resulting in the earlier onset of corrosion, spalling and loss of strength. The mobile LiDAR scanning system used here proved capable of reducing survey time, which would allow for shorter interval revisits, while providing more quantitative information of the leakage areas. Long-term continuous monitoring of the internal structure of a tunnel will reduce the life cycle costs by removing the need for personnel to enter the tunnels for visual assessments and enable remedial work to be better planned by analysing a virtual 3D point cloud of the tunnel before stepping foot onto site.

DECLARATION

I, the undersigned hereby declare that:

- I understand what plagiarism is and I am aware of the University's policy in this regard.

- The work contained in this dissertation is my own original work.

- Where other people's work has been used this has been properly acknowledged and referenced.

- I have not allowed anyone to copy any part of my dissertation.

- I have not previously in its entirety or in part submitted this dissertation at any university for a degree.

Disclaimer:

The work presented in this dissertation is that of the student alone. Students were encouraged to take ownership of their projects and to develop and execute their experiments with limited guidance and assistance. The content of the research does not necessarily represent the views of the supervisor or any staff member of the University of Pretoria, Department of Civil Engineering. The conclusions and recommendations given in the report are also not necessarily that of the supervisor, sponsors or companies involved in the research.

Signature of student:

Name of student: Chad J Hawley

Student number: u16001142

Date: 11 November 2021

Number of words in report: 22 454

ACKNOWLEDGEMENTS

I wish to express my sincere appreciation to the following persons and organisations who made this dissertation possible:

a)   Professor PJ Gräbe, my supervisor. You have always believed in me since the day our paths crossed and for that I'm eternally grateful. Thank you for affording me the opportunity to complete my Masters in a field I'm extremely passionate about. You allowed me to continue with my work at my own pace, making mistakes along the way and in the end producing a report that was purely my own. Your continued guidance, support and constructive feedback helped me get to where I am and present work that I am truly proud of.

b)   To my family and close-friends, I thank you for your encouragement and support during this past year. Getting through the hard times and making a success of this year would have been a lot tougher without you all.

c)   This dissertation is based on research performed at the University of Pretoria. Permission to use the material and equipment is gratefully acknowledged.

d)   Transnet Freight Rail for their generous financial support towards the Chair in Railway Engineering, affording the opportunity for postgraduate railway research.

e)   The following persons are gratefully acknowledged for their assistance during the study:

   i)   Mr A Broekman

   ii)   Mr MH van Schalkwyk

   iii)   Mr M Boswell

f)   The team at Maptek for providing we with a PointStudio suite license for the duration of my Masters and assisting with some basic training.

g)   Mr. Alex Powell, for his assistance in obtaining the necessary permissions and access to the Gautrain tunnels to conduct the field testing.

h)   Mr. Jordan Herrmann, for assisting me in setting up a workflow within Maptek and automating some of the point cloud processes.

i)   Lastly, I'd like to acknowledge and thank the two anonymous reviewers for taking the time to review my dissertation and provide me with valuable comments.

TABLE OF CONTENTS

LIST OF TABLES

LIST OF FIGURES

LIST OF SYMBOLS

P_R	Received signal power
P_T	Transmitted signal power
ρ	Reflectivity of the material
α	Angle of incidence (°)
r	Range from scanner to object surface (m)
η_{Atm}	Atmospheric transmission factor
η_{Sym}	System transmission factor
I	Intensity
C_1	Unknown constant parameter ($\pi P_T \cdot \eta_{Atm} . \eta_{Sys}$)
C_2	Changeable parameter ($\frac{\cos \alpha}{4r^2}$)
Δt	Two-way travel time of a light pulse
c	Speed of light
Q	Pulse energy (J)
PRR	Pulse repetition rate (kHz)
A_L	Laser footprint (cm^2)
Δh	Measure of surface roughness
λ	Laser wavelength (nm)

LIST OF ABBREVIATIONS

LiDAR	Light detection and ranging
NDT	Non-destructive testing
GPS	Global positioning system
4IR	Fourth industrial revolution
MOS	Minimum operational standards
SHM	Structural health monitoring
CV	Computer vision
IP	Image processing
BIM	Building information model
PDI	Periodic detailed inspection
IDI	Initial detailed inspection
UAV	Unmanned aerial vehicle
IoT	Internet of Things
RC	Reinforced concrete
GPR	Ground penetrating radar
IRT	Infrared thermography
SfM	Structure from motion
TLS	Terrestrial laser scanner
PRR	Pulse repetition rate
TOF	Time of flight
NIR	Near-infrared
OSHA	Occupational Safety and Health Administration
MPE	Maximum permissible exposure
MSE	Mean square error
USD	United States dollar
UV	Ultraviolet
IR	Infrared
PS	Phase-shift
RMSE	Root mean square error
SLAM	Simultaneous localization and mapping
IMU	Inertial measurement unit
DOF	Degree of freedom
CA	Californian
FOV	Field of view

MBL	Multi-beam lidar
RMBL	Rotating multi-beam lidar
RGB	Red, green, blue
MB	Megabyte
GB	Gigabyte
USB	Universal serial bus
CAD	Computer aided design

1   INTRODUCTION

1.1   BACKGROUND

Railway tunnels are key pieces of infrastructure. They improve connectivity, efficiency and enhance the capabilities of the transportation sector (Puente et al., 2016). In an ever-expanding world where space is a premium, underground transportation networks are fast becoming more common practice in a bid to alleviate traffic congestion (Huang et al., 2018).

Tunnels do however present a maintenance challenge as they need to be inspected regularly to avoid costly incidents and ensure safe train operations (Zan et al., 2016). Tunnelling projects are also generally more costly than the construction of bridges and the life cycle of these assets should therefore be extended for as long as possible (Puente et al., 2016). The consequences of incidents in a tunnel are notably more severe, given the confined environment, compared to an open roadway (Leingartner et al., 2016). The need for operational performance on all aspects from lighting and ventilation to drainage and clearance need to be monitored constantly. One of the greatest problems facing tunnels is the infiltration of water through the tunnel lining (Dawood et al., 2020). This infiltration not only leads to drainage issues but also accelerates the degradation of the concrete lining the tunnel walls. The infiltration of water through cracks leads to corrosion of rebar, spalling and water voids, all of which compromise the structural integrity of the tunnel and increase user risk (Dawood et al., 2020).

Conventional assessments of concrete tunnels are based on visual inspections. These assessments are however time consuming, require lengthy track occupation and rely heavily on the interpretation of the assessor (Dawood et al., 2020). With a large number of infrastructure assets currently requiring regular monitoring and maintenance, and with this number constantly on the rise, a more cost-effective surveying method is required. A list of NDT methods compiled for infrastructure monitoring was reviewed to assess their applicability for tunnel monitoring (Gastineau et al., 2009). Light detection and ranging (LiDAR) was noted as one of the methods that is fast expanding and becoming an essential tool for accurate non-destructive 3D measurement of structures (Mosalam et al., 2014). This method will be the focus of the research and assessed for its application to tunnel monitoring.

LiDAR technology is commonly used for range estimates, modelling of external geometry, clearance calculations and the generation of 3D point clouds of scanned environments. In addition to the (x, y, z) coordinate information, most systems simultaneously record a radiometric value termed 'intensity'. This value is loosely defined as the strength of the backscattered energy from any given point and is influenced by the physiochemical properties

of the scanned surface. Intensity information has shown to benefit a number of used cases; damage evaluations (Chen et al., 2013), segmentation (Tatoglu & Pochiraju, 2012), classification (Arastounia, 2012), moisture detection (Suchocki et al., 2018) and even surface moisture quantification on sandy beaches (Jin et al., 2020). An advantage of 3D point clouds generated from this method is that they can be stored and viewed off-site by engineers, saving time and allowing multiple inspections to be carried out within a single day. Having a record of each scan provides engineers with the opportunity to refer to previous scans if information was missed or just simply to compare two scans from different epochs and assess any changes. Recent improvements in accuracy, precision and mobility of these instruments have seen their application grow and spread to all sectors, not only engineering.

Hovermap, a specific mobile laser scanning unit developed by Emesent, an Australian based company, will be the focus of this research. The compact, lightweight and durable design of the Hovermap system has seen it become a global leader in underground mobile mapping with the capability of fully autonomous flights in GPS-denied environments. The Emesent Hovermap system is equipped with a Velodyne VLP-16 LiDAR puck with specifications published by Emesent (2020). Studies that have assessed different aspects of the Velodyne VLP-16 have been carried out by various authors (Glennie et al., 2016; Kidd, 2017; Péntek et al., 2018; Bula et al., 2020). However, none report on the performance of the Hovermap system and VLP-16 LiDAR as an integrated unit.

In an attempt to maximise the overall benefit of an inspection, a good understanding of the scanner system and its deliverables is essential. The response of the LiDAR to surfaces of different colour, roughness and wetness, along with the distance and incidence angle the surfaces are viewed at, need to be fully understood to prevent the redo of scans and extract as much meaningful data as possible during each inspection.

1.2   OBJECTIVES OF THE STUDY

The main objective of this study was to assess the capability of the Hovermap LiDAR system for remote sensing and monitoring of water leakage areas in concrete railway tunnels. Activities were carried out to meet the following study objectives:

- To determine/quantify the effects distance, incidence angle and lighting have on range accuracy, intensity and data density of point clouds of different coloured targets.

I To review and investigate the change in recorded intensity information for various concrete surfaces with different degrees of roughness and states of saturation.

I To demonstrate the ability to automatically identify and extract quantitative water leakage information based on intensity data alone for a section of an operational railway tunnel.

Results of this study will aid in practical applications to better select scanning positions and improve the overall efficiency of data acquisition. Detecting water leakages from point cloud data will eliminate the need for personnel to enter tunnels and obtain such information through a visual assessment, which is both time consuming and only produces qualitative information of the location of each leak. In addition, the results of the study will assist general land surveyors in understanding Hovermap's capabilities and limitations based on object surface properties and how this may influence the accuracy of measurements.

1.3   SCOPE OF THE STUDY

The focus of the study was to investigate the ability of the Hovermap LiDAR system to be used as a primary tunnel monitoring and water leakage mapping tool.

The 3D scan pattern distribution of the point cloud collected with the Hovermap system was reviewed to identify blind spots. Further work included the collection of point clouds of different coloured and concrete targets at different distances and incidence angles to assess the effect colour, reflectance and roughness had on the returned signal. The experimental focus was on the recorded intensity information and the effect degree of saturation had on this. The influence of ambient lighting was also observed for all scans. Distances of up to 6 m and incidence angles from 0° to 45° were considered.

Field experiments were conducted to assess the feasibility of implementing such a mobile laser scanner with the aim of reducing surveying time and identifying and extracting quantitative information of water leakage areas in concrete railway tunnels. The study was only concerned with water leaks on the tunnel walls. Pooling of water on the floors was not considered as it was not the source of water ingress but rather the run-off from leaks on the tunnel walls.

1.4   METHODOLOGY

The methodology that was followed is described below:

- A literature review was conducted to investigate the challenges associated with tunnel maintenance and the NDT methods used to identify defected areas. Properties of different surfaces are then reviewed with the Chapter concluding with information on the Hovermap LiDAR system and associated specifications and published works.

- The equipment, components and different target surfaces needed for the testing were collected, manufactured or obtained from suppliers.

- Testing and data collection of different target surfaces were conducted in a controlled laboratory environment.

- Field surveys were conducted on sections of an operational concrete railway tunnel to verify laboratory results.

- All processing of point cloud data was carried out off site.

- The data was analysed, results discussed and conclusions drawn.

1.5   ORGANISATION OF REPORT

This dissertation consists of the following Chapters:

- Chapter 1 serves as an introduction to the dissertation, outlining the objectives, scope, methodology and organisation of the dissertation.

- Chapter 2 contains the literature study which serves as a technical introduction and review of past research conducted as guidance for this study.

- Chapter 3 describes the experimental setup of targets, scanning equipment and the full testing procedure from scanning to data retrieval and analysis.

- Chapter 4 presents and discusses the results obtained during the study.

- Chapter 5 includes the conclusions that were reached and provides recommendations for future studies.

- A list of references is included at the end of the dissertation.

2   LITERATURE REVIEW

An in-depth literature study was prepared on railway tunnel maintenance and the current available condition monitoring practices. A brief introduction to the current maintenance strategies of railways is discussed, with emphasis on time and scale of monitoring practices. This is followed by a summary of deterioration mechanisms that commonly affect concrete structural elements and how water infiltration affects these areas. A list of available NDT methodologies is presented, with emphasis on LiDAR and focused on the Velodyne VLP-16. The properties and reflectiveness of different materials are reviewed, addressing aspects of colour, roughness, material type and degree of saturation. A description of the Emesent Hovermap system, equipped with a VLP-16 LiDAR device, then follows and forms the centre of the research. The future of digital twinning and remote monitoring is briefly discussed, with the section concluding with a summary of the reviewed literature.

2.1   RAILWAY MAINTENANCE

The past decade has seen major changes in the way railway infrastructure is managed in comparison to preceding centuries (Zoeteman, 2001; Kasireddy et al., 2020). The onset of the fourth industrial revolution (4IR) has introduced technological advances that make otherwise time-consuming tasks more efficient and cost-effective. This has afforded engineers and maintenance personnel the opportunity to carry out maintenance work more frequently, with a higher level of accuracy. In some cases, work has been done remotely, eliminating the need to set foot on site.

The world's growing population is placing an increasing demand on the transportation sector. Coupled with ageing infrastructure and limited funds to completely reconstruct, maintenance of existing infrastructure has become an important topic of interest. Minimum operating standards (MOS) must be met despite limited track occupation time available for maintenance activities (Kumar et al., 2006). The response of railway maintenance managers to this issue has been the development of NDT and computer-based tools that assist in the continuous long-term monitoring of these key infrastructure assets. These tools aim to assist decision makers to coordinate maintenance operations in a timely fashion while still meeting the MOS and remaining in budget. Despite efforts to reduce costs, a substantial amount of railway budgets is spent on inspection and maintenance. The outdated means by which these activities are carried out create additional costs, which are then further inflated by poor logistical decisions, inadequate equipment and mediocre planning (Kumar et al., 2006).

2.1.1 Costs

The management of rail traffic during inspections is becoming increasingly challenging as lines are being operated at higher capacity with faster trains and for longer hours. The maintenance window is becoming progressively smaller, and most inspections must be carried out in the early hours of the morning when traffic is least and train operations can be halted.

The importance of railway infrastructure maintenance is crucial for a well-functioning transportation system. The actual maintenance of railways consists of an extensive number of activities carried out by workers, inspectors and engineers who combine their knowledge and skills to ensure safe train operations. However, these activities are costly and require considerable resources and large budgets (Lidén, 2015; Wang, 2018). Lidén (2015) reported that European countries allocate, on average, 15 to 25 billion euros annually for railway maintenance and rehabilitation. With a network consisting of roughly 300,000 km of track, this amounts to approximately 700,000 euros per track km per year.

Although network growth is needed to generate increased revenue, this growth places increased pressure on the teams that inspect and maintain the existing network. A larger network means more teams are required, thus increasing the cost of maintenance. Investment into cost-effective technologies that can assist in monitoring various parts of the network is essential to sustain and promote continued growth.

2.1.2 Ageing infrastructure

The transportation infrastructure sector is ageing and, with limited funding for maintenance and preservation, keeping these infrastructure segments in operation is challenging (Allen et al., 2015). Increasing populations in urban areas have resulted in a reduction in available land for capacity expansion. Engineers' response to this has been to design and construct complex tunnel systems to keep up with demand and improve mobility. Unlike bridges which occupy available land, underground tunnelling is the ideal means of improving mobility. Reducing transport distances and relieving urban traffic congestion are its main advantages (Xu et al., 2018). The primary disadvantage, however, is the cost of these key pieces of infrastructure, which are generally far more expensive than the construction of bridges (Puente et al., 2016).

The past few decades have seen many major cities around the world conduct extensive tunnelling projects due to limited space and the need to use it more effectively (Attard et al., 2018). Continuous monitoring of deterioration within these tunnels is essential to extend their life cycles and prevent collapse from occurring. Fortunately, this task is being made easier by modern technological advances.

2.2   MAINTENANCE OPERATIONS AND INSPECTIONS

Traditional methods of inspection relied heavily on visual assessment and fixed sensing equipment that required installation (Hoult & Soga, 2014). Manual inspections of the condition of infrastructure elements are not only time consuming and expensive, but subject to human error with some locations too dangerous or too difficult to reach (Frangopol & Tsompanakis, 2014; Attard et al., 2018; Dawood et al., 2020). The ever-expanding network means that infrastructure managers are under pressure to maintain and keep records of these pieces of infrastructure in a more cost-effective manner.

A possible solution comes in the form of structural health monitoring (SHM) systems (Gastineau et al., 2009). These systems apply a variety of different tools, scanners, photogrammetry and computer vision (CV) techniques, depending on the environment, to achieve surveying goals (Attard et al., 2018; Su et al., 2019). The effectiveness of these systems rests heavily on the efficiency and accuracy of the equipment to provide maintenance managers with the necessary information required. The skill and experience of inspectors are also important as errors in inspections are often costly and error reduction is challenging (Menendez et al., 2018).

Utilizing image processing (IP) and the generation of 3D point clouds have proven to assist in the monitoring and creation of building information models (BIM), as seen in work published by Ariyachandra and Brilakis (2020), Huang et al. (2020) and Xue et al. (2020). Having access to a 3D digital twin of the current condition of an infrastructure asset will improve asset inventory management and reduce inspection errors by providing a more complete picture of the asset (Menendez et al., 2018).

2.2.1   Time frame and scale

The monitoring of civil engineering structures includes all controls and inspections done throughout the life cycle of the asset. These are done to reveal any changes from the asset's reference in terms of as-built and current state (CETU, 2015). The time frame and scale of SHM are necessary considerations that need addressing before choosing the type of monitoring system (Gastineau et al., 2009). Most new tunnel structures are built with the intention of lasting over 50 years and therefore require long-term monitoring solutions. However, the monitoring frequency may change and is usually linked to particular events in the life cycle of the structure. These may be continuous, periodic or even once-off (CETU, 2015):

- Continuous:
    - o   Monitoring requires regular recording of defects and abnormalities.

- Periodic:
  - o Annual inspections and assessment visits
  - o Periodic detailed inspections (PDI)
  - o Detailed inspection of parts of the structure.
- Once-off:
  - o Initial detailed inspection (IDI)
  - o Inspection at end of contractual guarantee
  - o Unforeseen events.

The scale of the monitoring is also important as this influences the time necessary for inspections to be carried out. This can be subdivided into three sections (Gastineau et al., 2009):

- Local:
  - o Focus is on a specific location. This may be to assess the growth of a known crack or specific abnormality, or where previous remedial work has been carried out.
- Member:
  - o Focus is on a specific member or region where a problem such as excessive deformation has been identified, or in an area of high-water leakage.
- Global:
  - o Focus is on the overall health of the infrastructure. This is good for tracking long-term changes. Infrastructure report cards are based on this metric.

It is important to know what you are looking for and how to look for it when performing inspections. Primarily observation- and description-based inspections compare deterioration and defects through visual appearance. Additional subsurface information may be required and gathered in areas showing signs of visual deterioration, but this comes at an additional cost (CETU, 2015). It is essential to have a well-kept record of inspections from the end of construction to date for maintenance managers and engineers to refer to and track changes.

2.2.2 Current practice

The current practice for infrastructure maintenance, health and progress monitoring varies across disciplines. Recent advances in unmanned aerial vehicles (UAVs) have unlocked new possibilities that enable low-cost acquisition of high-resolution spatial data with customised revisit times (Javadnejad, 2017). A study published by Flammini et al. (2016) discussed the application of drones for the monitoring of railway infrastructure. Figure 2.1 demonstrates some of the areas where drones may be used effectively to monitor the railway environment.
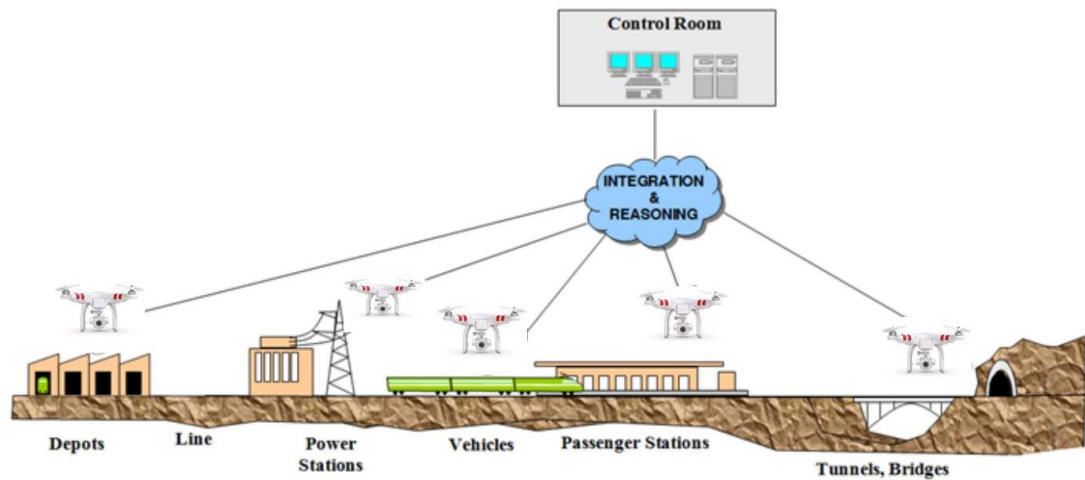
Figure 2.1: Drone-based monitoring of railway infrastructure (Flammini et al., 2016)

Depending on the size and type of drone, payloads of up to 2.5 kg may be carried onboard. This enables the integration of sensors and scanners with different and diverse functionalities to be mounted on the drone for monitoring purposes. Baylis et al. (2020) discussed the use of mobile drone LiDAR for structural data collection. In the future, advancements in smart maintenance and the Internet of Things (IoT) will reduce the need for human intervention, enabling quicker, safer and more frequent inspections to be carried out (Flammini et al., 2016).

2.3 DEFECTS ON CONCRETE STRUCTURAL ELEMENTS IN RAILWAY TUNNELS

Concrete supports the construction of many major infrastructure assets and has been the most widely used building material since the 1950s (Valença et al., 2014). Valença et al. (2014) emphasise the exponential increase in the costs of concrete rehabilitation with time, and that predicting reinforced concrete (RC) structure degradation is extremely important to preserve its functionality. This chapter discusses the term deterioration and some of its most common forms found in RC tunnels.

The term 'deterioration' describes a problem that affects part of a structure and manifests gradually or suddenly. Deterioration is often caused by changes in material properties, behaviour of the surrounding ground, water ingress, pollution, or unfavourable faults stemming from poor workmanship. Signs of deterioration should be identified as soon as possible to avoid catastrophic and costly collapse (CETU, 2015). Some examples of deterioration include:

- Appearance of cracks and deformation
- Changes in mortar, scaling and spalling
- Appearance of water ingress and change in flow rate.

The type and rate of deterioration changes with time, depending on the location of the defect and whether previous remedial action has taken place. Understanding and tracking these long-term changes will help to extend the life cycle of infrastructure and better direct funds for more effective maintenance and repair.

2.3.1 Water leakage through tunnel linings

It can be argued that the building of the tunnel lining is the most important stage in the construction of a tunnel structure. An inadequate waterproof lining or substandard thickness has proven to result in early deterioration and can lead to serious accidents (Zan et al., 2016; Huang et al., 2018). The majority of tunnel linings are built using RC or shotcrete and the most common visible defects are cracks, spalling and water ingress (Menendez et al., 2018). The infiltration of water through this lining is a serious problem and, when coupled with other defects, leads to accelerated deterioration which compromises the structural integrity of tunnels (Suchocki et al., 2018; Xu et al., 2018; Dawood et al., 2020). Identifying and monitoring areas of leakage in tunnels are therefore vital to protect the structure successfully. Remedial work must be initiated timeously and changes tracked to optimise interventions (Valença et al., 2017). An example of a damaged tunnel lining with extensive water leakage is shown in Figure 2.2.

Figure 2.2: Damaged tunnel lining with extensive water leakage

Attention to waterproofing should be given where multiple joints are present. The effectiveness of the waterproof lining depends on the following factors (Huang et al., 2018):

- Permeability and thickness of the concrete
- Effectiveness of the joint sealer and waterproof lining
- Watertightness around the bolts
- Permeability of the connection between the tunnel and station.

Human factors such as improper installation of sealing material are also a cause of water ingress. Detection of water leaks is one of the most important tasks of regular inspections and is fortunately made easier through methods that integrate different tools and image processing (Attard et al., 2018; Xu et al., 2018; Yu et al., 2018; Dawood et al., 2020; Huang et al., 2020).

2.3.2 Differential settlement

Work done by Hu et al. (2018) concluded that irregular differential settlement resulted in structural damage and leakage on and around joints, with an increase in spalling at these locations. A potential threat to safety and train operations is posed when settlement or deformation of the tunnel floor or wall becomes excessively large. Continuous monitoring of tunnels should be done to compare results to previous surveys and to the as-built data to check for any variations.

Previous detection methods used a device known as a profilometer. This was moved over a concrete surface to measure elevations of the surface for comparison with as-built elevations. Apart from being extremely time consuming, this method required direct access to the concrete surface. It was often unsafe since climbing to perform bridge inspections or entering hazardous tunnels was the only available means by which this inspection could be undertaken (Kim et al., 2015). Today, more advanced devices can provide larger amounts of data while saving time and eliminating the need for personnel to enter dangerous spaces.

An extensive record of tunnel inspections should be kept. This should include measurements of as-built dimensions together with the internal state of the tunnel lining and the lining thickness at the time the tunnel was under construction and while in service (Puente et al., 2016). Gathering this information would not be possible without advanced scanners that can capture point clouds of large areas and save a digital twin of the area in a matter of minutes. Having access to such records is important for calculating clearances, monitoring deformation, marking areas of water ingress and detecting differential settlement. A full record of 3D point clouds of a tunnel at various epochs would allow infrastructure managers to change easily between the different inspections and observe the changes in real-time.

2.4 NON-DESTRUCTIVE TESTING (NDT) METHODS

Current infrastructure inspections are performed through periodic visual evaluations by trained inspectors. These assessments aim to document structural defects such as cracks, water infiltration, spalling and exposed rebar, and compare these observations with previous surveys (Attard et al., 2018). The growing number of infrastructure assets being built each year means traditional visual evaluations are fast becoming outdated. More cost-effective and accurate data-capturing systems are required. It is important that these assessments are non-invasive, which means NDT methods are commonly used. Some of the most common methods include:

- Visual inspection
- Photogrammetry
- Ultrasound
- Ground penetrating radar (GPR)
- Light detection and ranging (LiDAR)
- Infrared thermography (IRT)

These NDT tools aid in the detection of deterioration at early stages which affords engineers and inspectors the opportunity to prioritise maintenance and repair efforts. The current and future trends of NDT for building diagnosis were studied by Flohrer (2010).

Previous drawbacks of some of these methods related to their application to tunnel inspections and the considerable amount of cost and time needed to complete scans (Attard et al., 2018). The latter is no longer a problem due to advanced scanners and equipment mobility. However, various problems, relating to tunnel inspections, emerged which required personnel to access tunnels that could be hazardous, characterised by dust, inadequate lighting and ventilation and present possible traces of toxic substances (Flohrer, 2010; Attard et al., 2018; Menendez et al., 2018). The advancement of UAVs and the small compact size of modern-day mobile scanners open up a new realm of possibilities that will eventually eliminate the need for personnel to enter tunnels to conduct inspections (Javadnejad et al., 2019).

Each of the methods listed above require trained personnel and specialised equipment. The information obtained by performing each of these NDT methods differ, with main evaluation categories for a basic concrete wall summarised in Figure 2.3. A more detailed discussion of each method follows.
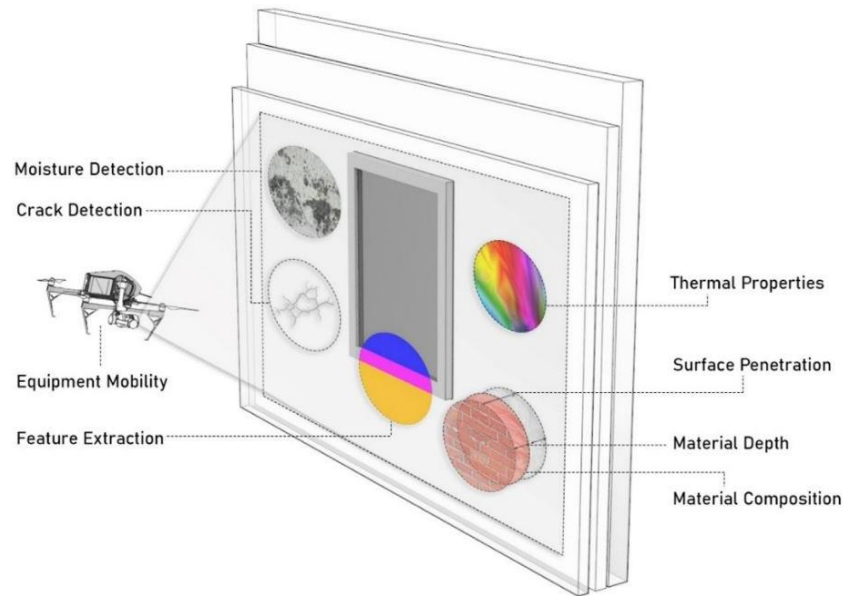
Figure 2.3: NDT evaluation categories (El Masri & Rakha, 2020)

Visual inspection

Visual inspections are traditionally carried out on a routine, detailed or specialised basis. Visual assessment of concrete infrastructure is done to identify signs of damage and deterioration; however, lighting in tunnels is normally inadequate to allow for accurate observations (CETU, 2015). Figure 2.4 shows how additional lighting is used to aid manual visual assessments of tunnels. The person undertaking the inspection records all signs of deterioration and damage by drawing a detailed sketch of the affected area, supplemented by notes and annotations.

Figure 2.4: Visual assessment with additional lighting (CETU, 2015)

This is the most basic form of structural monitoring, which is both extremely time consuming and subject to human error. Visual inspections still have their place; however, alternative NDT methods are preferred for widespread monitoring of tunnel networks and repeatability of measurements.

Photogrammetry

Photogrammetry is used to recreate accurate 3D models of infrastructure through analysis of 2D images (El Masri & Rakha, 2020). Despite the inability of this method to detect subsurface defects, thermal properties and moisture changes, it does prove useful for feature extraction.

A new photogrammetric approach known as structure from motion (SfM) has been used in the generation of high-resolution maps where adequate lighting is available (Javadnejad et al., 2019). Figure 2.5 shows the general steps for SfM photogrammetry.
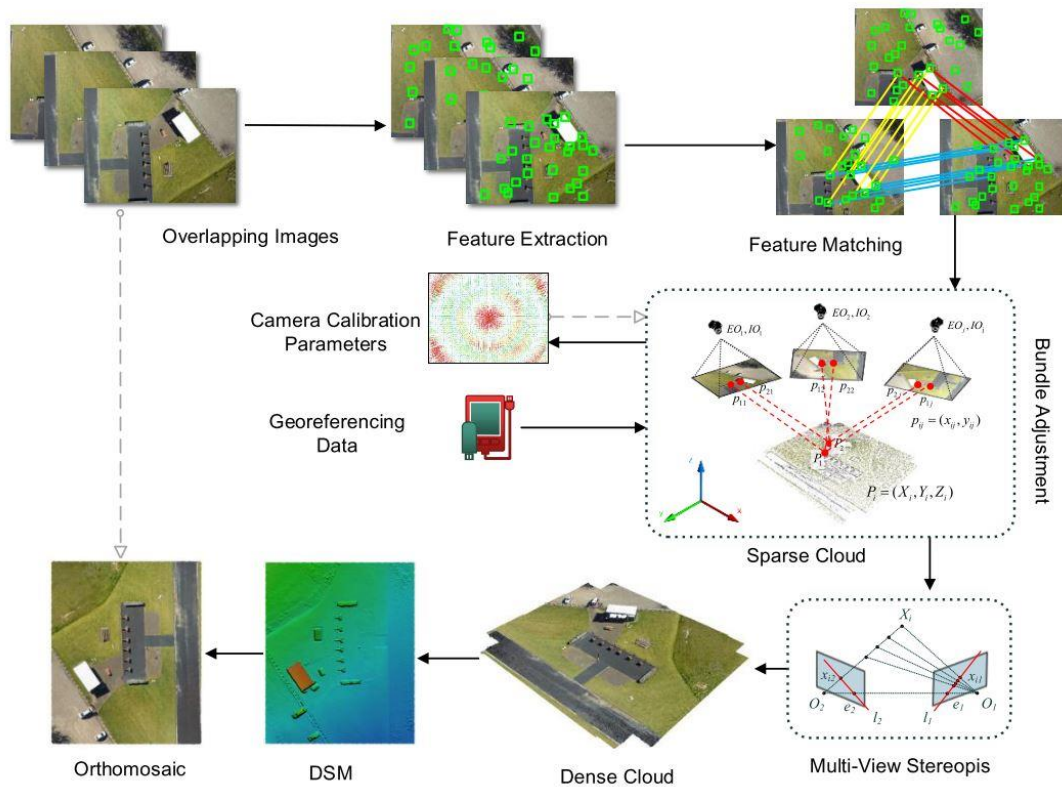
Figure 2.5: SfM photogrammetry workflow (Javadnejad et al., 2019)

This method of inspection has been used in several applications in civil engineering (Valença et al., 2017; Attard et al., 2018; El Masri & Rakha, 2020). Huang et al. (2020) demonstrated

the ability to identify and quantify areas of damage in tunnel linings using a combination of photogrammetry, point cloud data and machine learning. A drawback of this method is that it works in a passive way, relying on external illumination of the surface under inspection (Xu et al., 2018). In sections where lighting is insufficient, tunnels cease to benefit from this form of monitoring unless external illumination is provided.

Ultrasound

This NDT technique utilises short wavelengths to conduct detailed assessments of internal characteristics of concrete structures. The ability to locate voids and corrosion in a single test makes this technique attractive. However, it is limited for feature extraction, thermal properties and moisture detection (El Masri & Rakha, 2020). Analysis of the two-dimensional scanned data can sometimes prove challenging, which is why this method has been used mainly for rail head inspections (Gastineau et al., 2009). Figure 2.6 shows a handheld ultrasound scanner being used for a railhead inspection.

Figure 2.6: Ultrasound railhead testing (Pandrol, 2020)

Ground penetrating radar (GPR)

Ground penetrating radar utilises electromagnetic waves to conduct subsurface inspections. The device transmits an electromagnetic wave, measuring and analysing the reflected signal to locate objects hidden below ground and out of sight. This technology is used extensively by civil engineers to locate utility mains, identify existing infrastructure and inspect rebar positioning within cast concrete structures such as bridges and tunnels (Zan et al., 2016; El

Masri & Rakha, 2020). The speed at which data can be collected, either manually or fixed to a vehicle for increased data collection, makes this NDT method advantageous. A disadvantage is that scans are not interpreted as easily and require expert knowledge and experience to extract meaningful data. Figure 2.7 displays a typical example of the expected output from a GPR scan. Figure 2.8 shows a typical vehicle-mounted and handheld GPR setup.
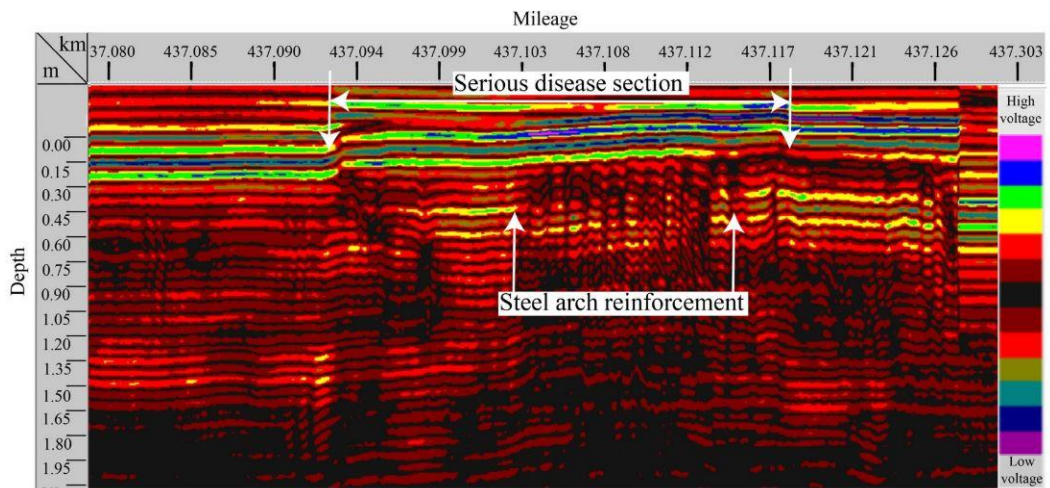
Figure 2.7: Expected data from a GPR scan of a concrete arch (Zan et al., 2016)
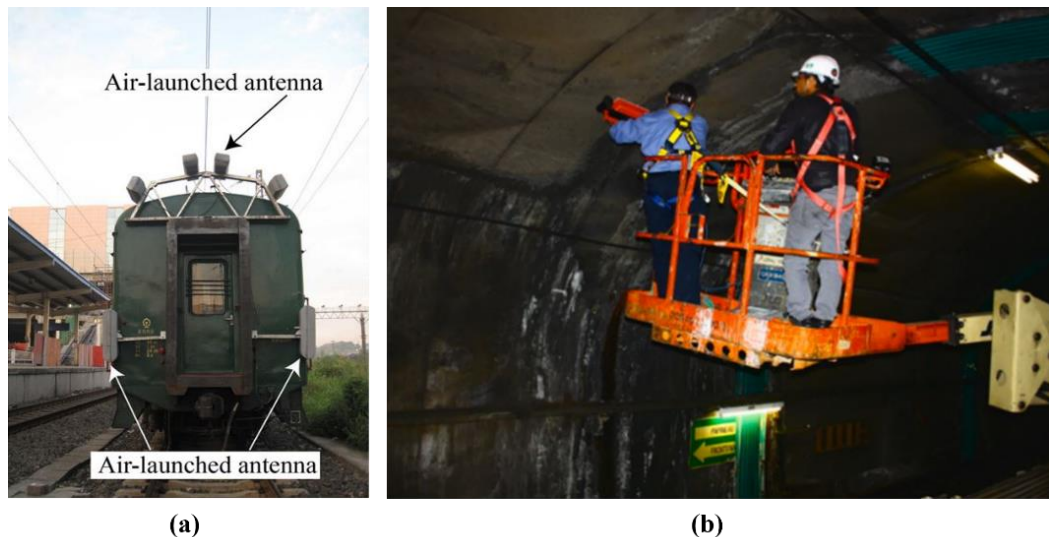
Figure 2.8: (a) Vehicle-mounted (Zan et al., 2016) and b) handheld GPR scans (Dawood et al., 2020)

Light detection and ranging (LiDAR)

LiDAR is an active system, transmitting an electromagnetic pulse of energy in the form of a light beam which indicates it is independent of external illumination, unlike photogrammetry (Wehr, 2008; Kidd, 2016). The scanner's laser source then uses either time for the emitted pulse to reflect off a surface and back to the scanner, or the peak amplitude phase difference from the reflected light to measure distance to a point (Gastineau et al., 2009). This distance information is used to create 3D point clouds of the scanned environment in a fraction of the time compared to traditional surveying methods. LiDAR scanners have shown sufficient applicability and superiority in surficial infrastructure inspections (Puente et al., 2013; Tan et al., 2016). In addition to collecting (x, y, z) coordinates of each point, the system also records intensity which is a radiometric value strongly related to the physiochemical properties of the scanned surface.

The advantages and disadvantages of LiDAR scanners vary, depending on the scanner type, the environment in which the scan is conducted and the offered accuracy. Contingent on the application, different scanners may be more suited than others, even though the latter may be more accurate and have a denser point cloud. The most common advantages and disadvantages of LiDAR are listed below:

Advantages

- 3D point clouds can be archived and processed off-line at a later stage
- Provides non-destructive, accurate and extensive data capture of a given study area
- Feature extraction, segmentation and physical defect identification have proven possible with the additional intensity information (Kashani et al., 2015).

Disadvantages

- Wide range of available laser scanners requires users to know their intended purpose
- Care must be taken when operating in rainy or hazy weather conditions due to the laser penetration (Azman et al., 2015)
- Cannot penetrate solid surfaces to provide material depth and composition information.

Figure 2.9 shows a typical point cloud of a railway tunnel coloured by intensity. This point cloud contains over 10 million points and was mapped in under 2 minutes.
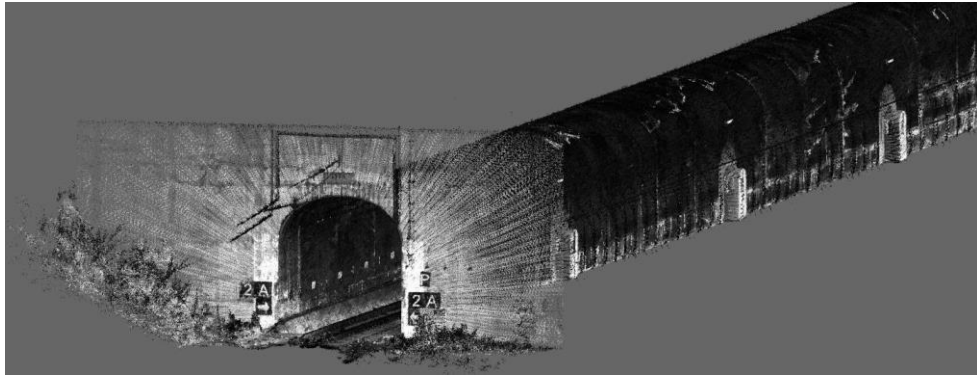
Figure 2.9: 3D point cloud of railway tunnel coloured by intensity

Infrared thermography (IRT)

IRT technology works in the invisible spectrum range. It measures radiation emitted or reflected off surfaces and displays this image as a spectrum (El Masri & Rakha, 2020). This technique is dependent on the emissivity of surfaces and is not effective, on its own, for identifying subsurface components. Janků et al. (2019) conducted a study that compared IRT with other NDT methods to identify delaminations in concrete.

Compared to other NDT methods, this method is more adversely affected by weather and surrounding conditions. This was noted in its application for tunnel monitoring where the temperature gradient is smaller, therefore requiring a sensor with a very high resolution and sensitivity to identify areas of moisture ingress (Konishi et al., 2016; Yu et al., 2018; Lu et al., 2019). A comparison between visible and infrared imagery is shown in Figure 2.10.
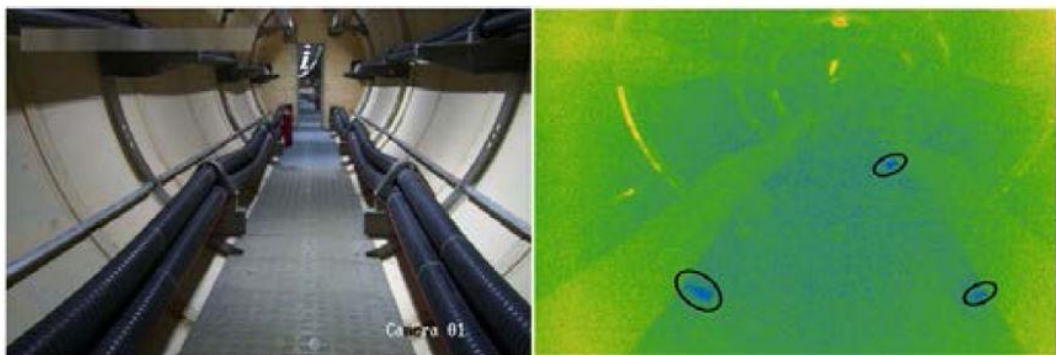
Figure 2.10: Visible and infrared image of a tunnel lining (Lu et al., 2019)

Figure 2.11 summarises some of the available NDT methods listed above and where they are best suited. A direct, indirect or no relevant literature score describes the NDT technique as, respectively, being relevant and practical, lacking literature backing, or showing a clear gap but no clarification as to whether the gap is as a result of technological limitations. Summaries like this assist in identifying areas that require research.
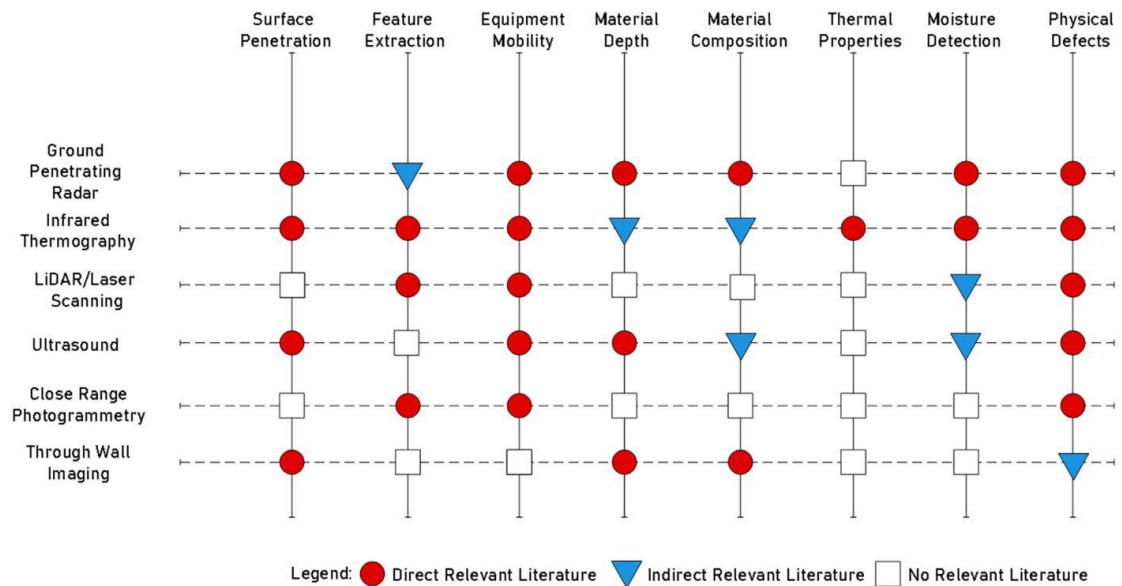
Figure 2.11: Capabilities of NDT techniques and hybrid workflow identification (El Masri & Rakha, 2020)

The most common and popular NDT methods are those associated with structural safety checks. LiDAR is one such method that is gaining widespread popularity and fast becoming an essential tool for accurate 3D measurements of structures (Mosalam et al., 2014).

2.5 LIGHT DETECTION AND RANGING (LiDAR)

Before describing the performance and specifications of the Hovermap system, a brief background of LiDAR is given. This is followed by an overview of the basic principles, the information captured for each point and applications utilising such information. Only pulse lasers are considered herein, with particular attention given to the Velodyne VLP-16 LiDAR.

2.5.1 Historical background of LiDAR

Just like sonar uses sound and radar uses radio waves to map surfaces, LiDAR uses light emitted in the form of a laser beam. LiDAR was initially a tool developed for military purposes in the 1960s for submarine detection from aircrafts. The primary function was to actively measure distance from the sensor to the target object. The last few decades have seen the interest in LiDAR grow beyond its initial intended purpose. This is the result of increased research and understanding of its capabilities (Azman et al., 2015). Today it has applications across a wide range of industries, namely construction (Kim et al., 2020), agriculture (Nakano et al., 2020), forestry (Azman et al., 2015), disaster management (Leingartner et al., 2016), reverse engineering (Mosalam et al., 2014), object detection (Ma et al., 2018), asset inventory (Leslar et al., 2010), underground mining (Jones, 2020), planar surface segmentation (Wang & Lu, 2009) and as-built model generation (Arastounia, 2016).

Three types of LiDARs are available, namely topographic, bathymetric and terrestrial. Topographic LiDAR is used mainly to map land surfaces using near-infrared light, while bathymetric LiDAR makes use of its water-penetrating green light to measure and map sea and riverbeds. Topographic LiDAR, also referred to as a terrestrial laser scanner (TLS), is the most common type, typically used to conduct close range scans over ranges between 0 and 200 m (Wehr, 2008). TLSs have become the most popular means of 3D point cloud acquisition in civil engineering (Suchocki et al., 2020)

2.5.2 Basic theory

LiDAR is based on the active transmission of laser beams. These beams are reflected and scattered off surfaces, enabling part of the return signal to be captured by the receiver. Equation 2.1 is the basic 'laser equation' which describes the relationship between a transmitted and received signal (Suchocki et al., 2020). The equation assumes that the target surface is rough (Lambertian scattering) and always larger than the area of the laser spot (Pfeifer et al., 2008).

$$P_R = \frac{\pi \, P_T \, \rho \, \cos \alpha}{4 r^2} \, \eta_{Atm} \cdot \eta_{Sym} \qquad (2.1)$$

where: P_R is the received signal power

P_T is the transmitted signal power

ρ is the reflectivity of the material

α is the angle of incidence

r is the range from scanner to object surface

η_{Atm} is the atmospheric transmission factor

η_{Sym} is the system transmission factor.

Point data information

Different scanners collect data at different rates, but the information pertaining to each point is often similar. From the received signal power, TLSs automatically conduct measurements of distance and vertical and horizontal angle (Suchocki et al., 2020). Based on this information, point coordinates are calculated and used to construct a 3D point cloud of the scanned environment. In addition, radiometric information (intensity) based on the amount of energy reflected off a surface back to the receiver is recorded. Figure 2.12 shows a schematic of the geometric and intensity data collected for each point.
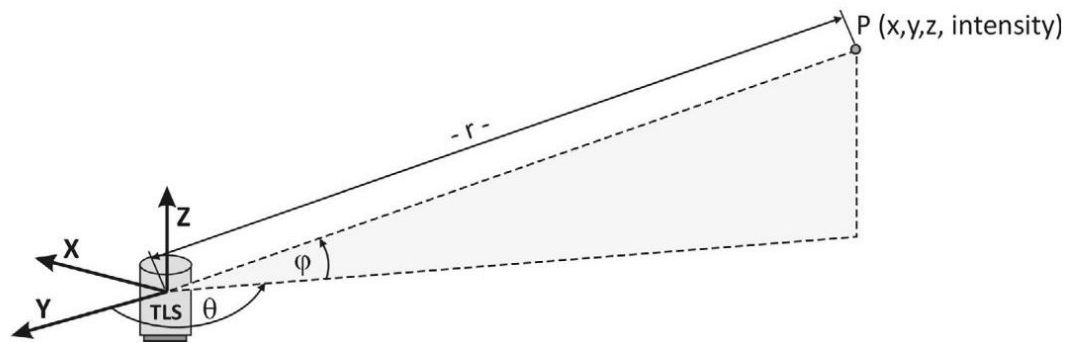
Figure 2.12: Point data collection (Suchocki & Katzer, 2016)

Equation 2.1 shows that the power of the received signal is dependent on multiple factors, of which some remain constant and others change during different scans. The power of the transmitter (P_T) is a term that can be regarded as constant if the same scanner is used (Suchocki et al., 2017). The same applies to the system transmission factor (η_{Sym}), which is usually unknown to the average user but is associated with the technical specifications of the scanner. If the same scanner is used for all scans, this term can also be considered constant. Suchocki et al. (2017) noted that scans conducted indoors and outdoors are usually either under stable conditions or very quick so the atmospheric effect (η_{Atm}) is negligible and to can be considered constant. However, care must be taken when conducting scans during rainfall events as results show these might have adverse effects (Filgueira et al., 2017).

Other factors such as reflectance (ρ), angle of incidence (α) and range (r) often vary between scans. The influence of these different factors on point clouds has been investigated by several researchers (Kukko et al., 2008; Voegtle & Wakaluk, 2009; Kaasalainen et al., 2011; Blaskow & Schneider, 2014; Tan & Cheng, 2016; Bolkas & Martinez, 2017). Kaasalainen et al. (2011) discussed possible empirical correction methods that could be applied during the post processing of data to eliminate or minimise the influence that range and incidence angle had on intensity measurements. Of the scanners studied, all effects were strongly dependent on the instrument itself. It was concluded that individual scanners be studied, depending on the use case, and adjustments be made accordingly. Kaasalainen et al. (2011) noted that additional research was needed to study the influence surface roughness has on the return intensity. Suchocki et al. (2018) and Suchocki et al. (2020) both claimed that these reflective characteristics were significantly influenced by the degree of saturation of the surface. By selecting or creating a surface with uniform roughness, varying the degree of saturation would be the only changing factor which, in theory, should influence the recorded intensity values.

Taking into account the factors that can be regarded as constant or changeable during each scan, Equation 2.1 can be simplified where intensity is directly proportional to the reflectance of the scanned surface. Equation 2.2 shows a simplified version of Equation 2.1.

$$I = \rho \cdot C_1 \cdot C_2 \tag{2.2}$$

where: I is the measured intensity value

ρ is the reflectance of a material (dependent on colour, roughness and saturation)

C_1 is the unknown but constant parameters ($\pi P_T \cdot \eta_{Atm} \cdot \eta_{Sym}$)

C_2 is the changeable parameters ($\frac{\cos \alpha}{4r^2}$).

A good understanding of each scanning device, the environment and the reflectance characteristics of different surface materials is essential to minimise the error sources (Voegtle & Wakaluk, 2009). The main source of error in deformation monitoring is the uncertainty of the point cloud position which depends on the instrument noise, target geometry and target surface properties (distance, incidence angle, roughness, and reflectivity) (Bolkas & Martinez, 2017). Understanding the influence of these factors will improve the planning of data acquisition and the selection of appropriate scanner for the job.

Performance metrics can be grouped and discussed under four main subheadings as follows (Kidd, 2016):

- Range estimation
- Laser beam characteristics
- Target detection
- Scanning mechanisms

All equations presented relate to pulse lasers whose output is characterised by energy pulses occurring at a particular pulse repetition rate (PRR).

Range estimation

The simplest form of range calculation uses time of flight (TOF). This is the measured time taken for an emitted laser pulse to travel from the transmitter, be reflected off a surface, and return to the receiver (Wehr, 2008). It is measured using Equation 2.3 (Kidd, 2016).

$$R = \frac{1}{2} c \cdot \Delta t \qquad (2.3)$$

where: R is the distance between the scanner and the object surface

        Δt is the two-way travel time of a light pulse

        c is the speed of light.

Laser beam characteristics

Laser beam characteristics involve a number of the parameters, all of which depend on the laser type and application environment (Kidd, 2016). TLSs typically have wavelengths in the near-infrared band (NIR) between 750 nm and 1550 nm (Kidd, 2016). However, some available scanners fall within the visible light spectrum, operating in the 520 nm to 565 nm or the 625 nm to 740 nm wavelength ranges. The colour of the laser beams operating in these bands are green and red respectively. Green light lasers are more commonly used in bathymetric LiDAR scanners due to their water-penetrating capabilities (Azman et al., 2015). Scanners of various wavelengths have been used in research with published results.

For all TLSs to be commercialised, each system must meet Occupational Safety and Health Administration (OSHA) standards. These standards require that laser systems be below the maximum permissible exposure (MPE), calculated using Equation 2.4 (OSHA, 1999).

$$MPE \geq \frac{Q \cdot PRR}{A_L} \tag{2.4}$$

where: Q is the pulse energy (J)

        PRR is the pulse repetition rate (kHz)

        A_L is the laser footprint (cm^2).

According to Equation 2.4, a TLS with a wavelength of 1550 nm can use higher power settings compared to a laser operating in the 900 nm range (Wehr, 2008). The reason is that a higher wavelength corresponds to a lower frequency and therefore a lower PRR, meaning pulse energy can be higher while still meeting the minimum MPE requirement.

Target detection

Detectability is influenced by various atmospheric and system transmission factors (Baltsavias, 1999). The most important factors include roughness, colour and the degree of saturation of the scanned surface (Voegtle et al., 2008; Suchocki & Katzer, 2016).

According to Baltsavias (1999), the minimum detectable object size depends primarily on surface reflectivity and not the laser footprint (A_L). A problem with highly reflective surfaces, where specular reflections are dominant, is that these reflections significantly increase the backscatter energy of a laser beam signal. Since point coordinates and intensity values are calculated from this received signal, errors outside the nominal accuracy of the instrument have been recorded (Tan et al., 2018; Pesci & Teza, 2008). Figure 2.13 shows wrongly measured points of a retro-reflective target scanned at two different ranges.
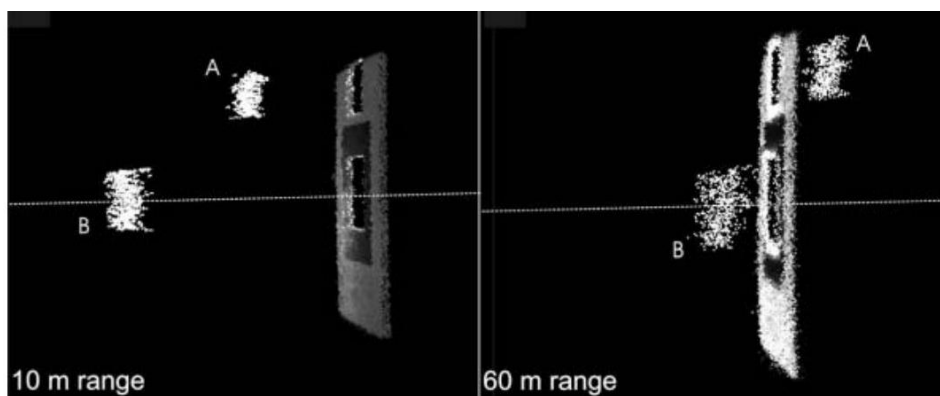
Figure 2.13: Wrongly measured points of two reflective targets (Pesci & Teza, 2008)

Unfortunately, the influence of each individual factor is not typically addressed by manufacturers as they cater for a variety of environments. Gaining a better understanding of the response of individual TLSs to different surfaces is therefore important.

Scanning mechanisms

The scanning pattern, PRR and multi-laser beams of modern laser scanners enable extremely dense point clouds to be captured. Scanners mounted on drones with pre-programmed flight patterns provide repeatability across different scans. However, different scanners produce different scanning patterns (Robeson et al., 2014). The PRR, number of laser channels and the scanning rate (f_{sc}) all influence the density of the point cloud and must be considered depending on the intended purpose.

2.5.3 Applications for intensity readings

Point intensity information, collected with (x, y, z) coordinates, has been an important research topic in recent years with increasing applications (Kaasalainen et al., 2011). Intensity is the measure of the ratio of the amount of emitted radiation over the amount received back from a material surface when struck by a laser beam (Tatoglu & Pochiraju, 2012). Thus, it is a measure of the surface reflectance, strongly associated with surface colour, roughness, material type and degree of surface saturation (Tatoglu & Pochiraju, 2012; Bolkas & Martinez, 2017). Because the measure of intensity of a point is sensitive to different material surfaces, it has proven to be beneficial in distinguishing between the different types.

2.6 PROPERTIES OF SURFACE MATERIALS

All materials have different properties and influence measurements of TLSs differently. Data quality is an important aspect of point clouds. Understanding the response of different material surfaces can help to plan data acquisition better; to account for laser-specific scanning effects; and to apply corrections or annotations to point clouds based on the material type.

Understanding the properties of material surfaces, such as colour, reflectivity and roughness, and how this is affected when the surface is either dry or wet, helps to better predict and explain the backscatter energy of the laser pulse.

2.6.1 Grey-scaled materials

Targets of diffuse and calibrated reflectivity are an excellent means to characterise LiDAR-sensing system performance. Targets of known reflectance that cover a range of reflectance values help to determine the scanner response to surfaces of similar reflectivity. This enables the user to quantify the range accuracy and measured intensity of each target of known reflectance.

Labsphere is an American-based company that specialises in the manufacturing of diffuse reflectance targets. The Zenith Lite diffuse targets exhibit highly Lambertian behaviour and provide near ideal diffuse reflectance over the wavelength range 250 nm to 2450 nm. The targets are available, covering a range of reflectivity values from 5 % to 98 %. Figure 2.14 shows an example of the Zenith Lite targets. It must be noted that the current cost lies in the region of $750 per target.

Figure 2.14: Zenith Lite diffuse reflectance targets (Labsphere, 2021)

When using similar targets of varying reflectivity, Voegtle and Wakaluk (2009) observed that the standard deviation of range measurements increased by a factor of about 2 – from 5 m to 25 m for any one given reflectance. These standard deviations also increased with decreasing reflectivity by a factor of about 4. This means that the diffuse targets scanned at the shortest range and with the highest reflectance produced the lowest standard deviation of range measurement. This result must not be confused with specular reflective targets which produce very different results (Pesci & Teza, 2008; Tan et al., 2018).

2.6.2 Roughness

Roughness is a key factor in the scattering characteristics of an incident beam and varies according to the surface finish and material type. Smooth surfaces usually exhibit mirror-like characteristics which can be explained by a phenomenon known as specular scattering or specular reflection (Suchocki & Katzer, 2018). This is different to diffuse reflection where energy scatter is explained as the cosine of the angle of reflection (Lambert's law) (Suchocki & Katzer, 2018). The difference in scattering behaviour of the incoming laser beams is shown in Figure 2.15.
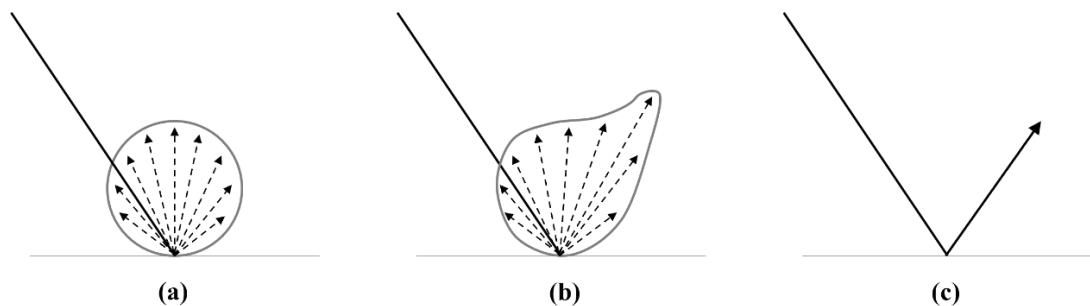
Figure 2.15: Different reflection types – (a) Lambertian diffuse, (b) mixture of diffuse and specular, and (c) specular reflection (adapted from Suchocki & Katzer, 2018)

Most surfaces usually exhibit a mixture of the two types of reflection, as seen in Figure 2.15(b). The proportions of both types relate to the surface roughness (Δh), wavelength (λ) and incidence angle (α) (Suchocki & Katzer, 2018). Lambertian scattering, which is defined by an ideal porous surface, is common for most building materials (Suchocki & Katzer, 2018). This ideal surface can be defined by the Fraunhofer criterion (Equation 2.5) and the Rayleigh criterion (Equation 2.6), with the latter as the more common approach.

A surface is regarded as smooth enough for specular reflection with a reflected wavefront phase shift (Δh) of lower than π/8 and π/2 for the two criteria respectively (Rees, 2013).

$$\Delta h < \frac{\lambda}{32 \, cos(\alpha)}$$ (2.5)

and

$$\Delta h < \frac{\lambda}{8 \, cos(\alpha)}$$ (2.6)

where: Δh is the scale of the surface roughness

      λ is the laser wavelength

      α is the incidence angle.

A beam at normal incidence to a surface with a wavelength of 500 nm will therefore exhibit specular reflection if Δh is less than 62.5 nm. The dependence of the criteria on α shows that the smoothness criterion is more easily satisfied with larger incidence angles. If the same beam as above were to be angled at $\alpha = 60°$, the calculated Δh value would increase to 125 nm. This means that a moderately rough surface may appear effectively smooth when viewed from different incidence angles. A graphical representation of a rough surface is seen in Figure 2.16.
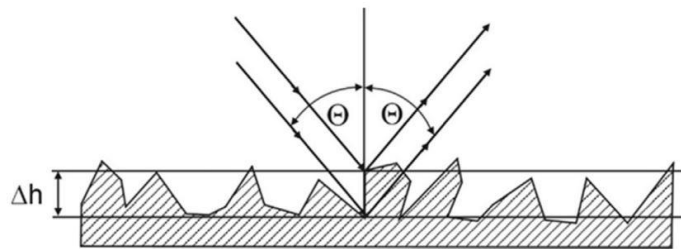
Figure 2.16: Reflection of a laser beam on a rough surface (Suchocki & Katzer, 2018)

Surfaces that meet the above criteria are likely only for certain manufactured materials such as glass, sheet metal and glossy enamel. Surfaces of common building materials, scanned using instruments in the 500 nm to 1500 nm wavelength, typically meet the criteria of an ideal porous or rough surface (Rees, 2013; Suchocki & Katzer, 2018). Intensity readings are strongly affected by any changes in roughness because roughness affects the scattering of emitted energy from which intensity values are determined (Suchocki & Katzer, 2018).

2.6.3   Colour

The colour of a scanned surface is another aspect, just like roughness, that significantly affects the absorption and dispersion of the emitted laser signal (Voegtle et al., 2008). Different coloured targets have been used to assess the effects that range, incidence angle, plane fitting and segmentation have on the point clouds, collected with different scanners (Voegtle et al., 2008; Voegtle & Wakaluk, 2009; Bolkas & Martinez, 2017; Bolkas, 2019). Figure 2.17 shows an example of painted boards used in a study conducted by Bolkas and Martinez (2017).

Figure 2.17: Example of coloured targets painted with matte (left) and semi-gloss (right) sheen (Bolkas & Martinez, 2017)

The matte sheen provided diffuse-like reflection and the semi-gloss sheen a mixture of diffuse and specular reflection (Bolkas & Martinez, 2017). The targets were scanned using two scanners: the TOPCON GLS-1500 and the Lecia ScanStation P40. The scanners had pulse lasers of wavelengths 1535 nm and 1550 nm respectively. In general, darker surfaces resulted in noisier distance measurements, a phenomenon also observed by Voegtle et al. (2008).

Suchocki and Katzer (2018) performed a similar experiment, but used two different TLSs: the Lecia C-10 (λ = 532 nm) and the Riegel VZ-400 IR (λ = 800 nm). The near infrared beam emitted from the Riegel registered similar intensity values for all colours, except the colour black which showed clear lower reflectance values. Work done by Voegtle and Wakaluk (2009) used a phase shift scanner with a wavelength of 670 nm. This laser beam was characterised by red light, similar to the Riegel VZ-400 scanner. The standard deviation of range measurements rose with increasing distance from the target surface, with black exhibiting the highest range standard deviation. This matched their observations from the Zenith diffuse target tests, as well

as the observations of other researchers (Hanke et al., 2006; Kersten et al., 2008). The effect of an increasing incidence angle, however, led to a decrease in recorded intensity (Voegtle & Wakaluk, 2009).

Understanding the effect that colour has on the return signal is important as all scan environments are different. The illumination of the environment in which the scan takes place also affects the returned signal. Figure 2.18 shows the results published by Voegtle et al. (2008) who used a pulse laser scanner with a wavelength of 532 nm (visible green). The measured mean square error (MSE) of range measurements decreased for all colours, other than white, when scans were captured at night as compared to the day.
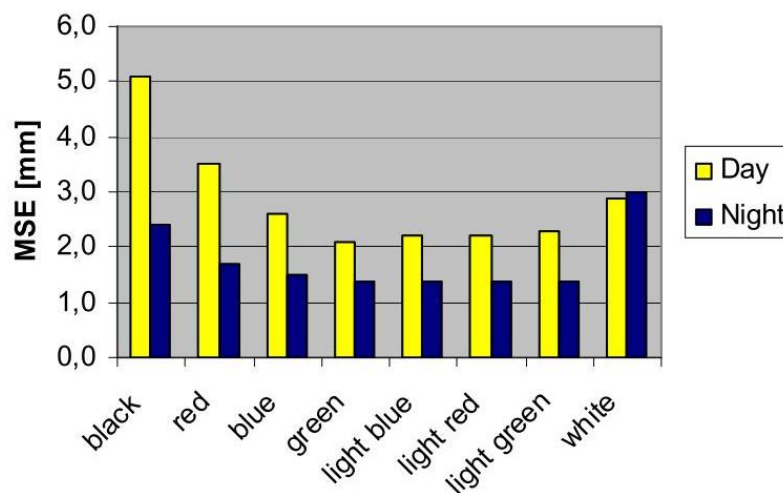
Figure 2.18: Range accuracy for day and night scans (Voegtle et al., 2008)

Two objects, painted with a spectrally pure red colour, look extremely different in visible light when one is placed under strong illumination and the other in darkness. However, if the same pure red were mixed with black, the appearance of the object in the dark is unlikely to appear that different. The reason is that colour is specified by three main parameters – hue, chroma (or saturation) and luminance (Malacara, 2011). While hue and chroma have more to do with the specific colour and its main colour components, luminance relates to surface reflectance. Luminance is defined as the intensity of light emitted off a surface per unit area and scattered in any given direction (Malacara, 2011). This parameter is particularly important because objects and surfaces of different colour and orientation will make up environments where scans are conducted. Understanding the response of a specific TLS to this parameter is important to better understand system performance.

Spectrometry

Spectroscopy is the science of studying the interaction been matter and incident energy and spectrometry is the method used to quantitatively acquire a measurement of the spectrum (CRAIC, 2021). Spectrometers are the devices that measure the intensity of reflected light relative to each wavelength, and that utilise this information to create a spectrum. A multitude of spectrometers are available, but one from SparkFun is reviewed.

The Triad spectroscopy sensor is a relatively low-cost sensor (currently USD $65). It combines three AS7265x spectral sensors that cover the measurement of light wavelengths from ultraviolet (UV) 410 nm to visible to infrared (IR) 940 nm. The 18 individual light frequency bands of the sensor are measured with a precision of 28.6 nW/cm^2 and an accuracy of $\pm$ 12% (SparkFun, 2021). An image of the Triad sensor with dimensions is shown in Figure 2.19.
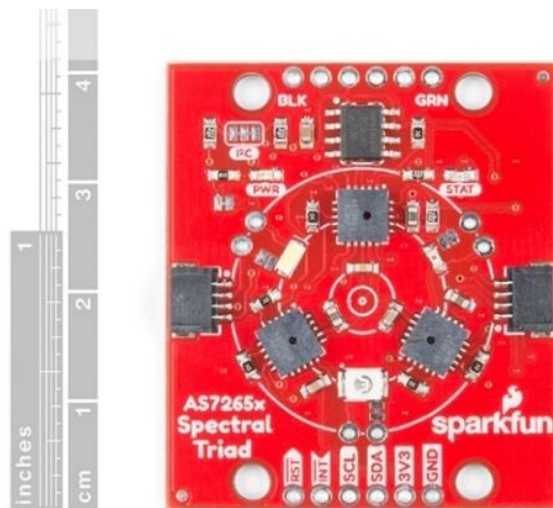
Figure 2.19: Triad spectroscopy sensor (SparkFun, 2021)

The three spectral sensors and associated wavelength bands of the Triad sensor are shown in Figure 2.20. This sensor gives the user the ability to measure and characterise how different surfaces absorb and reflect the light of different wavelengths.
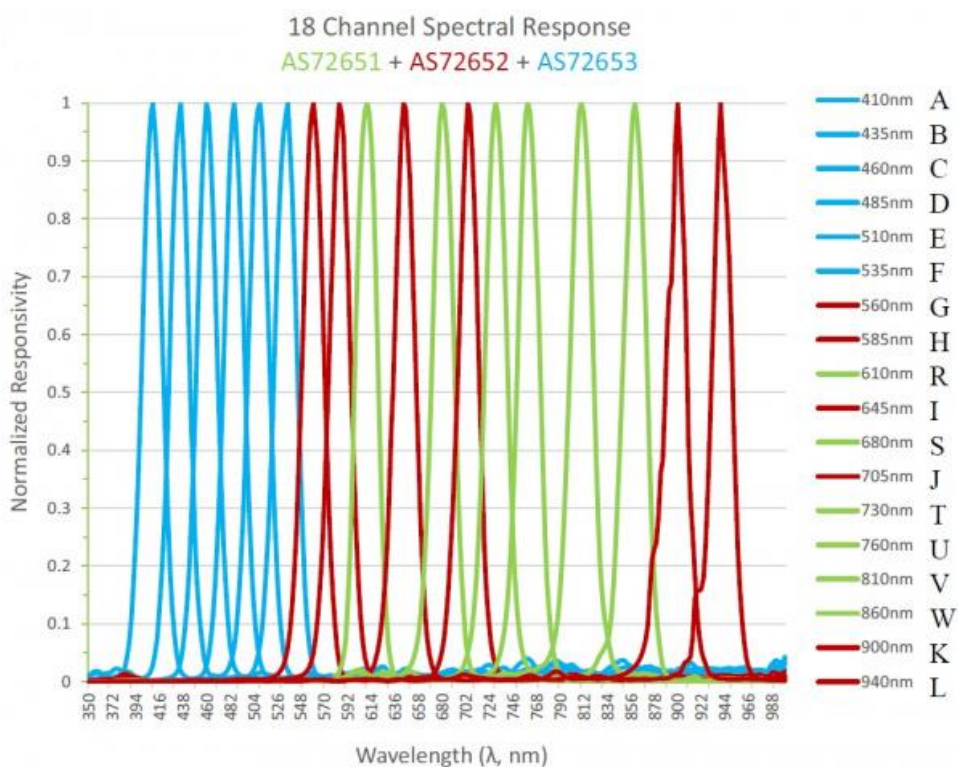
Figure 2.20: Output from spectroscopy analysis (SparkFun, 2021)

2.6.4 Building materials

From the multiplicity of possible materials available, a material common along railway corridors, specifically tunnels, is selected for review. Materials used in previous research have included concrete, brick, wood, marble and metal (Voegtle & Wakaluk, 2009; Suchocki & Katzer, 2016; Filgueira et al., 2017; Suchocki & Katzer, 2018).

Voegtle and Wakaluk (2009) carried out an analysis on materials common to building façades and recorded a rise in standard deviation of range measurements for concrete with increasing distance. An interesting observation was that the standard deviation of range measurements was fairly small (0.5 - 1.2 mm) compared to those obtained from the Spectralon targets (0.5 - 5.3 mm), despite the certain roughness associated with concrete. The influence of incidence angle on these measurements was similar to that observed in the Spectralon and coloured target tests, decreasing with increasing incidence. Scans conducted on different metals introduced extreme problems because data was not recorded for orthogonal scans. The saturation effect was ruled to be the main problem, caused by the high energy backscattered off the shiny (spectral) surfaces. Similar results were observed by Pesci and Teza (2008) and Tan et al. (2018). This observation makes it challenging for rail head geometries to be captured accurately using a TLS (Leslar et al., 2010; Arastounia, 2012).

2.6.5 Degree of saturation

The structural safety of both old and new structures, apart from the pure strength characteristics, rests heavily on the degree of saturation. Water ingress in tunnels is of great concern as this significantly affects the performance of the building materials, both in strength and thermal aspects (Yoo, 2017). Ångström (1925) indicated that a rough wet surface leads to diffuse reflection and subsequent internal reflection caused by the air-water interface. This concept is illustrated in Figure 2.21 with the layer height of water exaggerated to show a saturated surface. Water is known to have a high absorption coefficient (Tan et al., 2016; Suchocki et al., 2018). This means that, in theory, a scanned surface in different states of saturation should influence the properties of the return laser signal and result in a change in intensity readings.
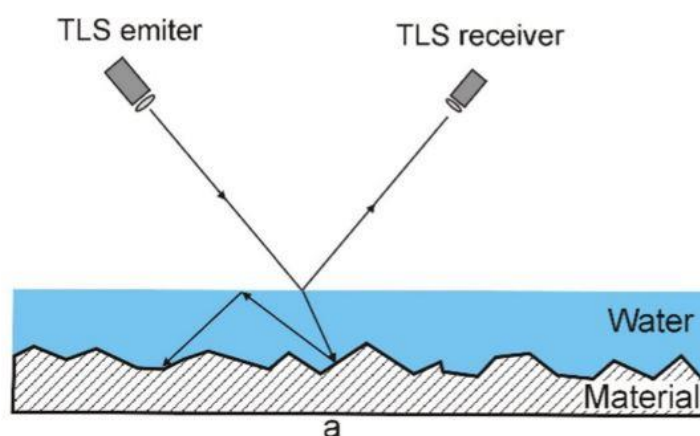
Figure 2.21: Behaviour of a laser striking a saturated rough surface (Suchocki & Katzer, 2018)

The ability to detect water leakage areas during infrastructure inspections would be extremely useful for structural safety checks and long-term deterioration monitoring. This measure would be implemented in addition to the ordinary physical distance measurements that already make use of the (x, y, z) coordinate information of the point clouds. Attempts at using intensity as a means of characterising surface properties have been tested before. Work done by Suchocki and Katzer (2016) aimed to prove the aptitude of using TLSs for remote sensing of the saturation of building materials. On average, the difference in intensity values of concrete in its fully saturated state were 18 % lower than when saturated by air humidity, proving that areas of saturation can be identified using intensity information.

Suchocki and Katzer (2018) briefly acknowledged the implications of trying to detect saturation based on intensity information. The study concluded that scanners with wavelengths in the NIR band seemed better suited to detect areas of saturation while the sensitivity of the green beam made them more useful for detection of different coloured objects (Suchocki & Katzer, 2018).

After results were published by Suchocki and Katzer (2018), Suchocki et al. (2020) conducted field experiments to validate these observations. The main aim of the research was to compare time-of-flight (TOF) and phase-shift (PS) scanners, based on collected intensity data for moisture and bio-deterioration detection. A concrete wall covered in plaster was scanned dry and then intentionally flooded with tap water to depict saturated conditions. Figure 2.22 shows how an increase in saturation brings about an increase in absorption of energy and consequently lower intensity values (Suchocki et al., 2020).
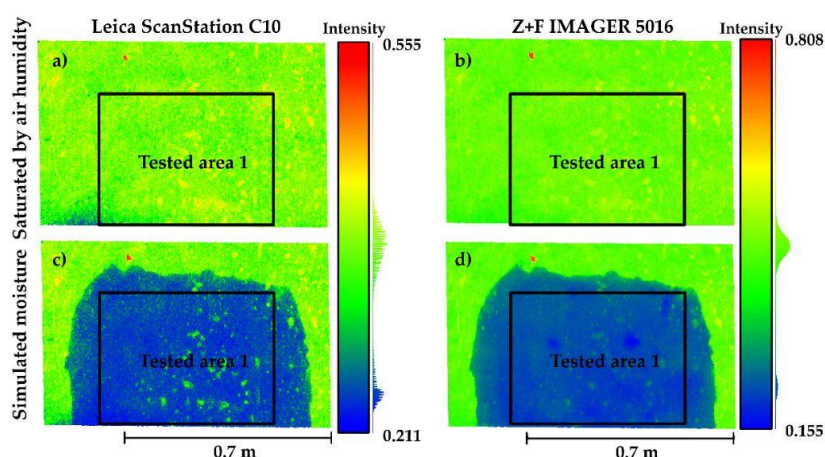
Figure 2.22: Value of intensity recorded by two TLSs (Suchocki et al., 2020)

2.6.6   Previous studies on the Velodyne VLP-16

Numerous studies have been conducted on various aspects of the Velodyne VLP-16 LiDAR, including calibration and stability (Glennie et al., 2016), measurement uncertainty (Péntek et al., 2018), dense point cloud acquisition (Bula et al., 2020), surface feature surveying (Kidd, 2017) and quantifying the influence of rain (Filgueira et al., 2017).

The study by Glennie et al. (2016) aimed to evaluate the long-term stability, geometric calibration and temperature variation effects of the VLP-16 LiDAR. The overall accuracy matched the 3 cm root mean square error (RMSE) specification published by manufacturers and the tested residuals were calculated to lie between 22 and 27 mm. In the same year a full

performance evaluation of the VLP-16 laser scanner was undertaken by Kidd (2016). The research consisted of laboratory experiments and field mapping of marine surface features. In addition, Filgueira et al. (2017) attempted to quantify the influence of rain on the different LiDAR parameters, such as range, intensity and data density.

Péntek et al. (2018) evaluated a method to validate a LiDAR uncertainty prediction model and develop a point-to-pixel association that matches each 3D point to a colour. Development of a low-cost rotating TLS was later proposed by Bula et al. (2020) to acquire denser point clouds. The rotating VLP-16 LiDAR puck allows continuous change in direction, enabling the densification of scans. Work done by both Péntek et al. (2018) and Bula et al. (2020) on the VLP-16 LiDAR has since been incorporated into the Emesent Hovermap system.

2.7   EMESENT HOVERMAP SYSTEM

The Emesent Hovermap is a mobile TLS system in which data capture can take the form of handheld, vehicle-, or drone-mounted scans. The system is lightweight, with the frame constructed from aluminium combined with carbon fibre composite panelling. This sturdy design enables the Hovermap to withstand harsh scanning environments while supporting the rotating VLP-16 LiDAR (Emesent, 2020). A quick release mechanism allows easy switching between acquisition modes (drone to handheld scans) for hard-to-reach places where additional point cloud information may be required.

An onboard computer encased within the Hovermap allows simultaneous localisation and mapping (SLAM) algorithms to generate the point cloud of the scanned environment through real-time processing of inertial measurement unit (IMU) and LiDAR data. The SLAM algorithm has the ability to interface with controllers of compatible drones, providing collision avoidance, position hold, programmable flight plans and the ability to navigate dark and GPS-denied environments (Jones et al., 2020). The capabilities of this system make it attractive for underground mining operations and tunnels where no GPS signal is available. The varying levels of drone autonomy offer endless data capture possibilities. Figure 2.23 shows some of the Hovermap functionalities and traits, as discussed above.
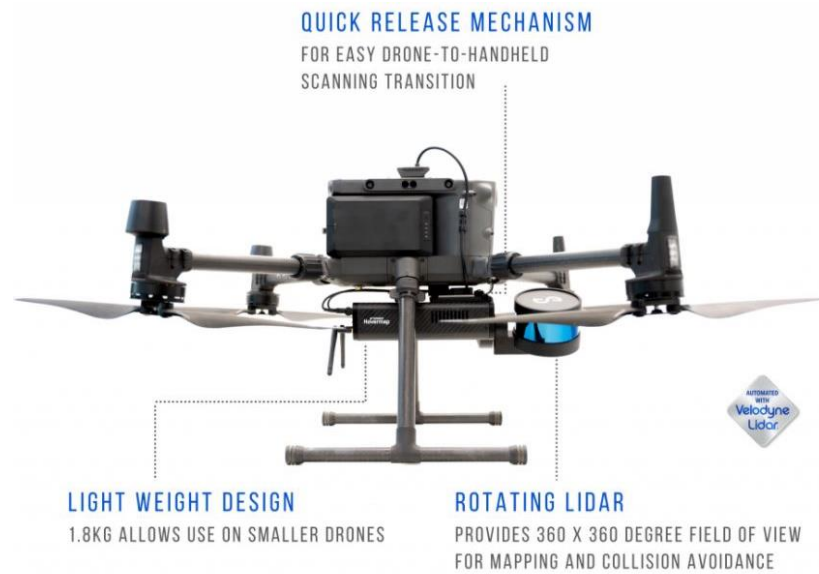
Figure 2.23: Emesent Hovermap system functionalities (Emesent, 2020)

2.7.1 Integration and specifications of the VLP-16

The light weight and compact design of the Velodyne VLP-16 LiDAR makes it an ideal attachment for the Hovermap system. Weighing only 830 g, it brings the total weight of the Hovermap system to 1.8 kg.

Specifications

The VLP-16, manufactured by Velodyne, Morgan Hill CA, is a third-generation multi-laser scanner. The VLP-16 LiDAR comprises 16 individual lasers fixed on a rotating head and arranged in a 30° field of view (FOV) (–15° to +15°), with a 2.0° vertical resolution. It yields a complete FOV that is symmetrical in terms of the horizontal plane, as illustrated in Figure 2.24. Additional features and specifications of the VLP-16 are tabulated in Table 2.1.
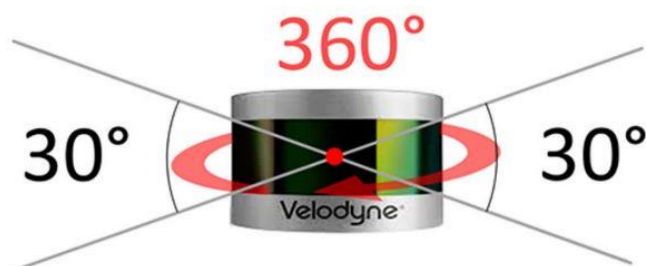
Figure 2.24: Field of view of the VLP-16 (Bula et al., 2020)

Table 2.1: Velodyne VLP-16 specifications (Bula et al., 2020)

Channel	16
Wavelength	903 nm
Ranging accuracy	±3 cm (typical)
Measurement range	Up to 100 m
Single return data points	$300\,000$ points s^{-1}
Maximum number of returns	2
Field of view (vertical)	30°
Vertical angular resolution	2.0°
Field of view (horizontal)	360°
Horizontal angular resolution	0.1–0.4°
Laser rotation	10 Hz
Weight	830 g
Dimension	$\varnothing$ 103 mm, h 72 mm
Retail price	USD 4000

The predecessors of this third-generation scanner were the HDL-32E and HDL-64E, both of which have been extensively researched in literature (Glennie, 2016). The substantially lower cost (approximately USD \$4000) of the VLP-16 compared to its predecessors stems from the reduction in vertical resolution (Neumann et al., 2016; Morales et al., 2018).

Integration

The VLP-16 is the smallest of the multi-beam lidar (MBL) units available from Velodyne in terms of both its size and number of laser channels. The lightweight and compact design of this MBL has created potential for the device to become a common solution to the need for rapid data acquisition. The disadvantage of the VLP-16 is its limited vertical resolution and field of view, as illustrated in Figure 2.24. However, this can be offset by adding an extra degree of freedom (DOF), as previously attempted by Péntek et al. (2018), Morales et al. (2018) and Bula et al. (2020). Hovermap is the first commercially available mobile mapping unit that has successfully incorporated this additional DOF, which transforms the original MBL into a rotating multi-beam lidar (RMBL), thus yielding a completely spherical FOV.

The Hovermap system is available in two different configurations, depending on the required customer application. The hardware and software are identical and the only difference is the position and orientation of the VLP-16 puck. Figures 2.25 and 2.26 show a schematic of the Hovermap system with the revolving VLP-16 puck attachment in the two available configurations.

Figure 2.25: Side and back view of the Hovermap VF1 setup (Emesent, 2020)

Figure 2.26: Side and back view of the Hovermap HF1 setup (Emesent, 2020)

When fitted to a drone, the forward-facing, horizontal orientation (HF1 setup) enables greater coverage directly above the drone. This is particularly useful in eliminating the shadowing effects and low point density directly above the system which are inherent in the vertical orientation (VF1 setup) (Jones et al., 2020).

The rotating mechanism that converts planar FOV to a spherical one is important to prevent irregular and uneven point clouds. Hovermap's incorporation of the RMBL changes the initially intended output of a 360° horizontal FOV to a spherical one (360° x 360°), providing an almost even point cloud (Jones et al., 2020). This 3D point cloud improves object detection and provides the basis for the creation of SLAM algorithms. However, the multiple beams of the VLP-16 cause a certain amount of overlap through the introduction of the additional degree of freedom. These overlapping beams result in extremely complex scanning patterns in which some areas remain in a blind spot.

2.7.2 Velodyne scan pattern distribution

Previous authors have conducted point pattern analyses of various LiDAR scanners. These entailed modelling the spatial patterns and distribution, as well as observing the influence an additional DOF had on the produced point cloud (Ripley, 1977; Wulf & Wagner, 2003; Robeson et al., 2014; Morales et al., 2018; Bula et al., 2020; Lassiter et al., 2020).

Morales et al. (2018), Bula et al. (2020) and Lassiter et al. (2020) are the most recent publications, all with a strong focus on the Velodyne VLP-16 LiDAR scanner. Two of the papers allude to the growing interest among researchers and industry partners in a portable and affordable 3D lidar system capable of accurate and timeous 3D point cloud reconstruction. Such a device is said to have extended applications in progress tracking in construction sites, intelligent surveillance, crime scene reconstruction and the monitoring of environmental risks such as rockfalls, landslides and mine and tunnel collapses (Leingartner et al., 2016; Morales et al., 2018; Bula et al., 2020).

Figure 2.27 shows the local frame X_v Y_v Z_v of the VLP-16 puck, with the Y_v and Z_v axes representing the forward and upward directions respectively. Rotating the puck on the Z axis is redundant since it represents the internal spinning motion of the puck itself. Thus, it should be rotated on one of the remaining two axes.
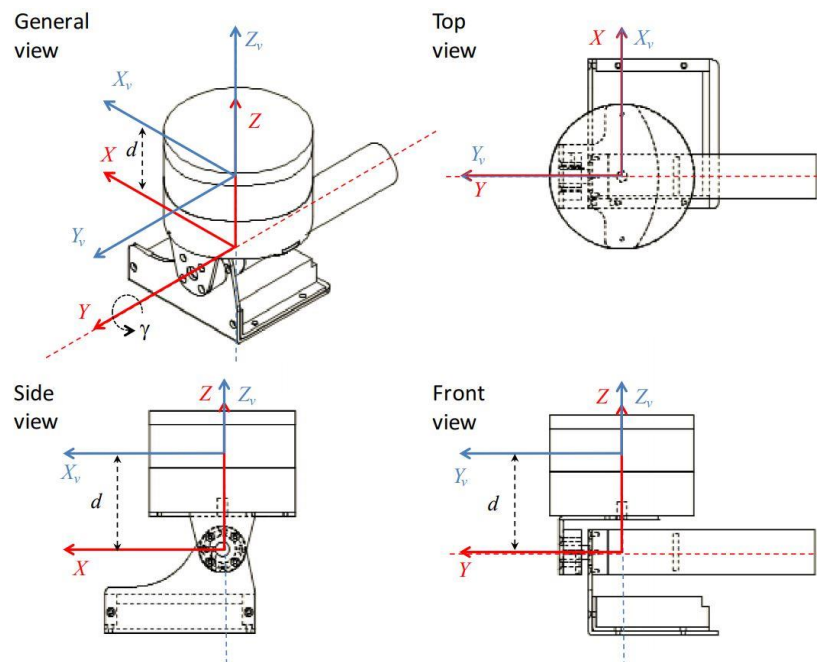
Figure 2.27: Local reference frame of the VLP-16 puck (blue) and rotational axis (red)

(Morales et al., 2018)

Rotation of the puck on the *X* or *Y* axes would be similar since the complete FOV of the VLP-16 is symmetrical with respect to the horizontal plane (Bula et al., 2020). Figure 2.28 shows the results of a numerical simulation performed by Morales et al. (2018). The distribution of points within the virtual hollow sphere assists in visualising the different scan patterns. Figure 2.28(a) illustrates the symmetrical beam pattern of the VLP-16 MBL with the full 360° horizontal FOV. Figures 2.28(b) and 2.28(c) show the points for the RMBL with different tilt speeds. The patterns formed by distributing the points over the sphere are clearly visible, especially in the lower resolution (120°/s) scan.
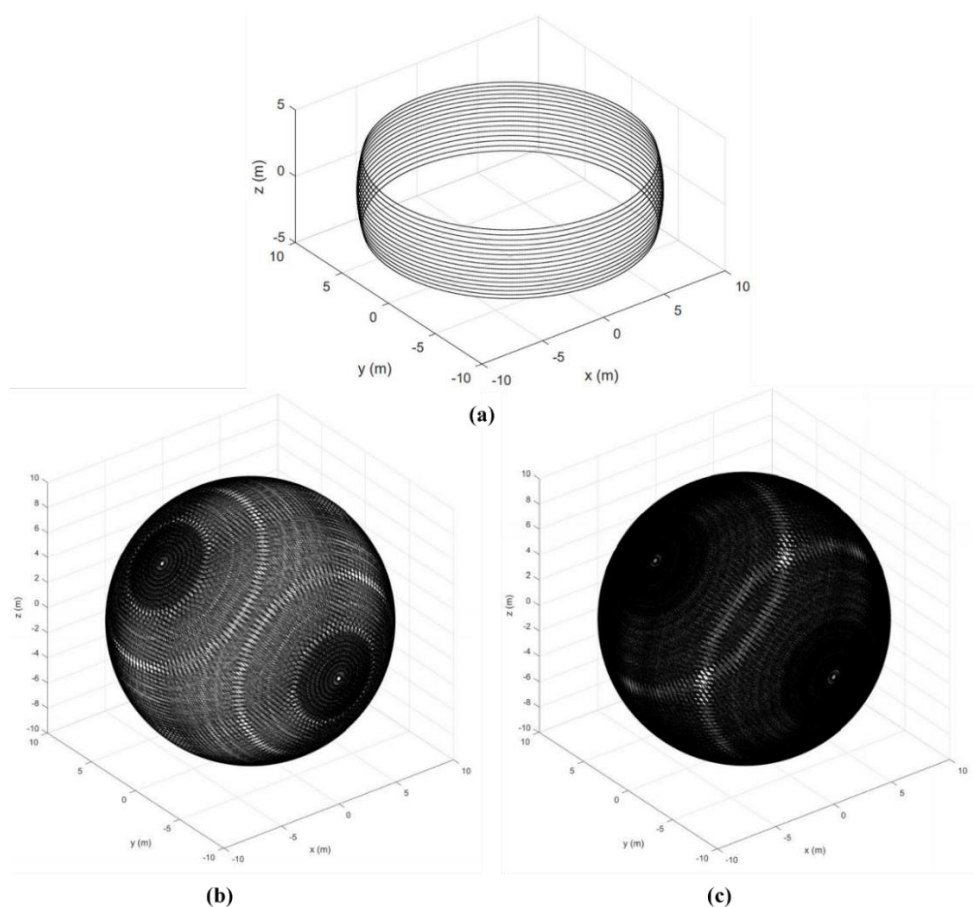
Figure 2.28: Visualisation of point distribution – (a) VLP-16, (b) RMBL at 120°/s tilting speed, and (c) RMBL at 50°/s tilting speed (adapted from Morales et al., 2018)

Morales et al. (2018) observed that both RMBL tilting speeds offered denser point clouds with a wider FOV compared to the static MBL. The orientation of the scanner also influenced the observed point patterns. The translation of scanned points onto planar surfaces is shown in Figure 2.29. The planar surface parallel to the Y axis produced a point cloud with a higher

density on the sides compared to the wall parallel to the X axis, which showed a much higher point density close to the centre, corresponding with the tilt axis. These differences are important to take into account when planning and deciding on scanner orientation with regard to the surface under consideration.
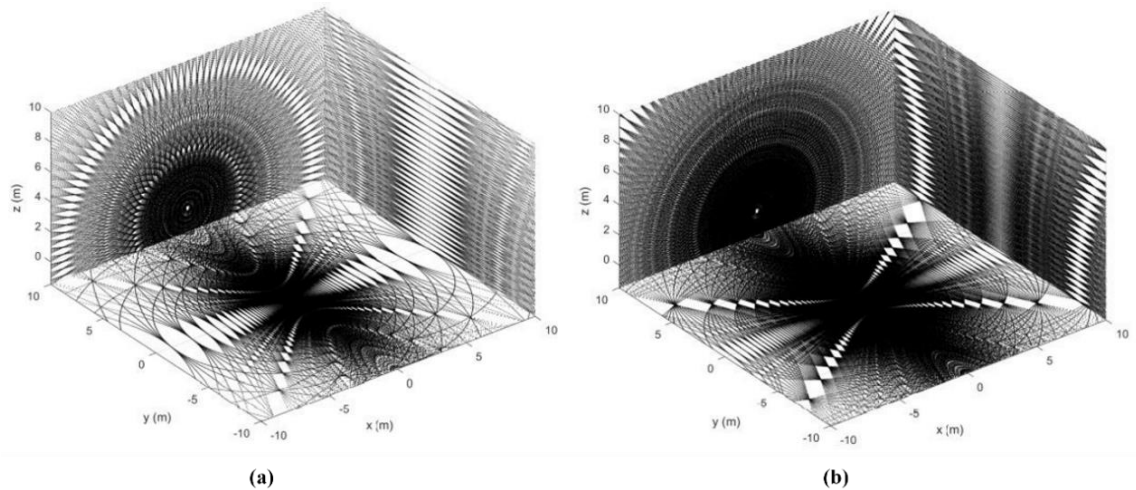
Figure 2.29: Orthogonal plane points of the RMBL with tilting speeds – (a) 120°/s and (b) 50°/s respectively (Morales et al., 2018)

2.7.3 Hovermap capabilities and specifications

The versatility of Hovermap enables the safe, easy and fast scanning and mapping of dangerous or inaccessible areas (Emesent, 2020). The application and capabilities of Hovermap are widespread and include:

- Telecommunication towers and powerlines
- Vertical shafts
- Industrial plants
- Tunnels and bridges
- Building and construction
- Mining
- Stockpiles
- Agriculture.

Table 2.2 summarises the specifications of the Hovermap system and compatible drones. It also gives additional specifications related to the mapping and data management of point clouds.

Table 2.2: Hovermap capabilities and specifications (adapted from Jones et al., 2020)

	Description	Comment
Hovermap Sensor		
LiDAR	Velodyne VLP-16 Lite (Puck)	Class I laser product
	- Up to 100 m range	Rotating to give a near 360° x 360° field of view
	- 16 channels	Useful for complex environments
	- Up to 300,000 points/sec	Return signal dependent on environment
	- Dual return	
Drone Autonomy		
Type	DJI M210 / M300 / M600	Compatible with drones equipped with DJI A3 autopilot
Flight time	10 - 30 min	Dependent on drone type, environment and payload
IP rating	Variable: none - IP57	Drone dependent
Collision avoidance	Omni-directional	Adjustable minimum distance collision avoidance threshold
Mapping and Results		
Mapping only	Handheld	Carried by hand or mounted to backpack
	Vehicle mounted	Any ground vehicle
	Drone mounted	Any VTOL drone capable of carrying the payload
SLAM	Local solution: real time	Used for collision avoidance and position hold
	Global solution: post-processing	Full point cloud solution for analytics
Point cloud processing time	Local: Real-time during flight	Displayed to pilot
	Global: 2 x flight time	Full point cloud solution for analytics
Georeferencing	Above ground	Georeferenced point clouds via GPS (in WGS84)
	Below ground	Via survey spheres or scan-toscan registeration
Colourisation	GoPro Hero 8	Colourisation of point clouds for easier classification
Accuracy*	± 30 mm	Raw data, ± 15 mm possible for post processed
Precision*	± 10 mm	Repeatability for local point cloud alignment
Data Management and Physical		
LiDAR data format	.las / .laz / .ply / .dxf	Each point cloud contains the following atrributes
		- Location (x, y, z)
		- Intensity
		- Range
		- LiDAR channel number
		- Time since scan started
USB3	300 MB/second	High speed data offload
Storage	480 GB	Approximately 12 hours of sensor data
Power	12 V - 54 V (Max 50 W)	Powered from battery or auxillary input
Size	393 x 155 x150 mm	(length x width x height)
Weight	1.8 kg	Lightweight to serve as a payload on drones

Recent advances have seen the introduction of colourisation of point clouds. A specialised Go-Pro Hero 8 mount for the base of the Hovermap enables video footage to be captured, providing additional red-green-blue (RGB) colour information for each point in the cloud. Colourised point clouds have the potential to assist in the classification and interpretation of point cloud data, further extending the capabilities of the Hovermap system (Emesent, 2020; Jones, 2020). Figure 2.30 shows the Go-Pro mounted at the base of the Hovermap.

Figure 2.30: Hovermap with GoPro attachment fitted to UAV (Emesent, 2020)

It is beneficial for surveying and mapping to combine LiDAR, which delivers 3D point clouds, with imagery that provides 2D to 2.5D rasters of the object and its surface spectral properties (Péntek et al., 2018). The fusion of point cloud and colourisation data by the Hovermap system is reliant only on the calibration of the Go-Pro and LiDAR puck, based on the measured offset between the two. The remainder of the registration of the two data sets is done automatically through the in-house processing software of Emesent.

2.7.4 Data collection and software

Hovermap's simple push-start button and quick-release handle mean capturing data is possible within 60 seconds of being switched on (Emesent, 2020). Capturing point cloud data with the Hovermap system can be summarised into four main steps, as shown in Figure 2.31. In the case of airborne scans, the fly/capture time is usually limited to the drone's battery life. In a handheld scan scenario, the life of an external lithium battery is used to power the Hovermap unit.
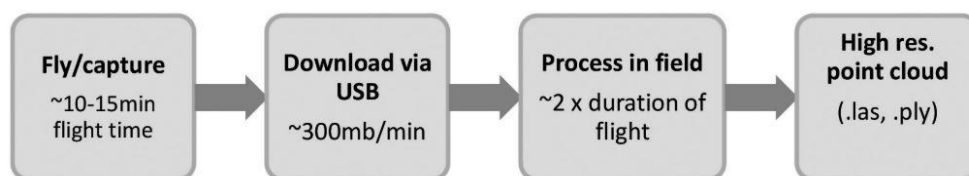
Figure 2.31: Overview of the steps required to extract point cloud data from the Hovermap (Jones et al., 2020)

The duration of the scan may also be governed by various other factors, including:

- Area of data capture
- Required density
- Complexity of features within study area
- Access restrictions.

The limitation of capture time, however, almost always returns to the battery life of the drone or external battery supply. The Hovermap, with its 480 GB of onboard storage, can store a full day of data capture at an acquisition rate of 300,000 pts/s (approximately 7 MB/s) (Emesent, 2020; Jones et al., 2020).

The total time required from start up to the final export of point clouds for further processing is roughly twice the time required for the initial capturing of the scan. For example, point cloud data from a five-minute scan will be ready to view and analyse in third party software within ten minutes. This rapid capture of 3D point cloud data makes this system an extremely time- and cost-effective solution for monitoring and data collection.

2.7.5   Maptek software

Maptek, an Adelaide, Australian-based company, is a leading provider of innovative 3D modelling, spatial analysis and design software tailored specifically for the global mining industry. The ability to automate workflows and write custom Python scripts for the collection, filtering, analysis and presentation of point clouds makes Maptek stand out from its competitors (Maptek, 2021). The PointStudio software package can be utilised as third-party processing software for all point clouds collected using the Hovermap.

2.7.6   Previous studies on the Hovermap

Many previous studies were carried out on the VLP-16 puck but none, apart from two known technical notes and one white paper, focussed on the performance of the Hovermap and VLP-16 puck as an integrated unit. A paper reviewing applications of the Hovermap for underground mining was published without inclusion of any laboratory experimentation (Jones et al., 2020). Two technical notes were written – one on accuracy evaluations and the other on georeferencing experiments of Hovermap point cloud data (Sofonia, 2020a; Sofonia, 2020b). The most recently published white paper demonstrates an improved convergence monitoring method at Rio Tinto's diamond mine using Hovermap LiDAR data (Evans, 2021). To date, no other papers, to the authors knowledge, have been published on the Hovermap and VLP-16 LiDAR system as an integrated unit.

2.8   DIGITAL TWINNING

The concept of creating virtual copies of existing infrastructure has the potential to revolutionise the way assets are managed (Zhu & Hyyppa, 2014). The disadvantage, however, is the cost of effectively generating such 'virtual copies' or BIMs. The element of periodicity that railways pose, benefits the real-to-virtual synchronisation in some ways and has shown success in early attempts at twinning. However, twinning still experiences some shortcomings (Sánchez-Rodríguez et al., 2018; Ariyachandra & Brilakis, 2019). Research by Leslar et al. (2010) involved the collection and inventory of 32 route miles of track, including sidings and rail yards. This was shown to be possible through the use of semi-automatic tracking features and manual digitisation. The processing took over 100 hours and only produced basic outlines of the different surfaces. Similar work was carried out by Geng et al. (2020). The future advantages of having a complete digital twin of a railway will offer a 3D display model of the physical asset that can be enriched with design, construction, operation and maintenance data, acting as a central data storage hub for the asset.

For now, 3D point clouds serve as virtual copies of the asset condition at the time the inspection was conducted, which can be saved as reference for engineers to refer to should the need arise. Extracting as much detail as possible from these models will assist companies to plan better, avoid costly mistakes and bid more tightly and competitively to win contracts. Emesent's introduction of colourised point clouds is a step forward in producing a more complete model of the scanned environment. The addition of RGB colour information will aid designers and CAD specialists to generate BIM models of the given environment, which can then be supplemented with additional operational and maintenance data.

2.9   THE FUTURE OF REMOTE MONITORING

The future of 3D mapping depends on the partnerships between scanning and software companies, which will enhance user experience and enable greater visualisation of scanned environments. The combination of other tools such as photogrammetry and point cloud colourisation will aid in generating data-rich 3D point clouds that will change the way in which assets and infrastructure are managed.

Predictions for the future are that all sites will be scoped, reviewed and discussed virtually before setting foot out of the office (Jones, 2020). LiDAR- and SLAM- based technology will continue to improve autonomy, playing a vital role in removing the need for personnel to access dangerous areas. Emesent has already demonstrated the first intercontinental flight which

shows footage of a drone undertaking an inspection in an underground Canadian mine while being operated from Emesent head office in Brisbane (Emesent, 2020). This pilot project demonstrated the beginning of the concept of remote automated data acquisition with minimal human interaction (Jones, 2020). The current extended period of COVID-19 lockdown and restricted movement has made it impossible for many inspections to be carried out. Technologies such as the Hovermap system have the ability to enable such inspections to continue, conducting them remotely and allowing operations to carry on as normal.

2.10   SUMMARY

Ageing, continuous loading and other environmental factors result in the deterioration of infrastructure over time. Regular inspections are necessary to provide early warning signs and promote continued maintenance for the safe running of train operations. However, traditional visual inspections of infrastructure are time-consuming and rapidly being replaced by faster, more accurate inspection methods. This literature review highlights the need for efficient, accurate and cost-effective monitoring of railway tunnel infrastructure.

A brief description of the typical defects found on concrete structural elements was reviewed, with particular attention to water ingress. The literature highlighted the importance of NDT for tunnel inspections with emphasis on LiDAR technology. The basic theory of LiDAR was reviewed and possible use cases for intensity information were considered. The roughness of a surface and the difference this makes to the scattering behaviour of incident beams were discussed, together with the response of different colours to scanners with different wavelengths. General building materials, characterised by diffuse reflections, were reviewed, together with the degree of saturation effects on concrete surfaces. Previous studies on the Velodyne VLP-16 LiDAR were discussed, followed by a detailed description and breakdown of the Emesent Hovermap system.

Apart from two papers published by Dr Jeremy Sofonia from Emesent, no other publications to the authors knowledge have been written to evaluate different aspects of Emesent's Hovermap system. Understanding the response of different materials and the returned laser signal from the Hovermap system will aid in planning and coordinating inspections to yield the best possible results. Many published articles in the literature on this topic assess different TLSs and conduct laboratory and field tests to quantify the performance of each. Advances in scanner size and weight are leading to the replacement of static TLSs in some areas by mobile LiDAR units that can be fitted to drones to reach previously inaccessible areas. This will further develop and improve autonomous data capture.

3   METHODOLOGY AND EXPERIMENTAL SETUP

This chapter discusses the methodology and experimental setup followed to capture and analyse 3D point clouds generated from using Emesent's Hovermap LiDAR system.

Controlled laboratory experiments were conducted to observe the change in range accuracy and intensity of point clouds. To measure this change, different colour and concrete targets were scanned at various ranges and incidence angles to investigate the effect of colour, roughness and degree of saturation on the associated point clouds. To verify results from the laboratory testing, field tests were done on operational concrete railway tunnels. These tests were the main focus of the work and were conducted to assess the suitability of the Hovermap system for field surveying and water leakage mapping of concrete tunnels as a cost-effective method to replace on-site visual inspections.

3.1   TEST TARGETS AND MATERIALS

This section covers the materials selected and used to manufacture targets that were scanned using the Hovermap LiDAR system. Only colour and concrete targets were investigated.

3.1.1   Selection of coloured targets

The first part of the study required 24 300 x 300 mm target boards, manufactured from 3 mm MDF, to be cut to size. Of the 24 boards, half were left in their raw state and the other half were made to resemble a rough surface.

The rough surface was achieved by gluing a 300 x 300 mm piece of 40 GRT sandpaper to the surface of each board. Sandpaper was used to maintain uniform roughness over the full target surface area. The remaining 12 targets were left in their original raw state to resemble smooth surface finishes. Homogeneity across all smooth surfaces was assumed as MDF is an engineered material, unlike wood which has inherent grains and markings that are not constant across different pieces. Figure 3.1 shows an example of the two different target surfaces. Once all the boards were complete, they were painted.

Figure 3.1: Raw smooth and rough targets

The study used ten different colours in total. The paint utilised was Spraymate spray paint with the following advertised names: sunshine yellow, brilliant green, signal red, tangerine, electric blue, light grey, machine grey, dark brown, white gloss and gloss black. All the listed colours were applied with a semi-gloss sheen finish. Two additional colours – white and black – with a matt sheen finish were also tested. Each of the twelve different colour sheens were applied separately to both a rough and smooth target surface. This was done to assess the diffuse and specular reflectance properties on each surface. Figure 3.2 shows the full set of 24 target boards with their associated colours and finishes. The two matte colours are in the bottom right-hand corner of both images.
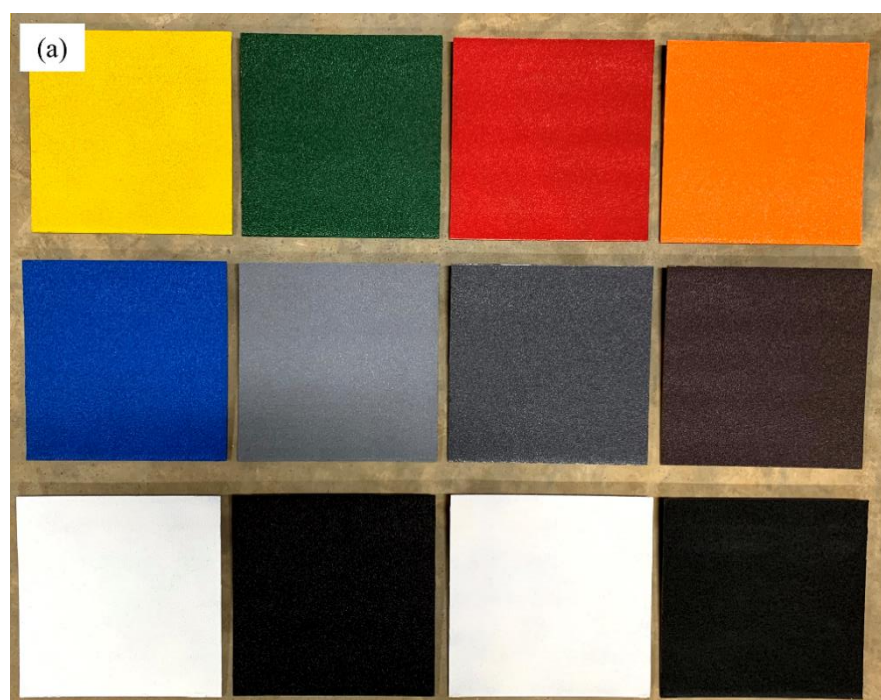
Figure 3.2: Coloured targets (a) Rough and (b) Smooth

The light reflection from some of the semi-gloss targets can be seen in Figure 3.2(b). A custom-made shelving rack, shown in Figure 3.3, was used to store all the coloured targets. This was done to allow adequate time for the paint to dry and to prevent any damage to the surfaces, thus providing the highest level of repeatability across different scans.

Figure 3.3: Rack to store coloured targets

To measure the response of light of different wavelengths, a spectroscopy analysis was carried out. The Triad spectrometer provided a cost-effective means of obtaining reflectance measurements of the different colours with a smooth and rough surface finish. Each target was scanned using the Triad spectrometer to measure the reflection and absorption of light at specific wavelengths in the range from 410 nm (UV) to 940 nm (IR). The sensor was attached to a small 3D printed black box, as shown in Figure 3.4. This was done to eliminate the effect of any external light. The spectrometer measurements were conducted in a dark room to further eliminate any additional external lighting effects.
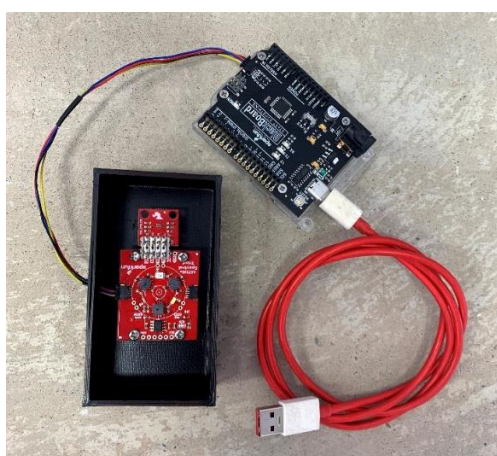
Figure 3.4: Triad spectrometer connected to an Arduino microcontroller

The box was placed face down on each coloured target and readings were taken for a ten-second period, as shown in Figure 3.5.
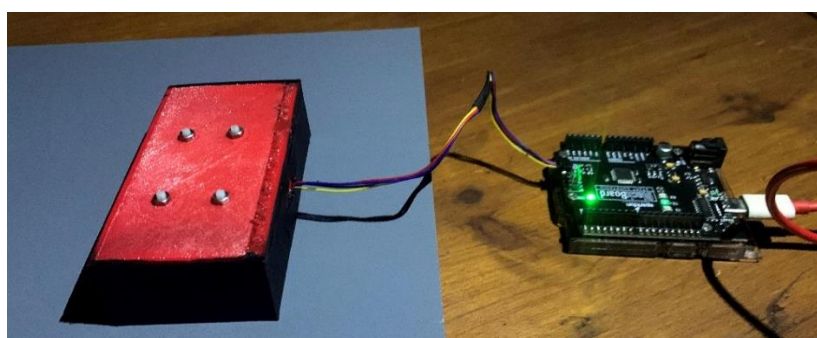
Figure 3.5: Spectrometer measurement on coloured target

The raw results of the different coloured surfaces are summarised in Figure 3.6. Each of the 18 x-axis labels correspond to the different wavelengths measured. This analysis was done to later run a regression analysis to observe any correlations between the target's spectral reflectance and measured intensity values from the point cloud data. The reflectance values at the 905 nm wavelength were of particular interest because this wavelength matched that of the Hovermap.
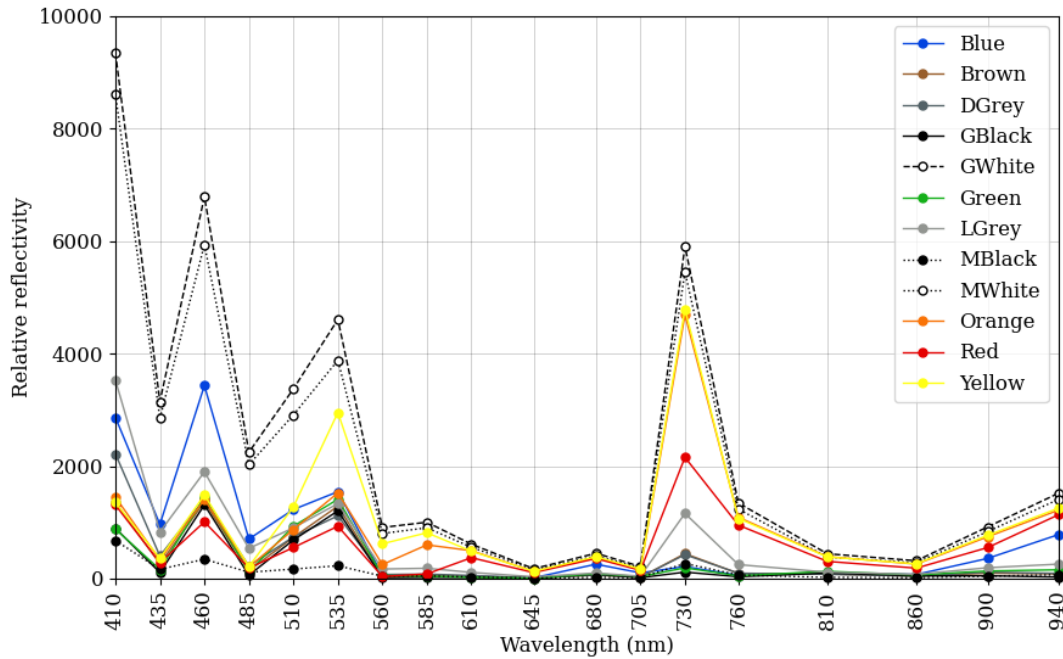
Figure 3.6: Raw reflectance results of the smooth coloured targets for different wavelengths

3.1.2   Selection of concrete targets

Concrete targets were made to measure and observe the effect of roughness and degree of saturation on the intensity information of the captured points. The targets were cast in steel moulds with the dimensions 300 x 300 x 50 mm, using two different mix designs. The mix designs utilised a standard 0.5 water-to-cement ratio and the only difference between the two mixes was the aggregate type. Mix 1 contained crushed dolomite aggregate and Mix 2 decomposed granite sand. The reason for the selection of different aggregates was to observe if this made any significant difference to the recorded intensity values since it is known that colour affects intensity readings. Four bolts were cast in-situ into the back of each panel to allow for easy attachment to a specialised rotating bracket. Figure 3.7 shows the steel mould with the connection bolts cast in-situ. A total of six panels were cast, three for each mix design.
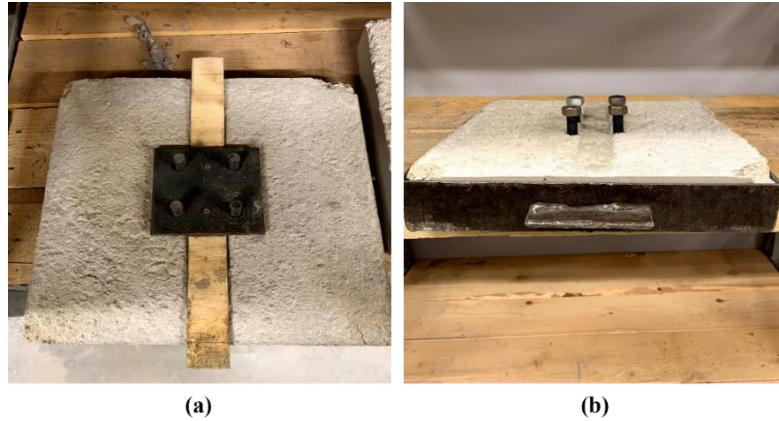
Figure 3.7: Concrete targets with bolts cast in-situ – (a) Top view (b) Front view

For each set of three panels, one was left in the original demoulded condition and the remaining two were given a rough concrete finish with two different degrees of roughness. Figure 3.8 shows the six concrete targets with varying roughness for the two different mix designs. Each target was labelled as smooth, rough and very rough in increasing order from left to right. The roughening of the concrete surface was done using a hammer and chisel. The volume of material removed from each target was recorded and the percentage matched between targets of the same roughness for the two different mix designs. This was carried out to minimise variation as far as possible and to allow for more accurate comparisons.

Figure 3.8: Targets of varying roughness – (a) Mix 1: Dolomite (b) Mix 2: Granite

3.2   LABORATORY TESTING

This section describes the experimental work performed which includes laboratory setup, setup of scanning equipment, preparation and mounting of targets and testing methodology.

3.2.1   Scan pattern

The scan pattern of the Hovermap was analysed against two adjacent concrete wall faces, as shown in Figure 3.9. This was done to identify blind spots when operating from a static position.

Figure 3.9: Adjacent concrete wall faces

3.2.2   Experimental setup

The basic experimental setup remained the same for all targets scanned. The short duration of each scan allowed system and atmospheric transmission factors and transmitted signal power to be assumed constant. A sketch of the laboratory floor setup is shown in Figure 3.10. The setup demonstrates the different positions in which the Hovermap was placed to capture scans of the target surface located on the right of the image.

Figure 3.10: Schematic of the setup and scanning positions of the Hovermap (plan view)

The setup included screwing a threaded rod into the laboratory strong floor and securing it in place at the base with a nut. The (x, y, z) coordinate of the rod was fixed and served as the means of attachment for the specialised bracket that held the target in place. 3D point clouds of the different target surfaces were captured at various distances by shifting the Hovermap away from the target surface in fixed increments of 2 m, predetermined by holes in the laboratory strong floor. The holes in the strong floor were evenly spaced in a matrix formation with the distance between each hole centre measuring 0.5 m.

A mounting bracket for the Hovermap was 3D-printed, with a nut in the base of the bracket to screw it onto the threaded rod. Top and bottom views of the mounting bracket are shown in Figure 3.11. This bracket held the Hovermap in place during each scan and allowed for the scanner position to be shifted easily to adjust the distance to the target. The holes in the laboratory strong floor enabled repeatability among the different scans because the location of the rod, even when shifted from a different distance, always remained in the same location as the previous scan. Figure 3.12 shows the complete setup, with the target and Hovermap separated by a fixed distance.
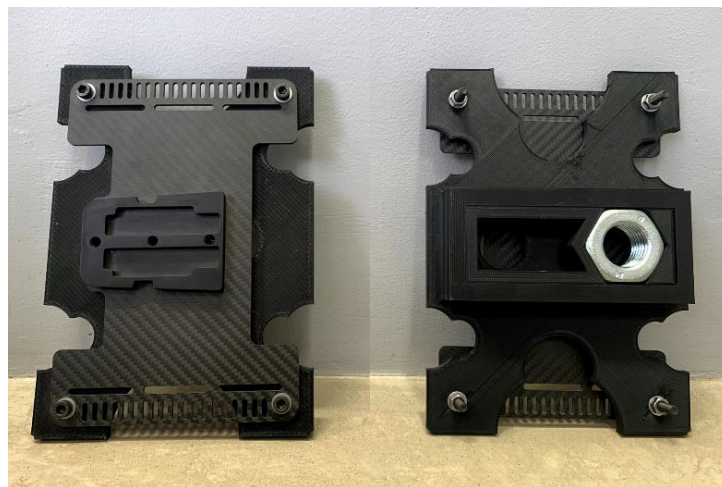
Figure 3.11: Mounting bracket for the Hovermap scanner

Figure 3.12: Setup of target and Hovermap

3.2.3 Preparation and mounting of targets

Each target was attached to the rod in the strong floor by means of a specialised bracket as shown is Figure 3.13. Markings on the nut of the bracket allowed for the incidence angle of each target to be adjusted with respect to the fixed position of the Hovermap. The height change in the z direction as the nut on the bracket was rotated, to alter the incidence angle, was negligible and therefore ignored.

Figure 3.13: Specialised rotating bracket

All concrete targets were attached to the rotating bracket by aligning the four bolts with the holes in the bracket and securing each bolt in place with a nut as shown in Figure 3.13. The colour targets used the same rotating bracket but a simpler means of attachment than bolts. Because these targets were significantly lighter than those made from concrete, small 3D printed slip-on attachments were made and glued to the back of each coloured target. Figure 3.14 shows an example of the 3D printed attachment glued to the back of the target. The gap between the attachment and the back of the target provided space for the specialised bracket to slip in.

(a)   (b)
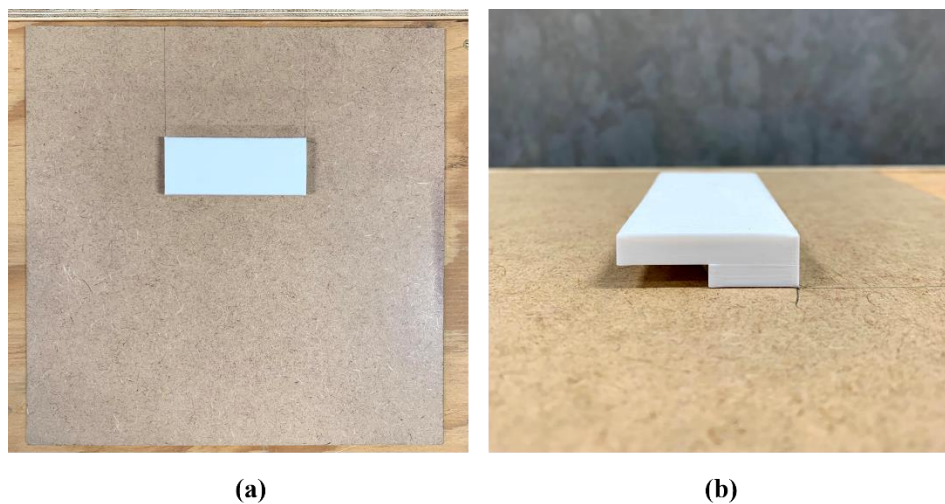
Figure 3.14: 3D printed attachment for colour targets – (a) Top view (b) Side view

3.2.4   Methodology and data capture

The methodology followed, focused on collecting point clouds of the different colour and concrete target surfaces and analysing the individual target point information, with particular attention to range and intensity values. For practical applications, such research is essential to better understand how these factors affect point cloud uncertainty.

The hardware used for the data collection was the Emesent Hovermap LiDAR system. The Hovermap was controlled by connecting to the wireless technology (WiFi) of the device and opening the web browser interface. Each scan was renamed, started and stopped remotely, and appended to the current scan list. The file was saved to Hovermap's onboard storage. Figure 3.15 shows the user interface, highlighting the features mentioned above.
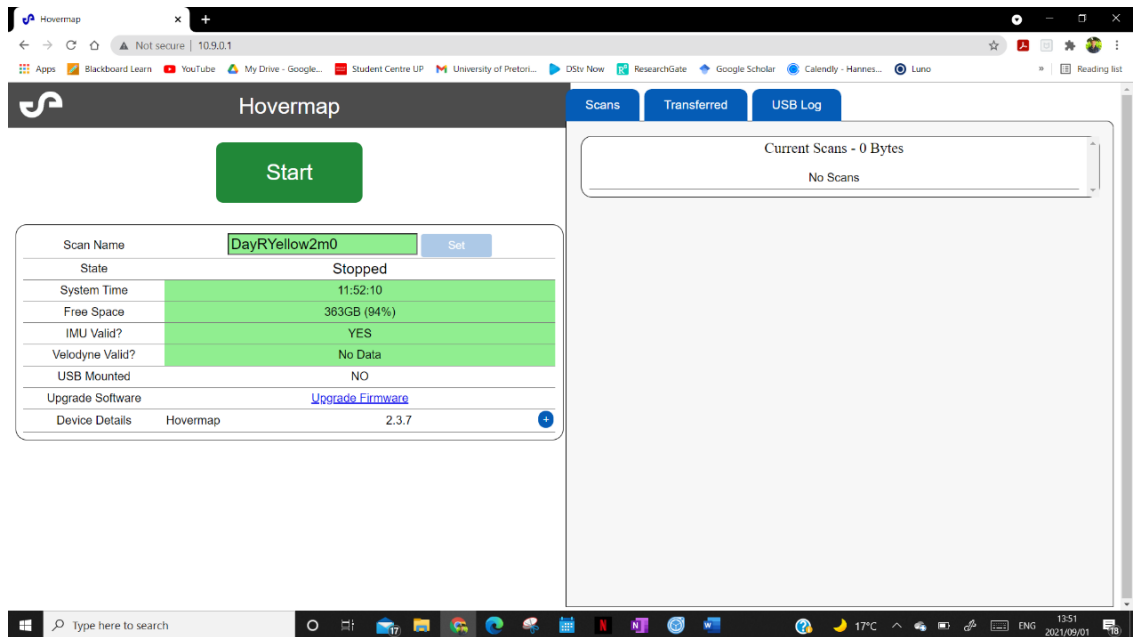
Figure 3.15: Hovermap web interface

The naming of each scan followed a specific format which made it simple to reference specific targets in Python when importing the point cloud data. Figures 3.16 and 3.17 show the scan product-naming sequence that was followed for the colour and concrete targets respectively.
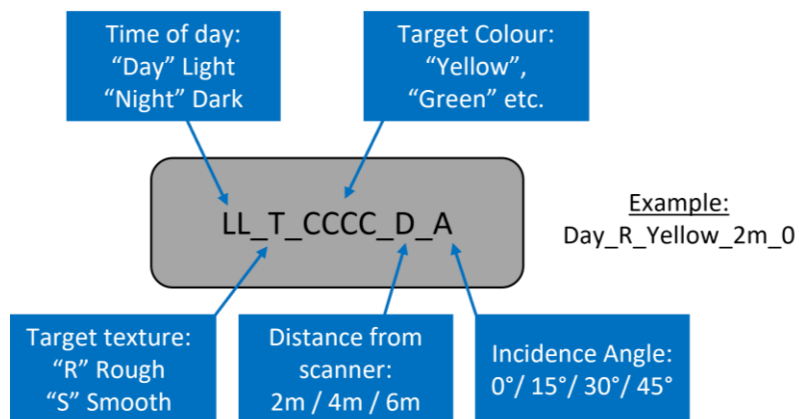
Figure 3.16: Scan product naming of colour targets
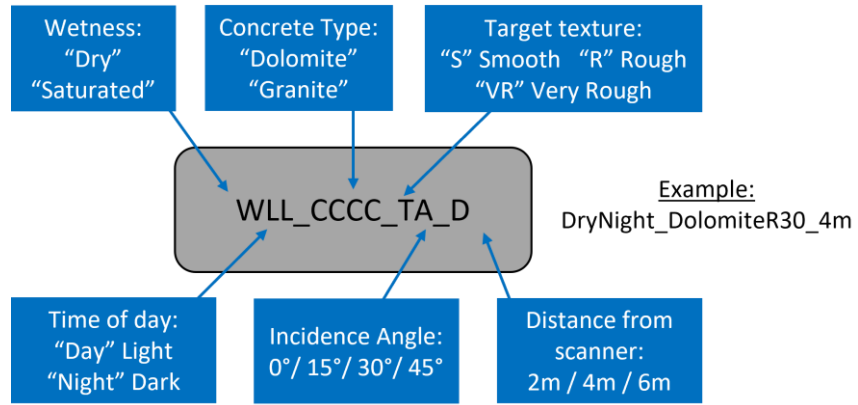
Figure 3.17: Scan product naming of concrete targets

In each setup a different target was scanned, with the incidence angle fixed at 0° or parallel to the Hovermap for the initial scan. Successive scans at different distances and incidence angles were then acquired. The test distances were 2 m, 4 m and 6 m, with incidence angles changed from 0° to 45° in 15° increments for each test distance. A total of 12 scans was collected for each of the different targets. All setups were created using the centre of each target as reference with an adjusted incidence angle, as illustrated in Figure 3.18. The planar targets were assumed to be level in the vertical. The incidence angle was only changed in the horizontal direction. Figure 3.19 shows a flowchart of the procedure followed to capture scans of each target. The duration of each scan was fixed at 30 seconds.
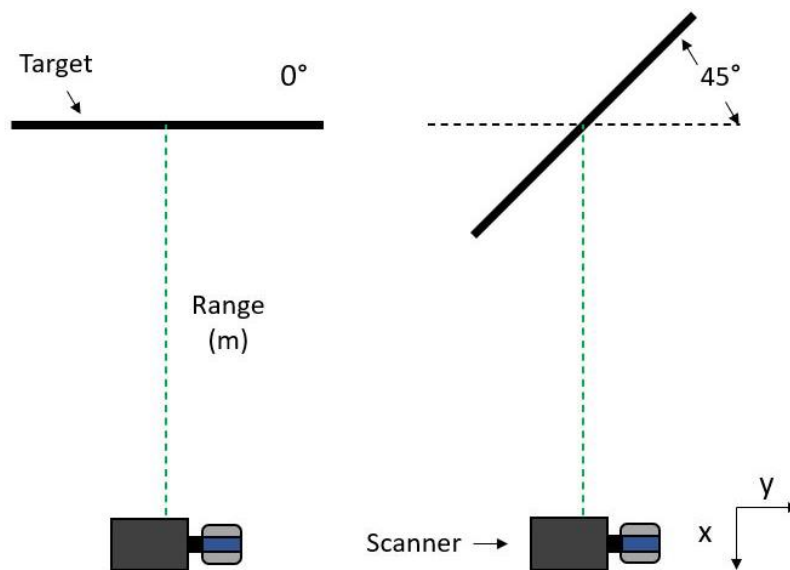
Figure 3.18: Target rotation from fixed scanning distance
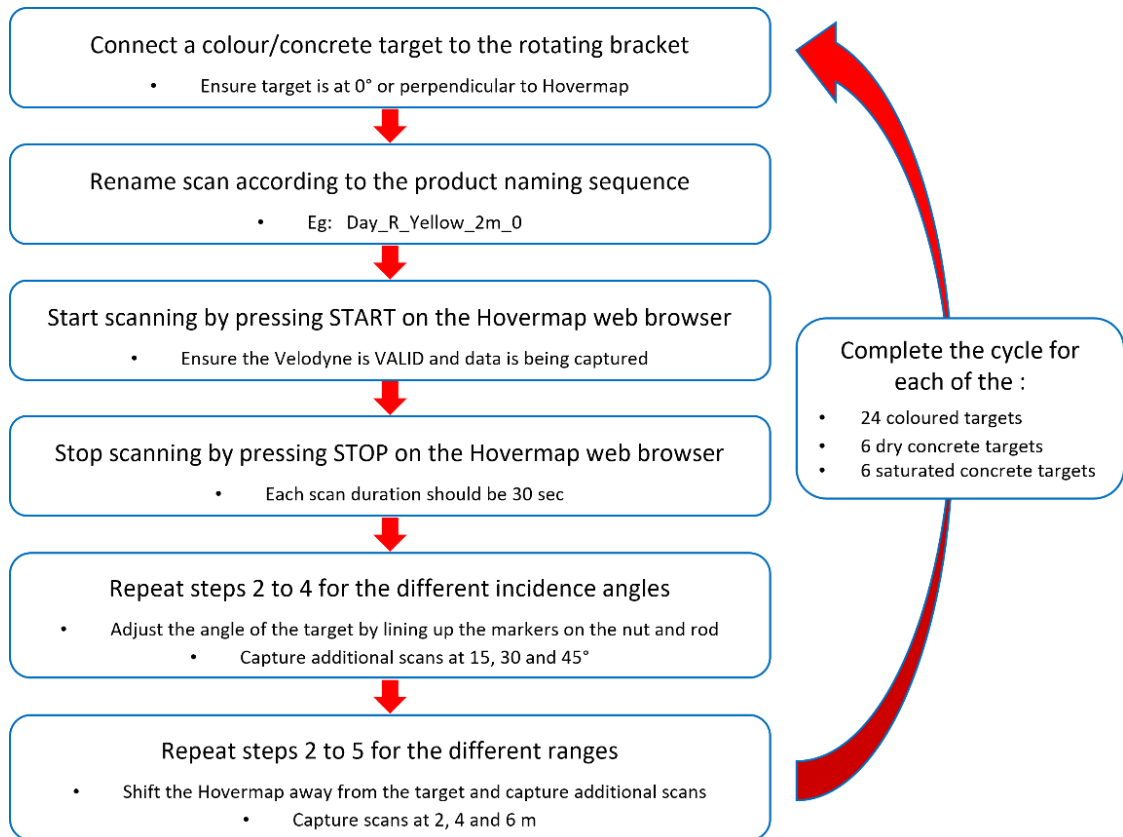
Figure 3.19: Flowchart of steps followed to capture target scans

Figure 3.20 shows the typical raw point cloud results obtained from one of the smooth concrete target scans.

(a)   (b)
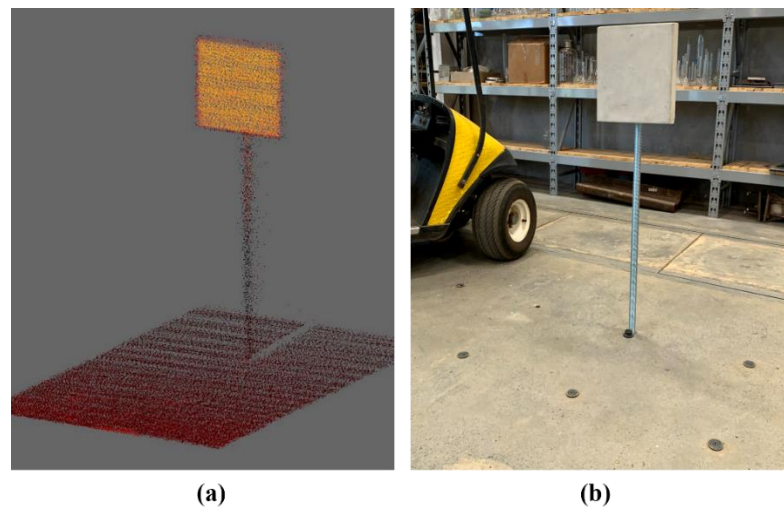
Figure 3.20: Example of a concrete target – (a) 3D point cloud (b) RGB image

3.2.5 Data filtering

All scans were saved to Hovermap's onboard storage and later transferred via USB to a secondary computer for further processing. A .laz point cloud file of each scan was generated by processing the scan in the Emesent software. Standard configuration settings were used. The only adjustment made was to the max intensity value, which was changed from 77 to 255. Once processed, these .laz files were all imported into third-party software to visualise, crop and export the individual quantitative point data. Cropping of the individual target surface from the rest of the point cloud was done manually. Thereafter, the coordinate and intensity information on the cropped points of the individual targets was exported as text files in .csv format. A Python script that automatically located, read and imported selected data from the text files was written to concatenate the data. The product-naming sequence made calling up information for plotting simpler and allowed numerous comparisons between different targets to be made.

Colour targets

A total of 12 scans were captured for each of the 24 coloured targets, which brought the total number of scans for all 24 coloured targets to 288. To investigate the influence that ambient lighting conditions had on range and intensity measurements, all 288 scans of the targets were repeated in the dark. Figure 3.21 shows the raw results of 12 rough colour targets taken in the day at a range of 2 m and a 0° incidence angle. The difference in intensity values between the different coloured targets is easily visible.
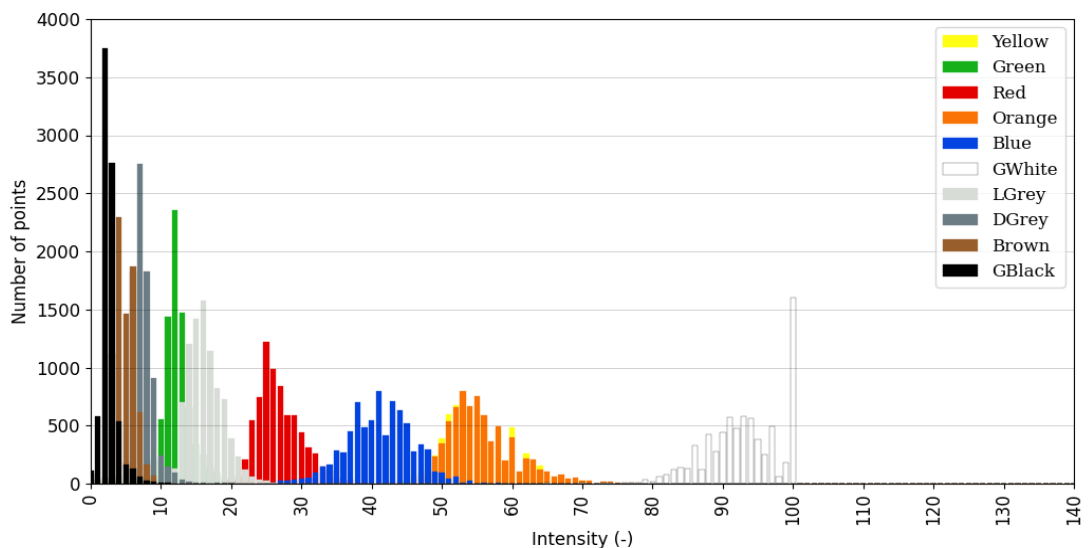
Figure 3.21: Intensity distribution of rough colour targets at 2 m and an incidence angle of 0°

Concrete targets

All concrete targets were scanned in two different states of saturation. For the first set of scans, the targets were saturated only by air humidity. Once captured, these scans were labelled with the prefix 'Dry'. To observe the effect of saturation on the returned intensity values and to provide a direct comparison between the different concrete surfaces, all six dry concrete targets were left to saturate in baths for a 24-hour period.

For the second set of scans, the targets were now fully saturated and scan names were labelled with a 'Sat' prefix. All targets were again scanned at different distance and incidence angles. Just like the coloured targets, scans of concrete targets in their dry and saturated states were repeated in the dark. Figure 3.22 shows one of the concrete targets undergoing saturation.

Figure 3.22: Concrete target saturating in bath

The difference in intensity values between the same concrete surface in different states of saturation was of special interest. Figure 3.23 shows the distribution of raw intensity values of the dolomite concrete targets scanned at 2 m and an incidence angle of 15°. The differences in intensity readings between the dry and saturated states, as well as the influence of surface roughness, are clearly visible.
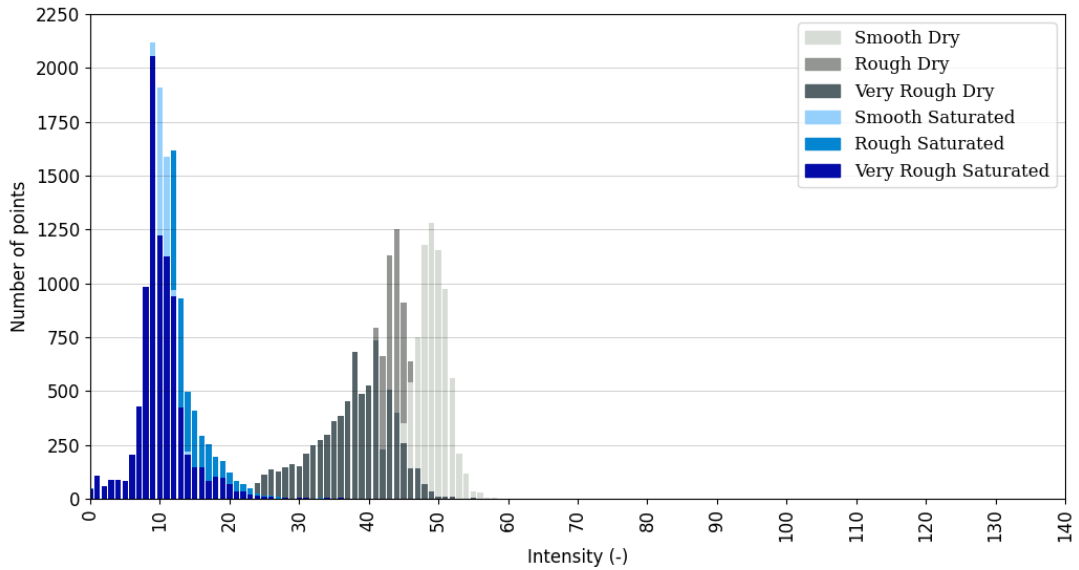
Figure 3.23: Dolomite intensity distribution at 2 m and an incidence angle of 15°

3.3 FIELD TESTING

The surveying of railroad tunnels is deemed to be critical for a number of reasons. Cross-sections, profiles, surface feature extraction, deformation mapping and as-built controls are key measures for effective rehabilitation and monitoring of these existing structures. Requests to understanding and gain deeper knowledge of a tunnel's current condition and to compare scans from different epochs against the existing structure make it essential to operate in the 3D environment.

This section aimed to assess the feasibility of the discussed laboratory testing to detect water leakage areas in real underground tunnel environments. The Emesent Hovermap was used to scan and generate 3D point clouds of different tunnel sections. The procedure followed to generate the point clouds and process the data is discussed further in this section. Although several defects and areas of moisture ingress found in tunnels are often hidden from view, the work presented here will focus only on those that are visible on the surface of the tunnel wall.

3.3.1 Site description and selection

Two sections along the Gautrain rapid rail line were selected for field testing. These tunnel sections were specifically chosen based on their condition and known surface finishes. The condition of the different tunnel sections by no means fully represents conditions found in all tunnels, but it does provide a good basis on which to evaluate and backup laboratory work.

Point cloud data was obtained for selected 50 m segments in the tunnel section from Park Station to Rosebank Station and a small section from Rosebank to Sandton Station. This entire tunnel section forms part of the southernmost end of the Gautrain network, starting just north of central Johannesburg in Parktown, as shown in Figure 3.24. The green and blue tunnel markers on the map indicate the location of the two different scanned sections.
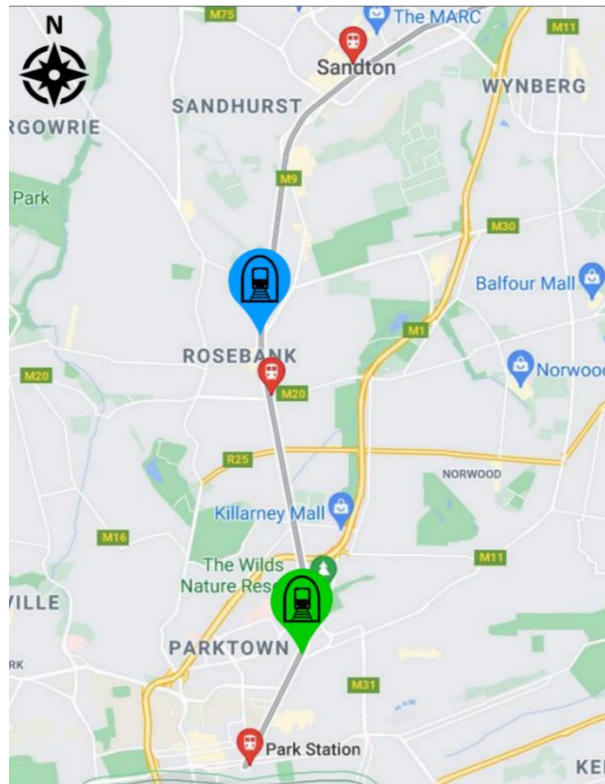
Figure 3.24: Location of scanned segments in relation to each station

The construction of tunnels along the Gautrain line was completed using two different construction methods. The cost-effective drill and ballast (DB) method was used for 90% of all tunnelling and the remaining 10% utilised a tunnel boring machine (TBM). The tunnel section from Park Station to Rosebank Station was excavated using the DB method and a small section just north of Rosebank in the direction of Sandton Station, was constructed using the TBM.

Figure 3.25 shows the internal structure of the tunnels constructed using the two different methods. Apart from the surface finish difference and non-constant circular profile of the DB section (green) compared to the TBM section (blue), other major targets in the scan area such as rails, pipes, lights and signalling all remained the same.
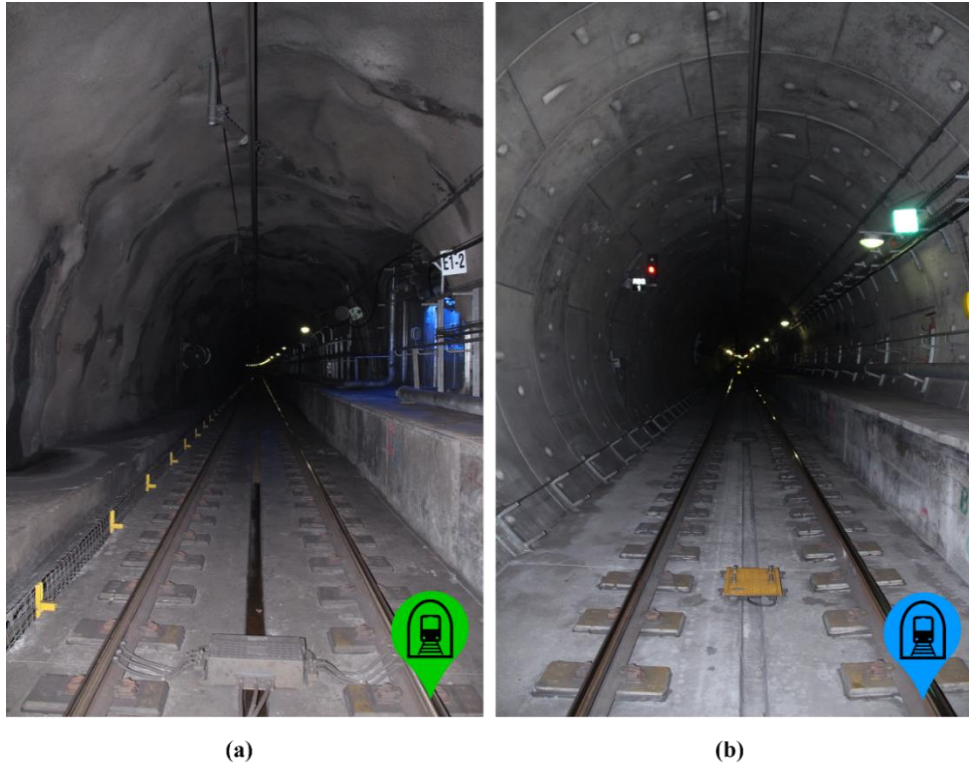
Figure 3.25: Internal view of tunnels constructed with (a) DB and (b) TBM methods

3.3.2 Scanning procedure

The scans were conducted manually in handheld mode for each tunnel section to show proof of concept, but could just as easily have been drone- or vehicle-mounted. The Hovermap was positioned parallel to the tunnel walls with the LiDAR puck pointed in the track direction. Scans were collected by walking along the centre of the track, as shown in Figure 3.26.

Figure 3.26: Capturing of point cloud data in TBM tunnel section

Depending on the time available and the level of detail required by the inspector, the speed of scans can be easily adjusted. The only effect would be a decreased point density for scans collected at a faster speed. For the sake of simplicity, a walking speed of roughly 0.5 m/s was adopted. Both tunnel sections were scanned between the engineering and maintenance hours of 22:00 and 04:00 on 29 and 30 July 2021

3.3.3   Data filtering

The same process was followed, as explained in Section 3.2.4, to generate the .laz point cloud files. These point cloud files included information on the 3D coordinates and original intensity values of each point in the point clouds, recorded in 8 bits [0, 255]. A Maptek project containing all the files was opened and a workflow created to automate the filtration, separation and isolation of low intensity points. These points were then used to generate complex 3D surfaces of the water leakage areas. Basic Python commands and scripts were included to filter through these 3D surfaces and delete individual areas below a set threshold.

Range and intensity filter

An extended python script was used to apply a super filter to both range and intensity data of the tunnel section, as seen in Figure 3.27. Points on the tunnel walls were extracted and saved as a new file before the filtering of possible water leakage areas.
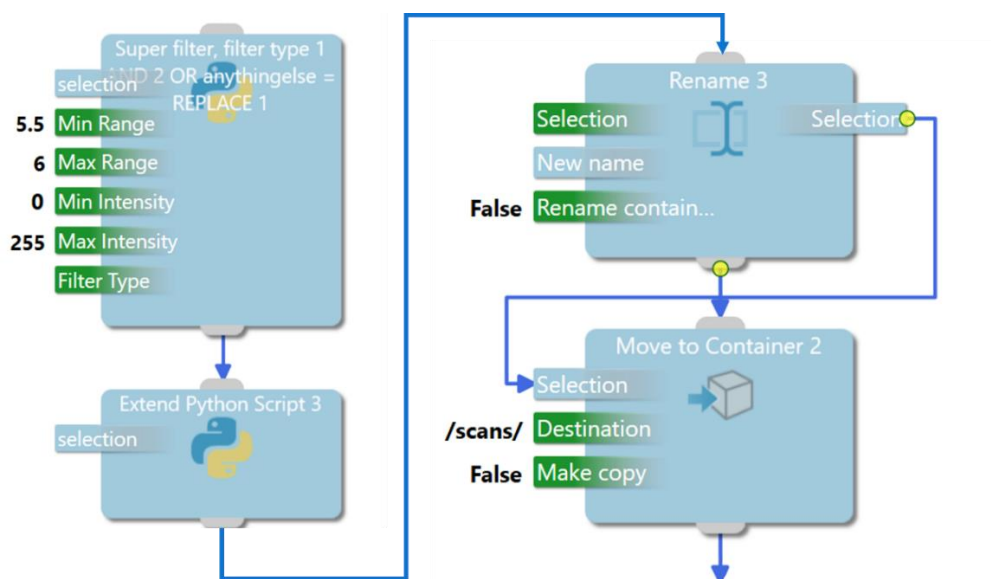
Figure 3.27: Range and intensity filter (Maptek, 2021)

Proximity filter

A best-fit surface was estimated for the tunnel walls and a proximity filtered applied to remove points further than 60 mm from this surface. The proximity filter is shown in Figure 3.28.
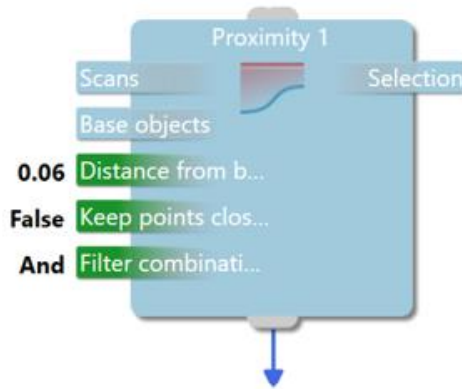
Figure 3.28: Proximity filter (Maptek, 2021)

Minimum separation filter

To remove duplicate and redundant points, a minimum separation filter was applied as shown in Figure 3.29. This was done to reduce point cloud size and improve triangulation of complex surfaces in the subsequent stages of the workflow.
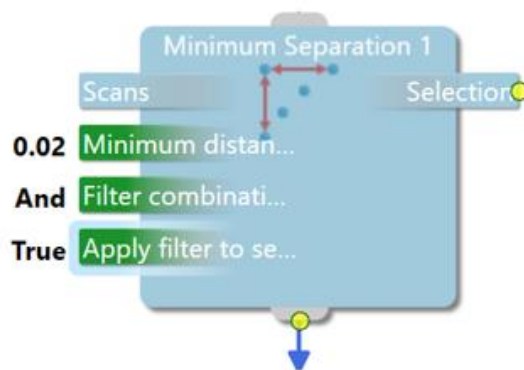
Figure 3.29: Minimum separation filter (Maptek, 2021)

Isolated points

Points greater than 60 mm away from any other points, in 3D space, were deleted. This was done to reduce point cloud noise. The isolation filter is shown in Figure 3.30.
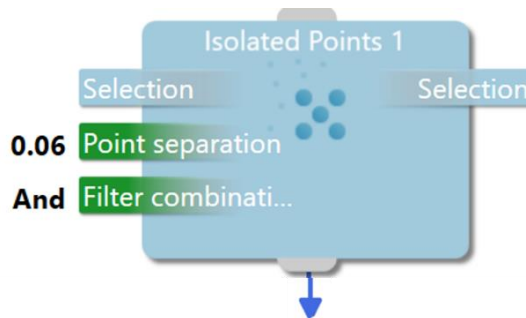
Figure 3.30: Isolated points filter (Maptek, 2021)

Triangulation

Complex 3D surfaces were generated using triangulation with a feature size of 200 mm and a smooth surface finish as presented in Figure 3.31.
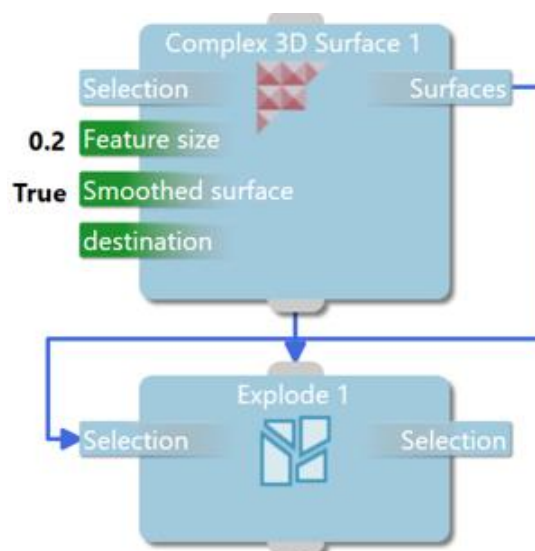
Figure 3.31: Triangulation of complex 3D surface (Maptek, 2021)

Surface area filter

Complex 3D surfaces were filtered to remove objects such has pipes and cabling that may have been mistakenly identified as possible water leakage areas. Each generated surface was checked against tolerances, with surfaces greater than 0.1 m^2 and point densities above 30 pts only retained. An extract of the code used to filter these surfaces is shown in Figure 3.32.

X, Y and Z span properties of each generated surface were also reviewed. If the X or Y span was greater than the Z span, the surface was deleted. Leaks on tunnel walls run vertically so it was a fair assumption to make that the Z dimension of the surface should be greater than that of the X and Y surface dimensions. The Maptek workflow for surface area filtering is shown in Figure 3.33.

```python
import numpy as np
from mapteksdk.project import Project
from mapteksdk.data import Surface

def area(surface):
    # 'triangles' = [[[x1,y1,z1],[x2,y2,z2],[x3,y3,z3]],]
    # Break out p1, p2, p3 for convenience
    triangles = surface.points[surface.facets]
    p1, p2, p3 = triangles[:, 0, :], triangles[:, 1, :], triangles[:, 2, :]
    Area = 0.5 *(-p2[:,1]*p3[:,0] + p1[:,1]*(-p2[:,0] + p3[:,0]) + p1[:,0]*(p2[:,1] - p3[:,1]) + p2[:,0]*p3[:,1])
    return np.sum(Area)

def check_surface(surface, min_area, min_pts):
    if surface.point_count < min_pts:
        return False
    if area(surface) < min_area:
        return False
    return True

if __name__ == "__main__":
    proj = Project() # Connect to default project
    tri_min_area = 0.1
    tri_min_pt = 30

    selection = proj.get_selected()
    # Use contextlib ExitStack to work with several 'with' contexts simultaneously
    to_delete = []
    for item in selection:
        if item.is_a(Surface):
            with proj.read(item) as surface:
                if(check_surface(surface, tri_min_area, tri_min_pt) == False):
                    to_delete.append(surface.id)

    for item in to_delete:
        proj.delete(item)
```

Figure 3.32: Surface area filter code
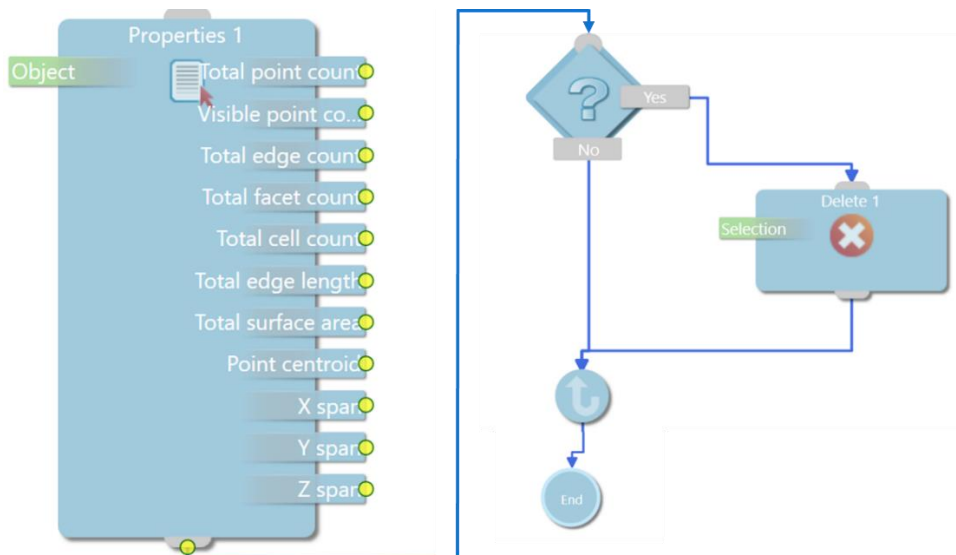
Figure 3.33: Surface area filter (Maptek, 2021)

3.3.4 Summary

Of the sections scanned, the DB section from Park Station to Rosebank Station experienced the most extensive water leakage. Figure 3.34 shows an internal point cloud of a small 20 m segment of this section. The point cloud is coloured by intensity, with 'hot intensity' as the chosen colour scheme in Maptek. The darker regions represent possible water leakage areas. Figure 3.35 provides a summary of the full workflow used to extract water leakage areas from the raw point cloud.
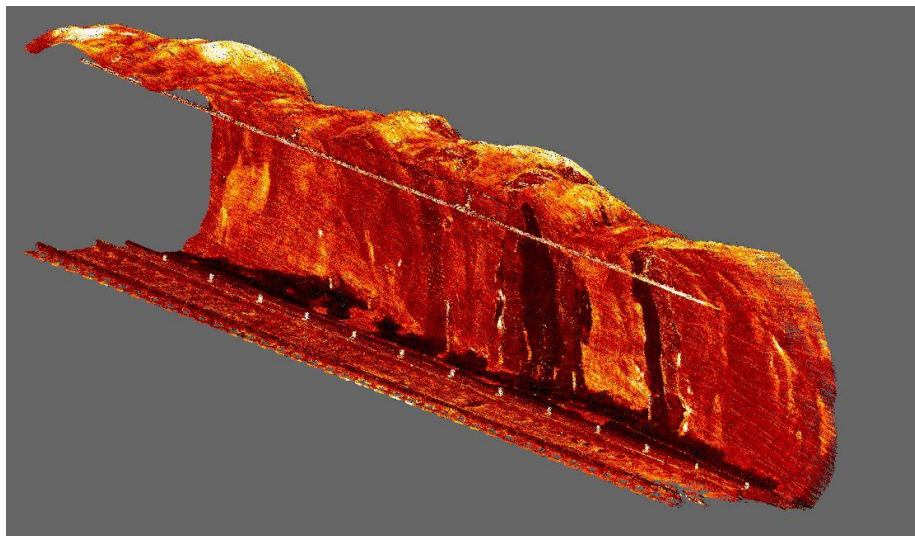
Figure 3.34: Raw point cloud of DB tunnel segment

Raw point cloud

Filter by range and intensity values
- Range (5.5-6m) and intensity (0-255)
- Rename filtered points as new scan '_walls'

Filter possible water leakage areas
- Range (5.5-6m) and intensity (0-2)

Proximity filter
- Deletes points further than 60 mm from best-fit surface

Minimum separation filter
- Points < 20 mm of another are filtered out to reduce cloud size

Isolated points
- Points > 60mm from any other point are deleted to reduce noise

Triangulation of complex 3D surfaces
- 3D triangulation set to 200 mm

Surface area filter
- Minimum surface area > 0.1 m^2 and point count > 30 pts.
- Filter and delete areas below set tolerances

Water leakage results
- Area and x,y,z coordinates of water leakage

Figure 3.35: Automated workflow for the processing of tunnel point cloud data

4 RESULTS AND DISCUSSION

This section provides a thorough interpretation and discussion of both the laboratory tests and field experiment results. The scan pattern of the Hovermap is analysed before selecting a scan orientation and duration. This is followed by a detailed discussion on the influence of target colour on range estimates and intensity values. Point cloud results of concrete targets are also reviewed with particular attention to roughness and degree of saturation. The section is concluded with an evaluation of the field tests done on operational railway tunnels to assess the applicability of extracting water leakage areas based on intensity data alone. All data was obtained by analysing point clouds generated using the Hovermap LiDAR system.

4.1 SCAN PATTERN

Figure 4.1 shows the results of the scan patterns produced against two adjacent concrete walls for 10, 20 and 30 second scan durations respectively. The complexity of the overlapping multiple beams during rotation generates uneven distributions, which is further influenced by scanner orientation. The complexity of the scan pattern is visible in Figure 4.1 (a).
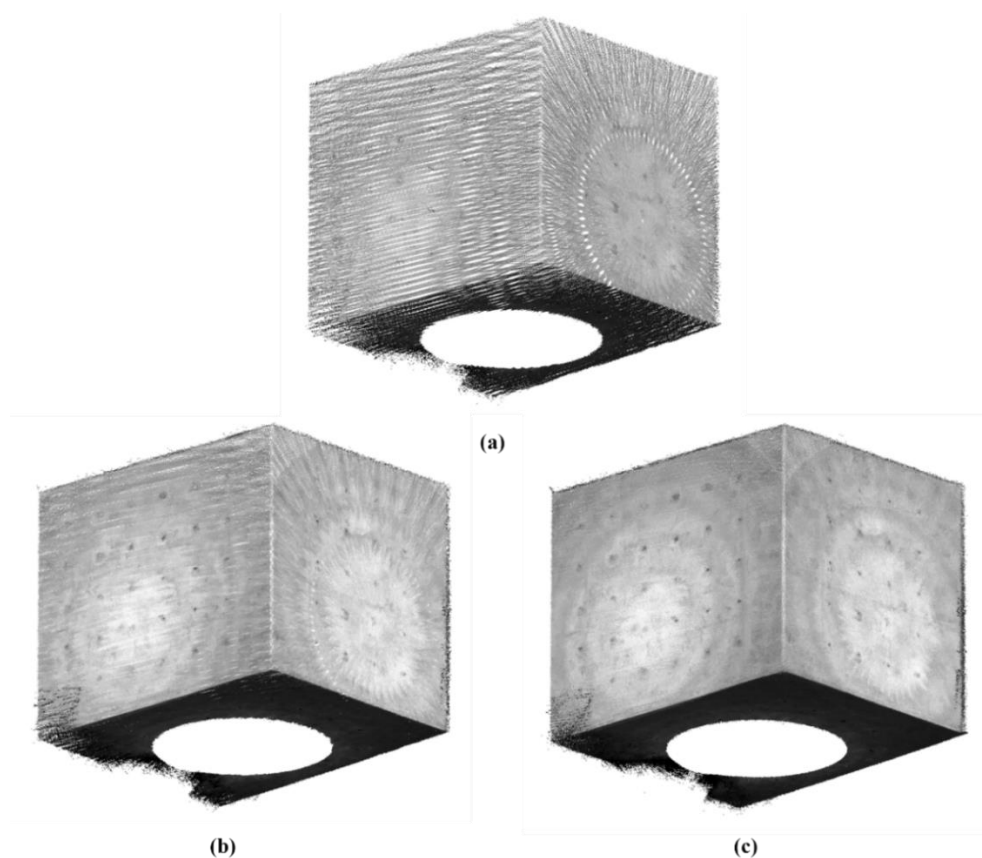
Figure 4.1: Visualization of point pattern distribution: (a) 10 s (b) 20 s (c) 30 s

For the purpose of this research, a thorough review of the scanning pattern fell outside the scope of work. The difference in patterns between the two adjacent walls along with the scanner's orientation was qualitatively considered, with particular attention to the intended purpose of the study. For this reason, the scanner orientation was fixed parallel to all scanned targets as would be the orientation when conducting tunnel scans. This orientation also eliminated the need to consider the blind spot directly perpendicular to the scanner as seen in Figure 4.2. The duration of the scans was chosen and fixed at 30 seconds, as it provided a more complete point cloud.
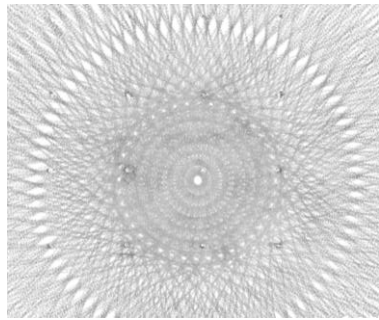
Figure 4.2: Point pattern with blind spot in the centre

4.2   COLOUR TARGETS

Initial laboratory testing was conducted on different colour and sheen targets with both a smooth and rough surface finish. For quality assessment of the captured point clouds, the standard deviation and mean values of range and intensity were selected. A spectroscopy analysis of the different coloured targets was carried out to provide a sound backing for the observed intensity results.

4.2.1   Spectroscopy analysis

The full range of measured wavelengths were cropped, with focus given to the 860 to 940 nm wavelength range as this range contained the Hovermap's wavelength of 905 nm. The results presented in Figure 4.3 qualitatively display the reflectivity difference between the coloured targets with a smooth surface finish. The results of the rough targets were the same but with an overall decreased magnitude of reflectance for all colours. This makes intuitive sense as the roughness of a surface affects the proportion of diffuse and specular reflectance components. Rougher surfaces have a greater diffuse component and lead to an even scattering of the incident beam and a lower received energy backscatter. This concept is detailed in Figure 2.15.

The white and black targets recorded the highest and lowest reflectance values respectively. The high recorded reflectivity values of white show it is dominated by a high reflectance component. This is different to black which tends to absorb more light energy, reflecting less back to the receiver and recording a lower reflectance value, as seen in Figure 4.3. A similar order of reflectance was observed by Suchocki and Katzer (2018) and Bolkas (2019) for semi-gloss and matte sheen colours. The prefixes "M" and "G" are used to distinguish between the matte and semi-gloss sheens respectively for the white and black colours. The two shades of grey colours are also distinguished by light "L" or dark "D" pigments. All other colours were applied with a semi-gloss finish.
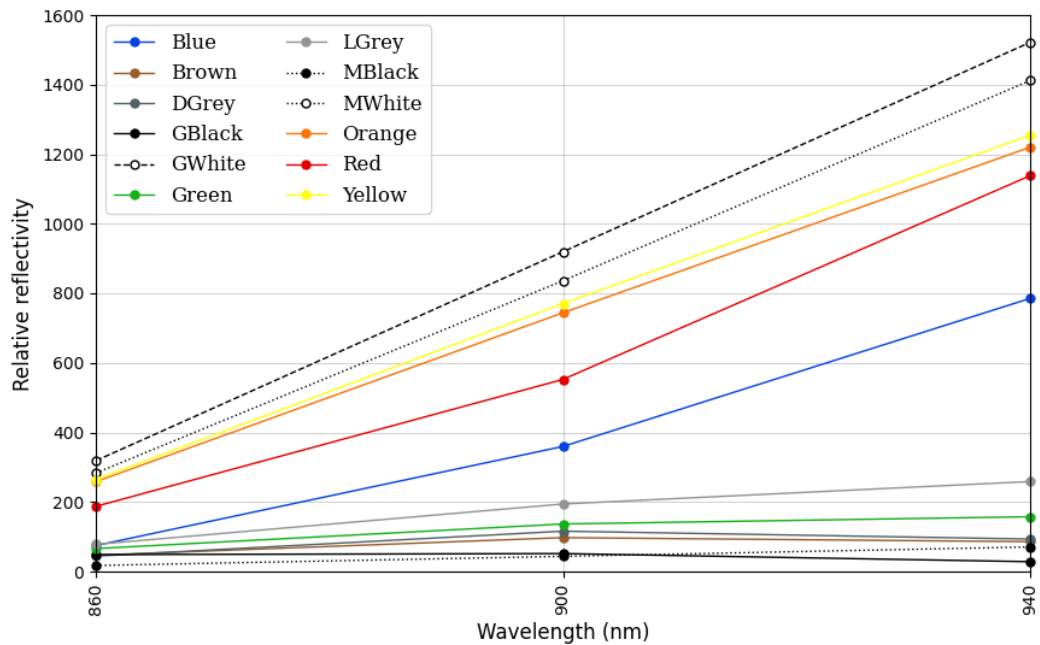
Figure 4.3: Reflectivity of smooth coloured targets

The percentage change in reflectance between smooth and rough coloured targets is shown in Figure 4.4 for the 900 nm wavelength. A decreased reflectivity was recorded for all rough coloured targets. This decrease ranged from 28.5% for GWhite to 65.4% for Green with an average reduction in reflectivity of around 44.3%. The spectrometry analysis was done to later refer to and observe any correlations between the target's reflectance and measured range and intensity values.
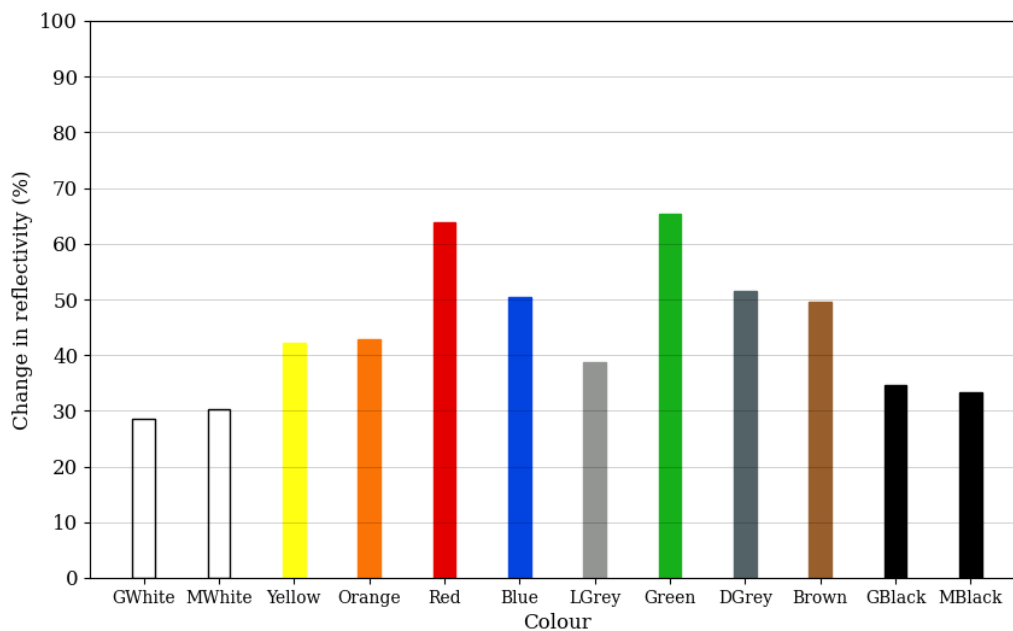
Figure 4.4: Change in reflectance between smooth and rough coloured targets

4.2.2   Range estimates

The geometric accuracy of point clouds and how this is affected by object colour and roughness is important as it provides a greater understanding of the inherent uncertainty associated with point clouds. This subsection deals with results captured at 0° incidence angle where the largest standard deviation (SD) of range measurements were observed.

An estimate of each target range from the scanner was determined using an adjusted plane (best-fit) and calculated by taking the average range of all points that appeared on the target surface. To analyse the accuracy of this measurement the SD was derived based on each point's residual distance to the best-fit plane. The influence of angular errors on the SD is less pronounced and rather more significantly affected by the target colour and roughness. Such was also noted and observed by other research groups (Voegtle and Wakaluk, 2009; Bolkas and Martinez, 2017).

Figure 4.5 and 4.6 shows the dependence on colour brightness, where the SD of range measurements are higher for black targets compared to the rest. This agrees with previous research which stated that the best and worst performance was measured for yellow and black targets, respectively (Bolkas and Martinez, 2017).
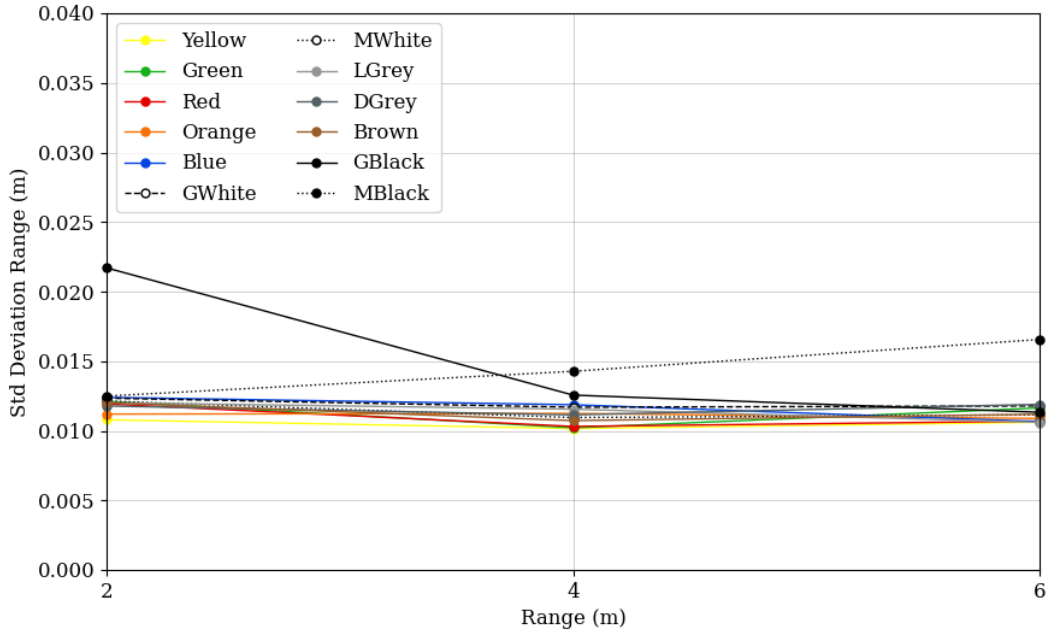
Figure 4.5: SD of range for smooth coloured targets at 0° incidence angle
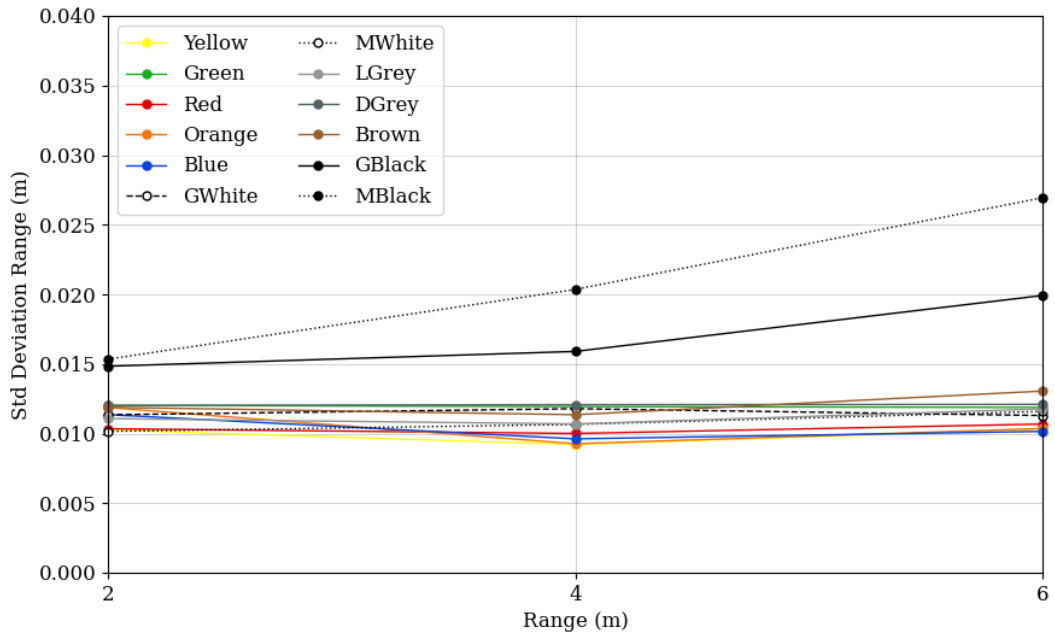
Figure 4.6: SD of range for rough coloured targets at 0° incidence angle

The SD for all coloured targets is below 30 mm which is the published accuracy of the scanner. The individual SD measurements of all targets, shown in Figure 4.5 and 4.6 above, are tabulated in Table 4.1. The colours are ordered in increasing reflectivity from black to white as measured in the spectroscopy analysis.

All coloured targets, albeit black, remain somewhat stable with increasing distance. The SD is bound between 9.2 and 13.0 mm for both smooth and rough finishes, whereas black varies between 11.3 and 26.9 mm. The difference in precision ranking amongst the coloured targets is expected as darker colours absorb more incident energy and thus reflect less energy back to the receiver, resulting in noisier range measurements. Apart from black targets, difference in the SD of range measurements between smooth and rough targets is less than 1.5 mm.

Table 4.1: Standard deviation (mm) of range for different coloured targets

Colours ordered by Reflectivity	Smooth			Rough		
	2m	4m	6m	2m	4m	6m
MBlack	± 12.5	± 14.3	± 16.6	± 15.3	± 20.3	± 26.9
GBlack	± 21.7	± 12.6	± 11.3	± 14.8	± 15.9	± 19.9
Brown	± 12.0	± 10.7	± 11.2	± 11.9	± 11.3	± 13.0
DGrey	± 11.8	± 11.1	± 11.9	± 12.0	± 12.1	± 12.1
Green	± 12.1	± 10.2	± 11.6	± 12.0	± 11.9	± 11.9
LGrey	± 12.0	± 11.6	± 10.6	± 11.1	± 10.7	± 11.8
Blue	± 12.4	± 11.9	± 10.7	± 11.4	± 9.6	± 10.2
Red	± 11.9	± 10.3	± 10.7	± 10.3	± 10.0	± 10.7
Orange	± 11.1	± 11.2	± 10.9	± 11.9	± 9.3	± 10.4
Yellow	± 10.8	± 10.2	± 10.6	± 10.3	± 9.2	± 10.3
MWhite	± 12.1	± 11.0	± 11.1	± 10.2	± 10.7	± 11.6
GWhite	± 12.3	± 11.7	± 11.8	± 11.3	± 11.8	± 11.3

An increase in SD from 2 to 6 m is observed for all black coloured targets. The matte and semi-gloss rough black targets record a 35 % higher SD on average for the 2 m scans compared to the rest of the coloured targets and seem to increase linearly and exponentially with distance. The smooth semi-gloss black target, however, does not follow a similar trend. The scan captured at 2 m produced SD measurements of order of magnitude double that of other smooth targets at the same distance, as seen in Table 4.1. Instead of the SD increasing with increasing distance, there is a sudden drop at 4 m which decreases further for the scan captured at 6 m. To better explain the high SD of the smooth semi-gloss black target, the point density of each target was considered. The point density of all smooth targets is shown in Figure 4.7. An exponential decrease in point density with increasing distance is observed for all targets. While the point density does not seem to be affected significantly by most surface colours, the semi-gloss black target experiences a significant drop between 2 and 4 m where the point density decreases from around 6500 to 290 points.

Additional point clouds of the same smooth black target were captured for each distance to test repeatability, with results showing large variability in SD but similar point density counts. This large drop in point density is identified as one of the main reasons for the erroneous SD measurements of the smooth semi-gloss black target in Figure 4.5. The lack of points and typical noise associated with the semi-gloss black surface meant there was little to no repeatability between successive scans. Scans of objects where precise measurements of range are required should thus be painted with brighter colours.
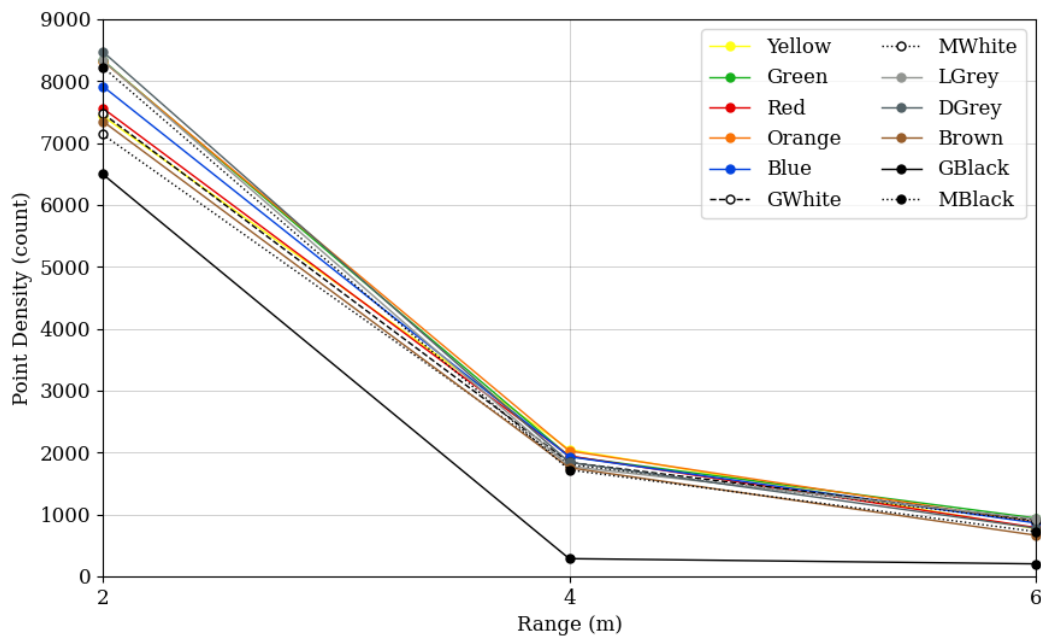
Figure 4.7: Point density of smooth targets scanned at different distances

Ambient lighting

The difference between measurements taken orthogonally at 2 m in the day and night-time for both smooth and rough coloured targets are shown in Figure 4.8. All targets recorded a SD of approximately greater than or equal to 10 mm with only semi-gloss black recording a deviation of above 15 mm. The difference in SD of each target scanned in the day and again at night is less than 0.75 mm and 0.84 mm, on average, for smooth and rough targets respectively. Apart from smooth semi-gloss black where a difference of 3.2 mm was measured, 80% of all other targets recorded a difference below 1 mm for the different lighting conditions. This did not agree with work done by Voegtle et al. (2008), who noted a significant difference in SD between scans conducted in the day and night-time (approximately by a factor of 2).
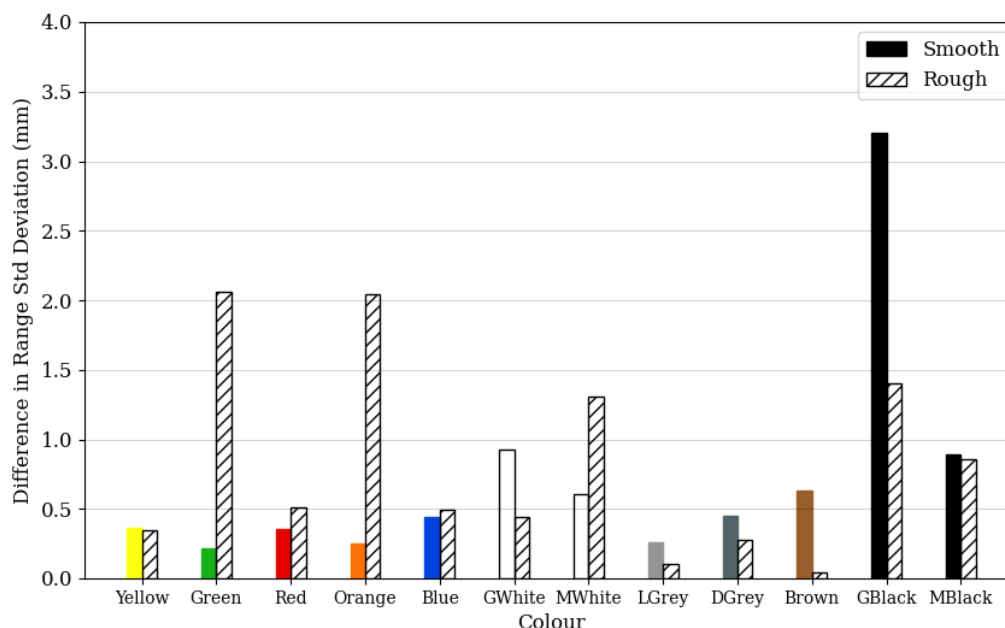
Figure 4.8: Difference in range accuracy for smooth and rough coloured targets scanned in different ambient lighting conditions

Similar results were obtained for the 4 and 6 m distances, with the max difference recorded for the rough matte and semi-gloss black targets at 6 m. These targets recorded a 6 mm difference between scans in different lighting conditions. In contrast to results obtained from previous work by Voegtle et al. (2008), where the SD difference was halved for the black target scanned at night, no clear indication of a change in range accuracy for scans conducted in different ambient lighting conditions could be proved. It must be noted that the TLS used by Voegtle et al. (2008) had a wavelength of 532 nm (green) and range accuracy of +/- 7 mm.

Even though semi-gloss and matte black have shown to have high variability between measurements, the total SD of each target is still less than the scanner's accuracy of 30 mm for tested distances less than 6 m.

4.2.3 Intensity

This section discusses laser scanner intensity, which accompanies 3D coordinate information, and is the focus of the dissertation. Extant studies analyse and describe the phenomenon of colour and its effect on the value of intensity, however the lack of results relating to the scanner used in this research meant this had to be tested. For analysis of the recorded intensities, the mean and standard deviation of intensity was computed and used.

The incidence angle effect on intensity was evident for all targets, but more significant for smooth targets. The results from the 4 m distance scans are shown in Figure 4.9 and 4.10. Similar trends were also observed for the other tested distances. Average intensity readings all decrease with increasing incidence angle, with a stronger decrease observed for brighter coloured targets.

The white and black matte colours, although they have the same sheen, produced different results. The matte white target showed a similar decreasing trend as the semi-gloss white but with slightly lower average intensity readings and a decreased spike at 0° for the smooth target case. The difference between matte and semi-gloss black was considerably more noticeable, particularly for the smooth targets. The matte black target was the only colour to not show a spike in intensity at 0° and remained somewhat unchanged with increasing incidence angle for both the smooth and rough targets. Average intensities of the same colour for a rough target compared to the smooth target were all lower, with the deviation again greater for brighter colours.
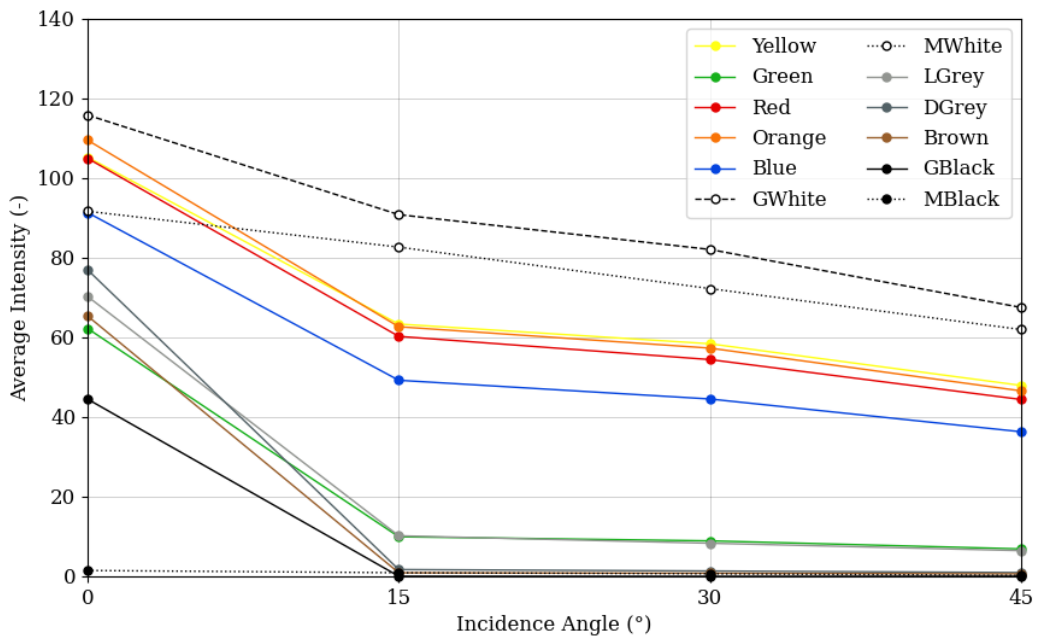
Figure 4.9: Average intensity of smooth coloured targets at 4m distance
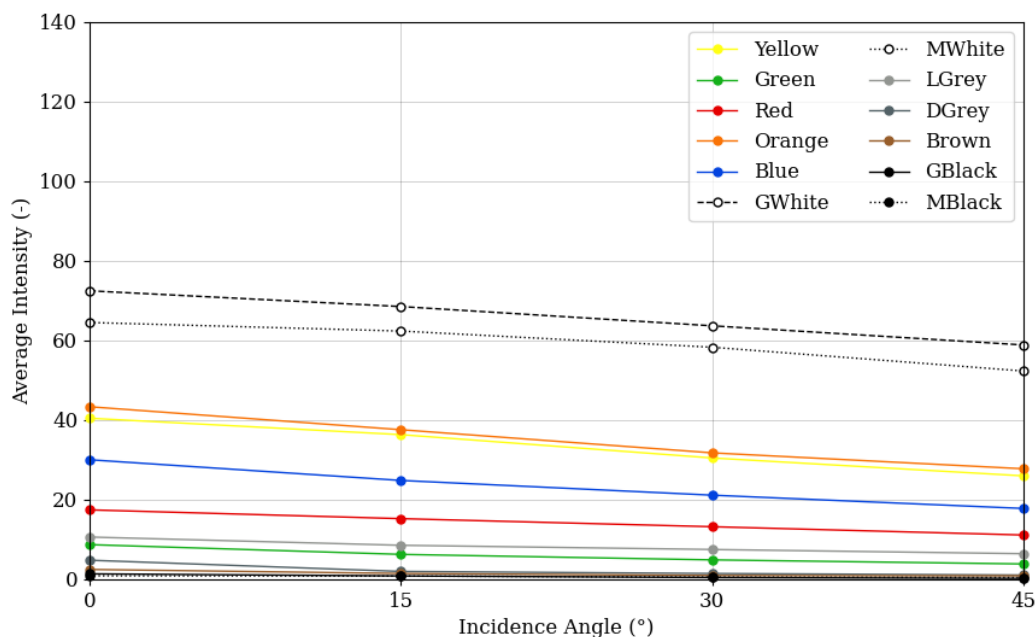
Figure 4.10: Average intensity of rough coloured targets at 4m distance

The spike in intensity readings is significant for all smooth semi-gloss targets at 0° in Figure 4.9. This same phenomenon is however not observed for the rough targets. This is mainly due to the different reflections caused by the change in roughness between the targets. Smooth targets have a higher specular reflection component which causes an increase in backscatter energy and at angles close to zero this is especially evident. Tan et al. (2018) observed the same specular reflections for geometrically smooth target surfaces scanned at normal incidence angles. This observation was termed the highlight phenomena i.e., the intensity data of a region on the scanned surface has a higher intensity than the rest of the target, although the whole target has the same reflectance characteristics. This phenomenon is seen as a bright spot that appears on the target surface and was observed for all smooth targets, albeit matte black. The points contained in these spots exhibited significantly higher intensities which in turn lead to higher average intensity readings as seen in Figure 4.9 at 0°. Figure 4.11 shows an example of the associated bright spot on one of the target's raw point clouds, coloured by intensity.
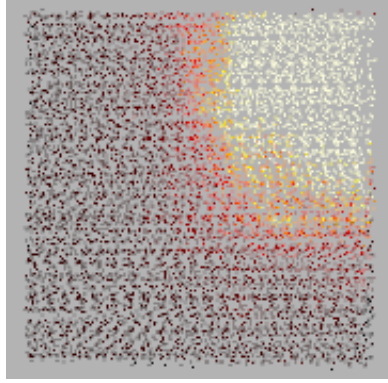
Figure 4.11: Bright spot at 0° incidence angle

A summarised version of the average intensity for each target is shown in Figure 4.12. This data agrees with the results of the spectroscopy analysis in Figure 4.4 and follows the same order of decreasing reflectivity. The only noted difference between the spectroscopy and intensity data was for the rough red target, which recorded a lower average intensity compared to the blue target. This change in order of reflectance may be due to the underlying colour of the sandpaper, used to resemble the rough surface, being black. The red paint may not have covered the rough surface in full and with the difference in sensitivity between the spectrometer and LiDAR, a lower intensity value was recorded.
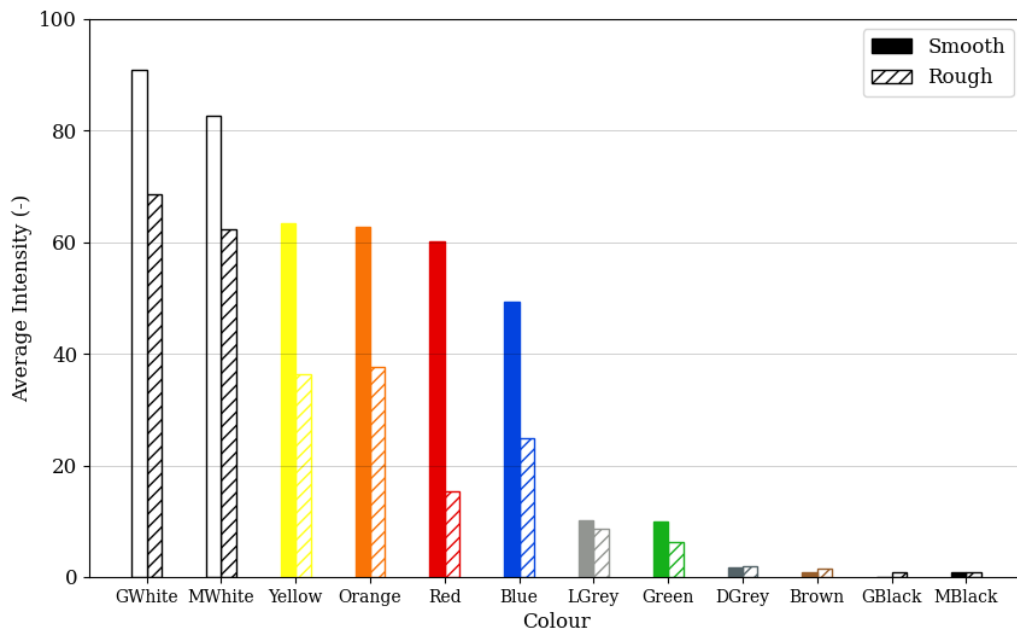
Figure 4.12: Average intensity of smooth and rough targets at 4m and 15°

All drab colours from dark grey to black recorded similar low intensity values under 5 units. Figure 4.12 proves that by analysing the intensity information of a surface, areas of darker colours are distinguishable. Filtering and colouring point clouds by intensity should, in theory and proven by the coloured target tests, be possible.

Ambient lighting

Figure 4.13 shows the measured point cloud intensities of smooth coloured targets generated in light and dark environments at 4 m and 15° incidence angle. Like range estimates, a negligible difference in intensity readings were observed with a max difference of 3 intensity units recorded. Rough coloured targets showed similar results. The small difference proves that ambient lighting has no remarkable effects on recorded intensity. Results confirm and back up statements made by other research groups (Voegtle et al., 2008; Voegtle and Wakaluk, 2009; Tan et al., 2018). Although all researchers used scanners of differing wavelengths, which is known to influence the absolute intensity values, the difference between intensity readings in different lighting conditions were all negligible.
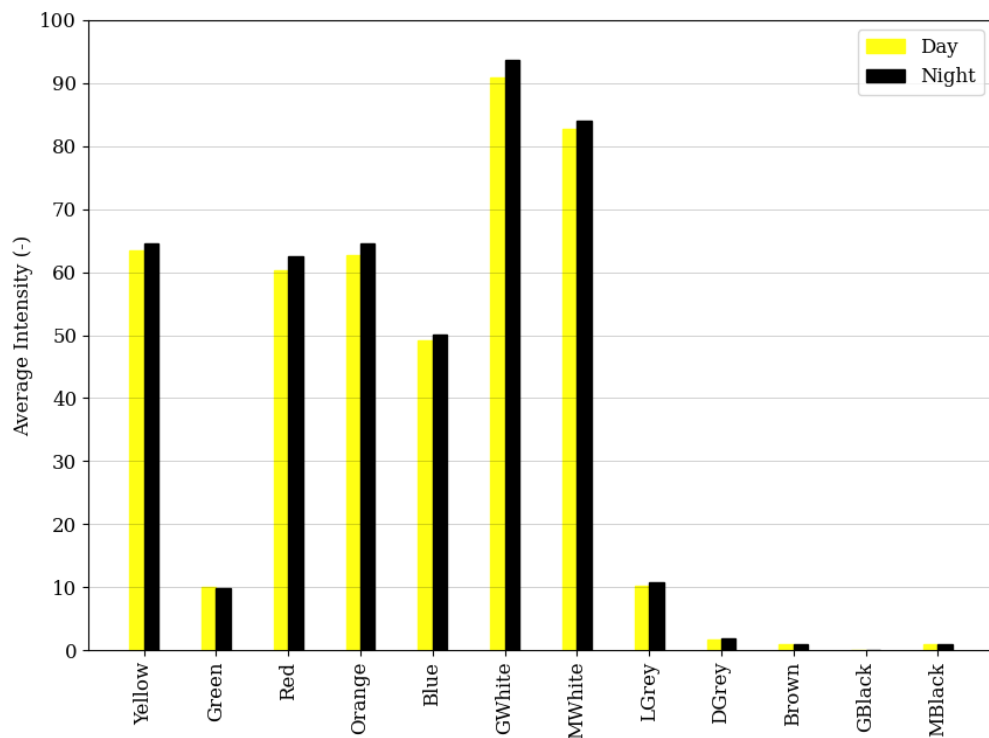
Figure 4.13: Average intensity for smooth coloured targets in different ambient lighting, at 4m and 15°

The highlight phenomena, caused by the high intensity readings at 0°, was also investigated in different lighting conditions with the results presented in Figure 4.14. The results showed that lighting had little to do with the observation seen in Figure 4.11. This meant that the bright spots observed at 0° were as a result of the spectral surface properties of the smooth semi-gloss targets and lighting had little to no influence on this observation. Rough targets angled at 0° showed similar results to targets angled at 15° with no spikes observed.
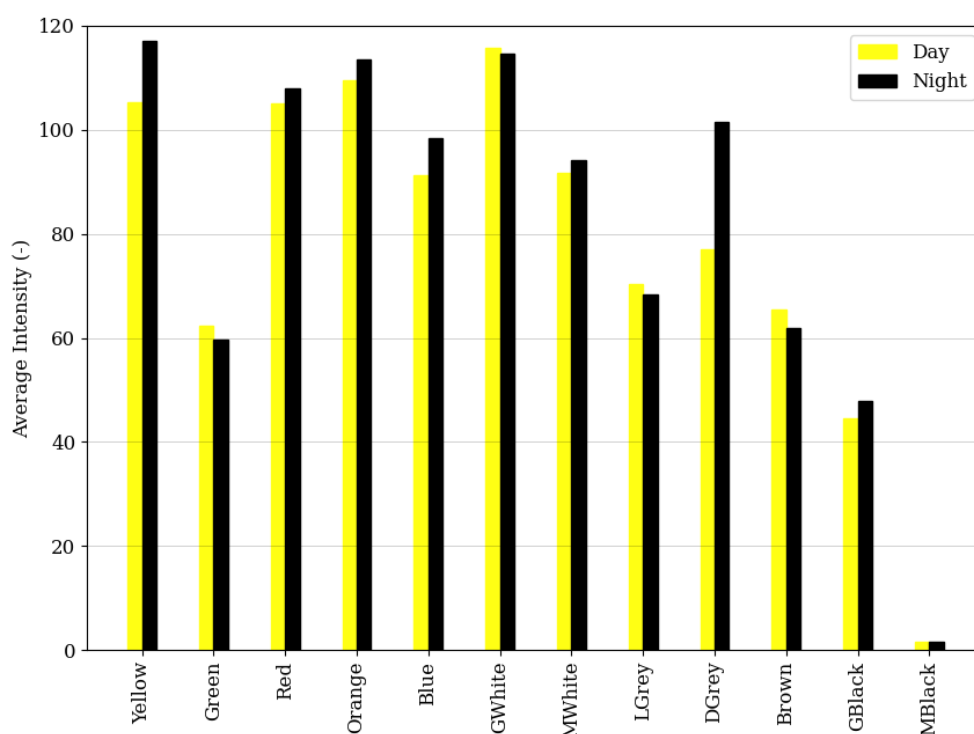
Figure 4.14: Average intensity for smooth targets at 4m and 0° in different ambient lighting

4.3   CONCRETE TARGETS

Since roughness and wetness are important known disruptive factors, their influence on laser beam return signals were investigated with regards to concrete surfaces.

4.3.1   Range estimates

Despite the difference in roughness and state of saturation of each target, SD of range measurements for all test distances were below 15 mm. Results of 0° scans are shown in Figure 4.15 and 4.16. No significant increase in deviation was observed for larger distances as was reported by Voegtle and Wakaluk (2009). The tested distances were however all less than 6 m.
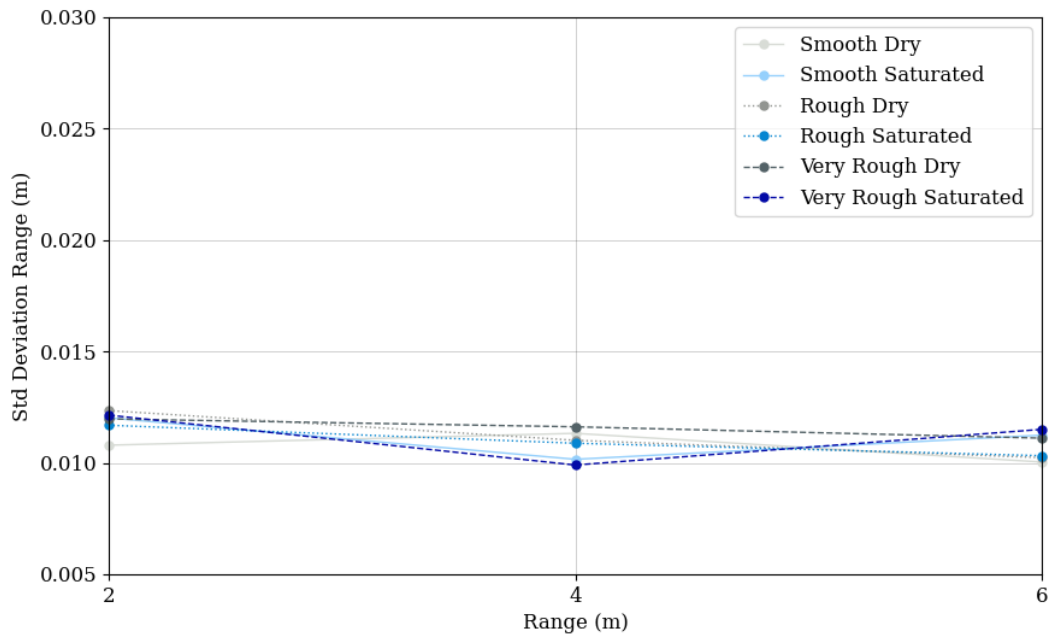
Figure 4.15: Standard deviation of range for Dolomite concrete targets at 0°
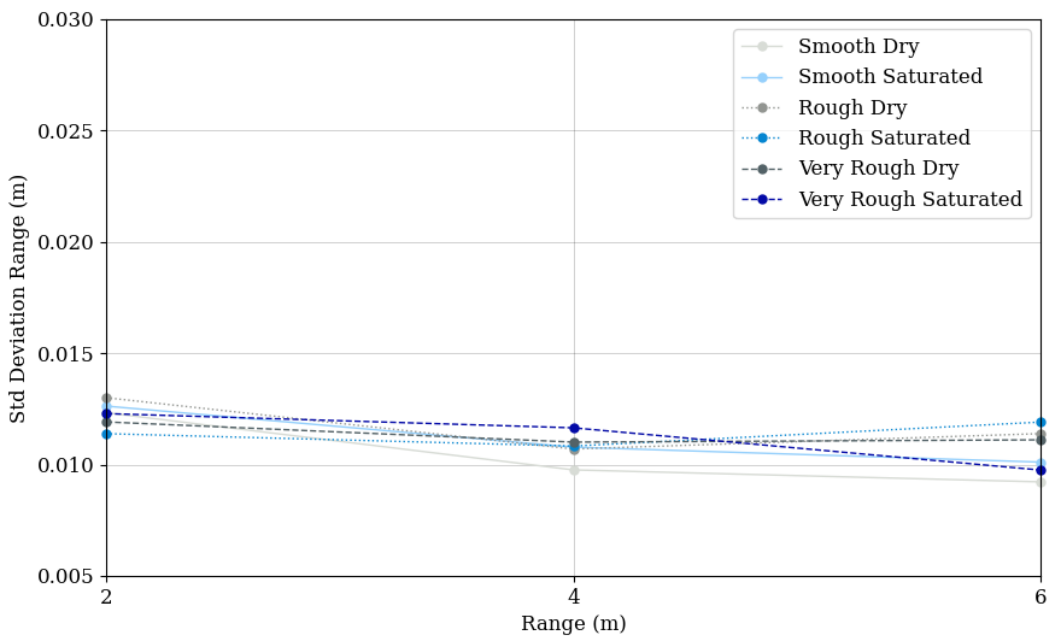
Figure 4.16: Standard deviation of range for Granite concrete targets at 0°

Longer distances need to be tested in future to observe if a decrease in SD of range does occur, but for the purpose of the study a max distance of 6 m was sufficient. The different concrete

types, roughness and degree of saturation had minimal effect on the SD of range measurements which followed a similar trend to all colour targets.

The same high variability in range estimates measured for black coloured targets was not observed for the concrete targets, even in their saturated state. The point density of the dolomite concrete targets is shown in Figure 4.17. This shows that roughness and degree of saturation had no significant effect and that all targets followed the same exponential decrease in point density as observed for the colour targets. Targets scanned at 0° incidence angle, where high deviations in intensity were observed, proved to have an insignificant effect on the range measurements.
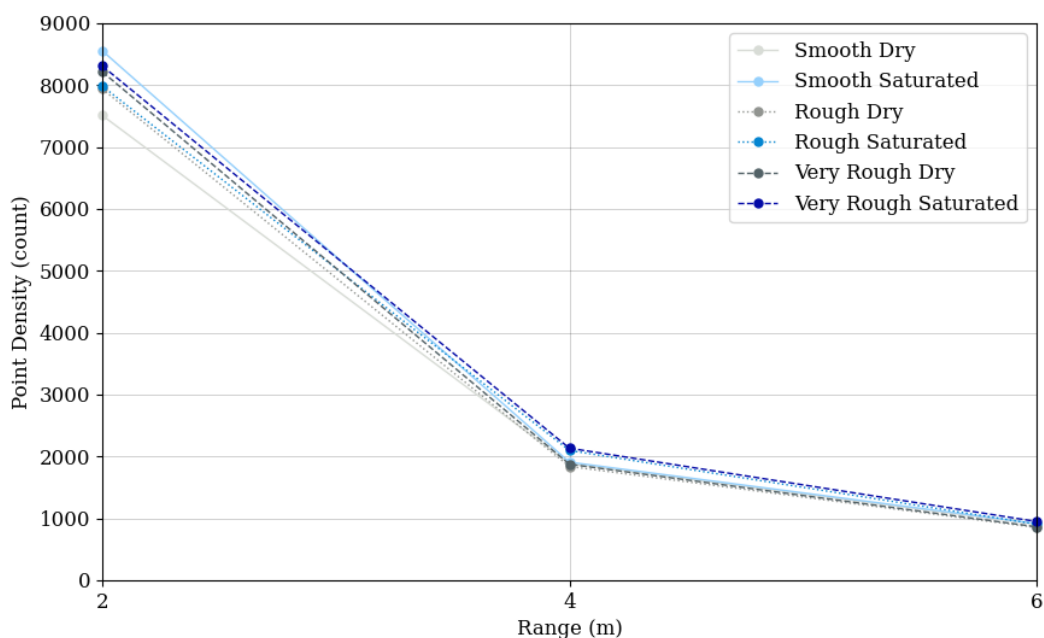
Figure 4.17: Point density of Dolomite concrete targets scanned at different distances

4.3.2 Intensity

The difference in average intensity between concrete targets of different roughness and wetness are shown in Figure 4.18 for scans conducted at 4 m and 15°. The tests confirmed that an increase in saturation lead to a significant decrease in recorded intensity values as water absorbed more of the laser's incident energy. Suchocki and Katzer (2018) observed a similar result when scanning concrete targets with a LiDAR of wavelength 1550 nm and reported an average decrease of 20 % for intensity values between the different states of saturation.

While all targets in their dry state had a mean intensity greater than 27, once saturated these intensity values were less than or equal to 11. The dolomite targets all recorded lower intensity readings compared to the granite targets. This is due to the dolomite stone being darker in colour compared to granite sand. Although an increase in roughness resulted in a decrease in intensity for the dry state, measurements did not differ significantly for targets in their saturated state.
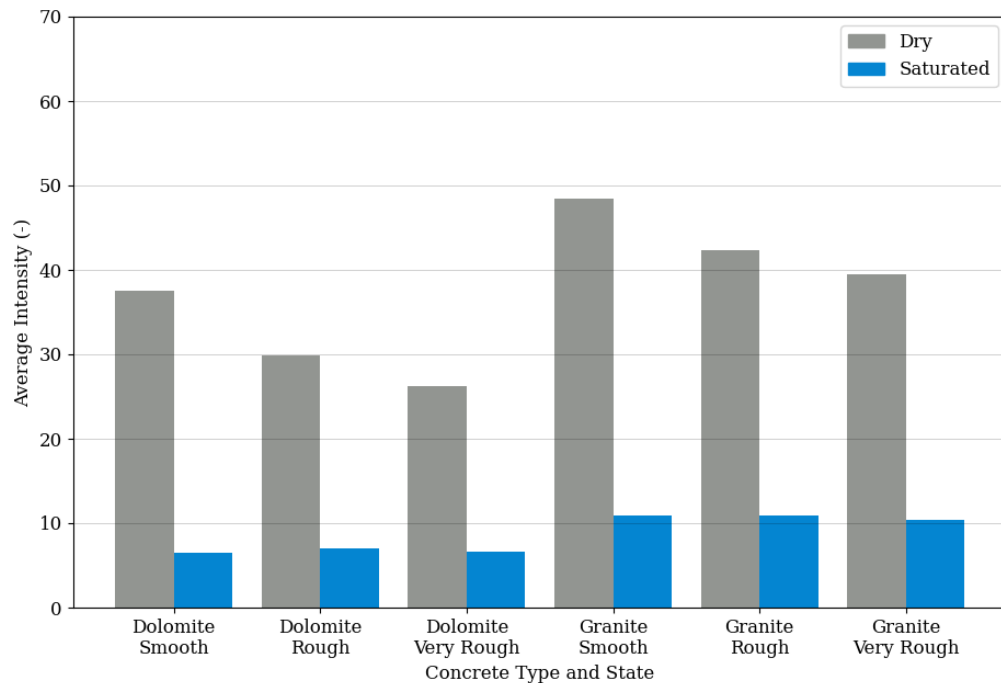
Figure 4.18: Different states of saturation of concrete targets at 4m and 15°

A complete set of the above results, including point density (n), intensity and range information for all distances at 15° are presented and summarised in Table 4.2. The average intensity values of both the dry and saturated targets scanned at 2 m were higher than when the same targets were scanned at distances of 4 and 6 m. This increase in average intensity values may be due to a type of near distance effect as illuded to in Section 4.2. Apart from the high intensity reading for the dry smooth dolomite targets scanned at 6 m, intensity readings for the 4 and 6 m distances showed minimal differences when compared. Similar results were observed for all distances and incidence angles except those taken orthogonally or at a 0° incidence angle.

Table 4.2: Summary of concrete targets in different states of saturation and roughness

Distance [m]		n	Intensity (-)		Range (m)		n	Intensity (-)		Range (m)	
			Avg	Std	Avg	Std		Avg	Std	Avg	Std
		Fully Saturated (Sat)					**Saturated by air humidity (Dry)**				
						Dolomite					
2m	Smooth	8231	10.3	2.426	1.937	0.0116	7638	48.7	2.828	1.926	0.0132
	Rough	8461	12.5	3.654	1.933	0.0091	7573	42.9	3.366	1.926	0.0146
	Very Rough	8847	10.3	3.828	1.933	0.0080	7475	37.5	5.898	1.930	0.0105
4m	Smooth	1847	6.5	1.777	3.929	0.0101	1860	37.5	5.691	3.925	0.0120
	Rough	2045	7.1	1.820	3.927	0.0114	1801	29.8	3.226	3.924	0.0163
	Very Rough	2075	6.6	2.068	3.927	0.0106	1741	26.2	4.555	3.925	0.0142
6m	Smooth	872	6.5	1.410	5.928	0.0116	740	52.5	6.319	5.925	0.0141
	Rough	865	7.1	1.713	5.928	0.0125	756	36.5	5.400	5.922	0.0140
	Very Rough	884	6.3	2.127	5.927	0.0125	757	29.2	5.929	5.918	0.0152
						Granite					
2m	Smooth	8292	17.5	2.585	1.933	0.0137	7866	58.50	4.138	1.925	0.0111
	Rough	8262	17.7	3.399	1.931	0.0120	8181	53.00	4.104	1.930	0.0135
	Very Rough	8026	15.5	3.345	1.933	0.0113	7639	52.00	4.910	1.926	0.0094
4m	Smooth	1882	11.0	2.519	3.931	0.0129	1991	48.4	6.876	3.928	0.0114
	Rough	2006	10.9	2.371	3.928	0.0154	1699	42.4	6.434	3.922	0.0116
	Very Rough	2094	10.4	2.297	3.932	0.0142	1884	39.5	6.812	3.928	0.0141
6m	Smooth	958	11.6	2.011	5.930	0.0155	824	49.6	5.383	5.935	0.0144
	Rough	881	11.4	2.718	5.933	0.0169	815	46.5	7.906	5.922	0.0155
	Very Rough	862	10.3	2.379	5.931	0.0174	818	41.8	5.212	5.934	0.0143

Each concrete surface is characterised as being rough and exhibits diffusive reflectance. This diffuse reflection is however, progressively replaced by specular reflection due to the effect of water (Tan et al., 2018). The change in mean intensity with increasing incidence angle is shown in Figure 4.19. Relating back to the results of the smooth coloured targets, specifically the semi-gloss ones, a similar pattern emerges where a spike in intensity readings is recorded for orthogonal scans. This spike in recorded intensity at 0° is as a result of specular reflection. When a rough surface undergoes saturation, small air gaps and pores are filled with water. This eventually creates a very thin layer that covers the surface of the material. Unlike scanners in the green light wavelength that can penetrate water, the scanner used had a wavelength in the IR band. Laser beams of this wavelength are unable to penetrate water and result in similar specular reflections as observed for mirror like targets (Pesci and Teza, 2008; Tan et al., 2018). The targets in their dry state do not suffer from this deviation at 0° and follow the same decreasing intensity trend as observed for the rough coloured targets.
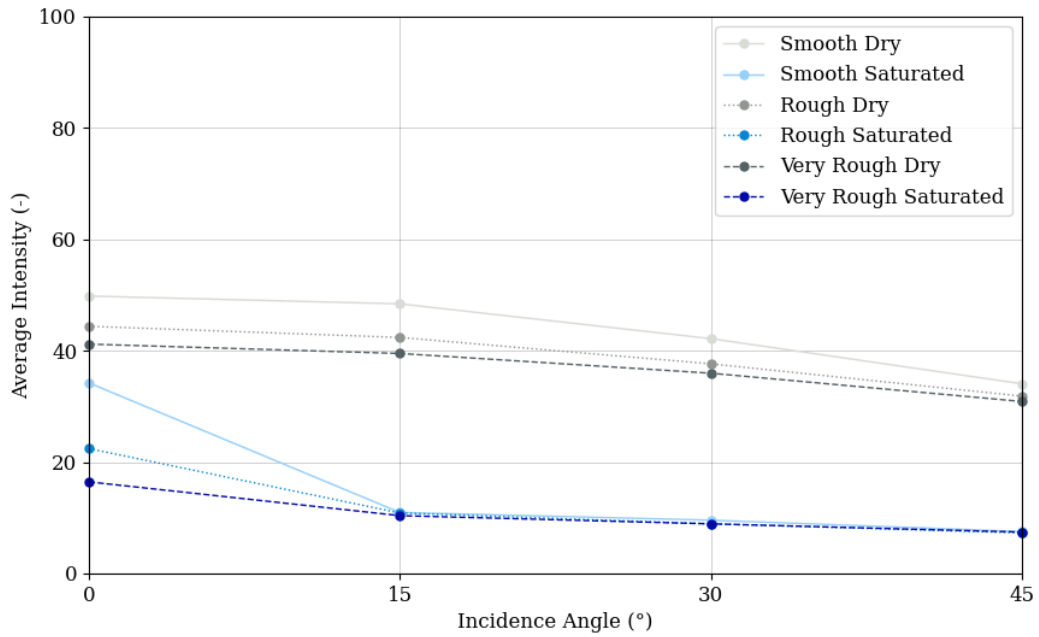
Figure 4.19: Average intensity of granite target at 4m

Figure 4.20 further highlights the spike in intensity readings of saturated targets at 0° by plotting the SD of intensity readings. Scans at all distances for both types of concrete showed to have the same high deviation at 0°. This high standard deviation can be eliminated by observing the same target at an angle greater than or equal to 15° as observed in Figure 4.20.
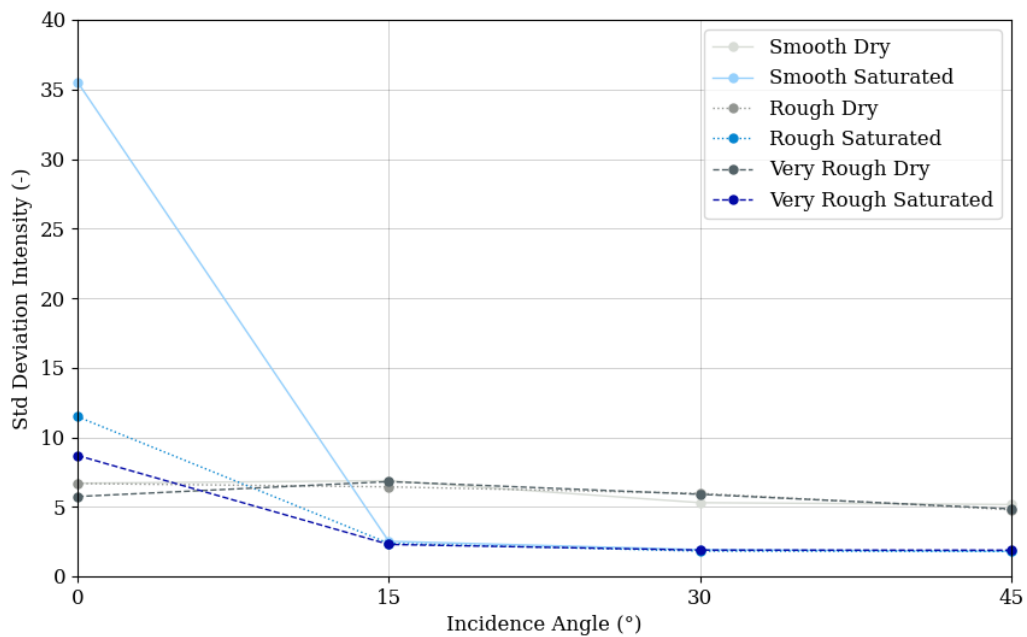
Figure 4.20: Standard deviation of intensity of granite target at 4m

The role of specular reflection on smooth wet surfaces at normal incidence (0°) should be investigated further in future. All incidence angles above 15° showed similar range estimates and average intensity readings.

Ambient lighting

The influence of ambient lighting was observed for the concrete targets. Figures 4.21 and 4.22 show the results for all concrete types scanned at 4m and 15°. Conclusions similar to those of the coloured targets were reached. Minimal differences when comparing scans of identical targets taken in different lighting conditions confirmed that lighting had little to no influence on the intensity measurements. Larger variations (5 to 8 units) were observed for concrete targets in their dry state compared to the saturated state were variations of less than 1 unit were measured. No trends or definite differences were noted.
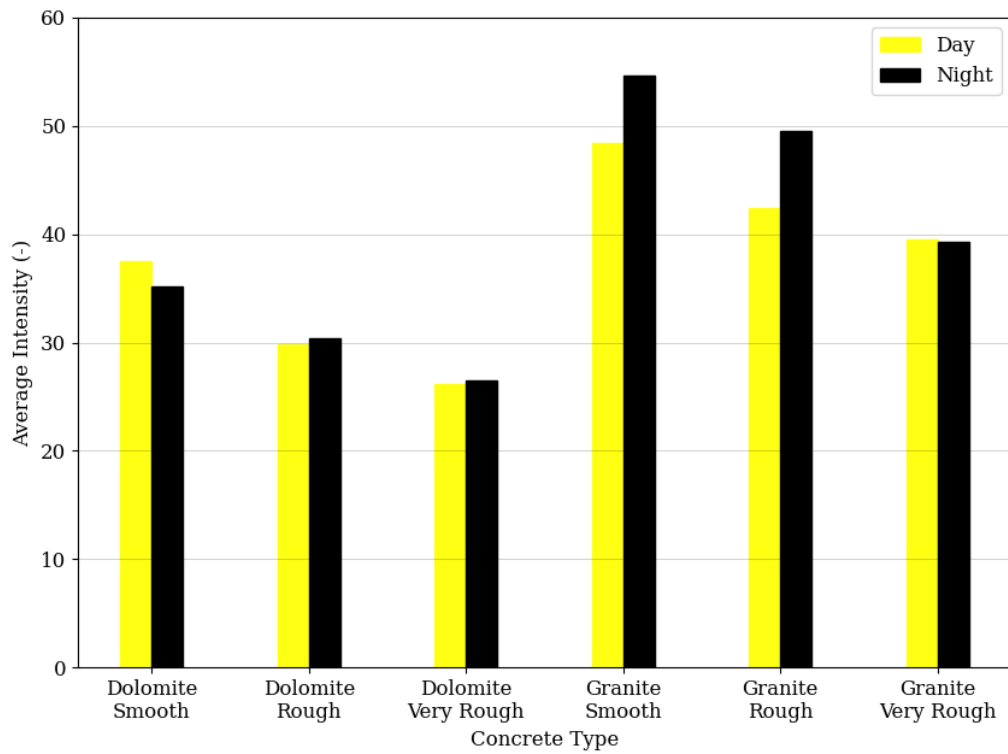
Figure 4.21: Average intensity for dry concrete targets in different ambient lighting at 4m and 15°
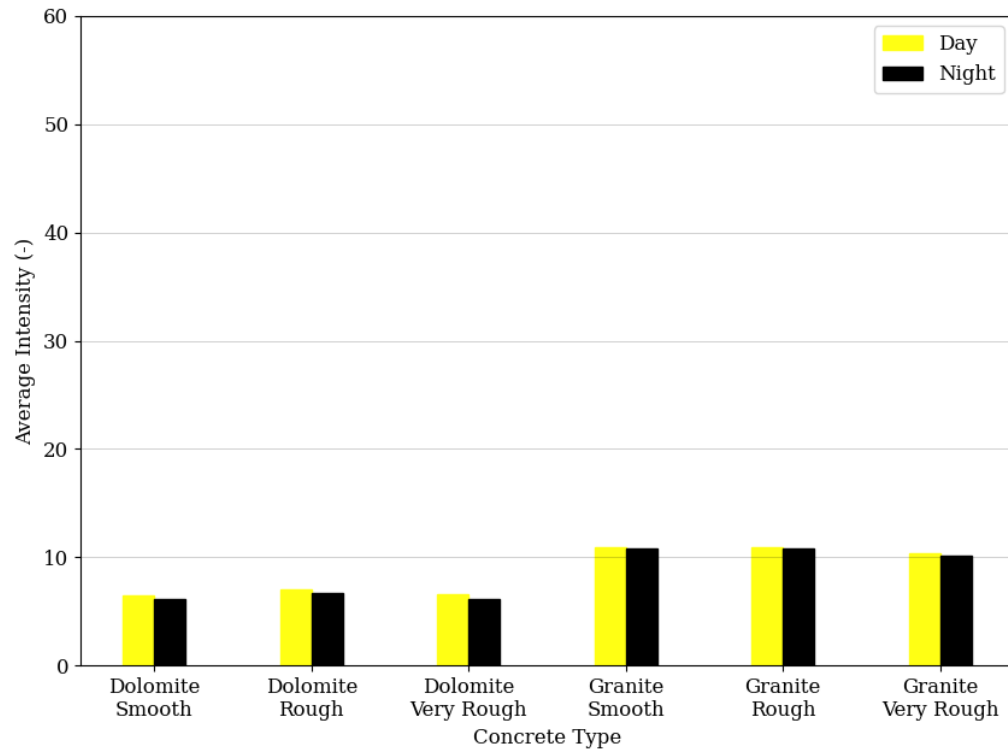
Figure 4.22: Average intensity for saturated concrete targets in different ambient lighting at 4m and 15°

4.4 TUNNEL SCANS

The point clouds captured for the two different tunnel sections, constructed using different techniques, are presented below. These two tunnel sections are very different in their appearance, structure and number of water leakage issues present on the walls.

4.4.1 3D point cloud of tunnel sections

Segmented point clouds of the two different scanned tunnels sections are shown in Figure 4.23. The DB section (green) showed a larger number of leakage areas, highlighted in red, compared to the TBM section (blue) which showed no signs of water leaks at all.

(a)

(b)
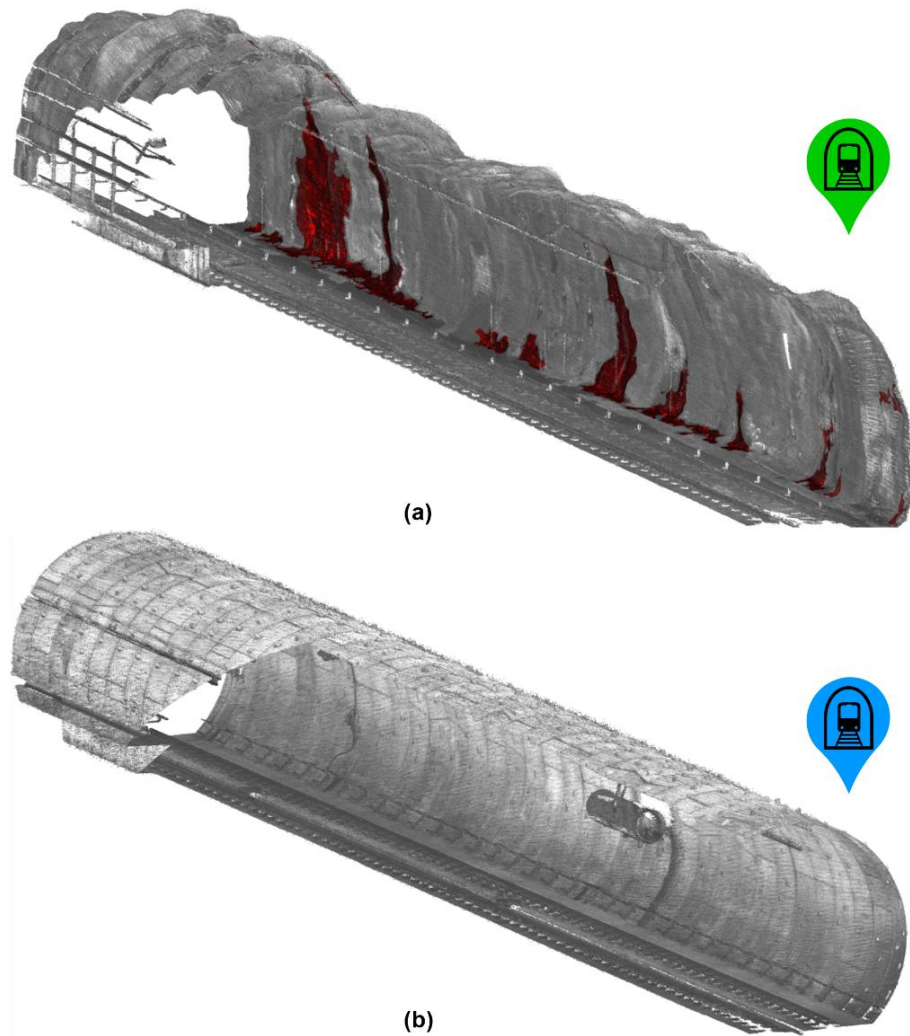
Figure 4.23: Sliced 3D point clouds of two 50 m tunnel sections: (a) DB, and (b) TBM

4.4.2　Water leakage areas

Areas of water leakage were only identified in the DB tunnel section. A selected 50 m segment from chainage 446 to 396 m was selected to present as this section displayed the largest number of leakages. Figure 4.24 shows the location of these leakage areas in a planar section view. An axis from 0 to 50 m at the base of the Figure shows the approximate location of each leak in the section. A quantitative summary of the leakages is tabulated in Table 4.3.
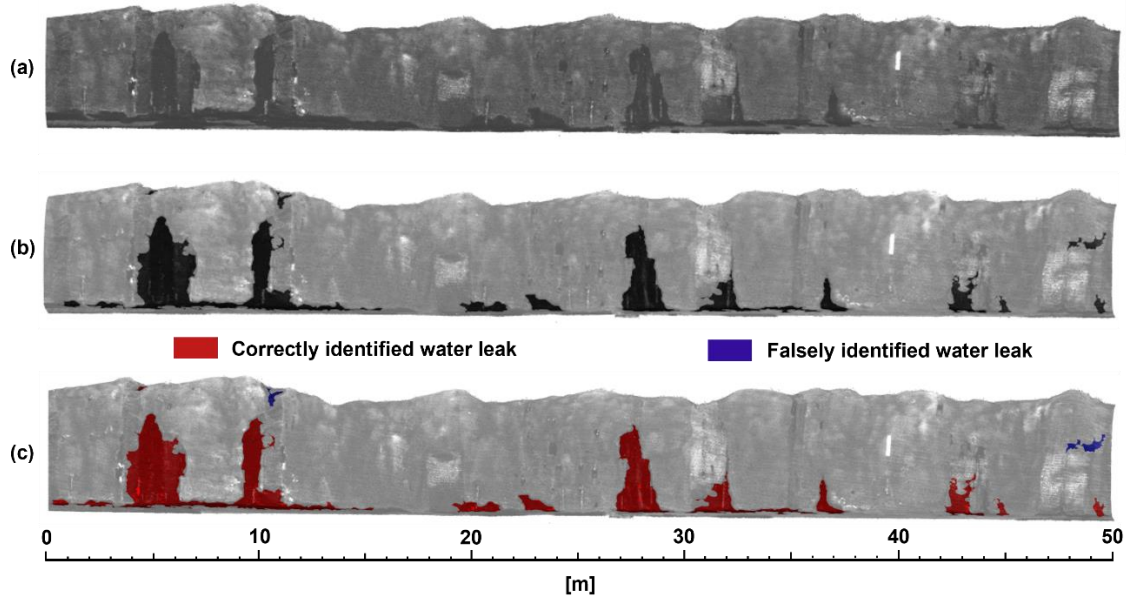
Figure 4.24: Conversion from raw point cloud to leakage area extraction: (a) raw 3D point cloud, (b) possible leaks identified, and (c) filtered final leakages

Table 4.3: Summary of the water leakages in the 50 m DB tunnel section

Leakage Number	Location [m]		Area [m^2]	Point Density
	Start	Stop		
#1	1.71	2.60	0.38	112
#2	5.42	6.00	0.15	102
#3	2.84	15.29	18.17	7871
#4	19.83	22.07	0.86	360
#5	22.84	24.71	0.79	393
#6	27.26	29.93	5.72	2657
#7	30.30	36.42	3.69	1811
#8	36.39	37.90	1.08	579
#9	42.21	44.02	1.84	736
#10	44.33	45.09	0.32	92
#11	48.87	49.59	0.32	104

These results demonstrate the ability to obtain quantitative information of water leakage areas in underground tunnels using intensity information from point cloud data. Although the method did incorrectly predict two small areas, as seen by the surfaces highlight in blue in Figure 4.24 (c), it did locate and map all other leakages in the section. Figure 4.25 shows the raw point cloud of the 50 m tunnel section with direct comparisons of some extracted leakage areas and associated RGB images which were taken for visual validation purposes.
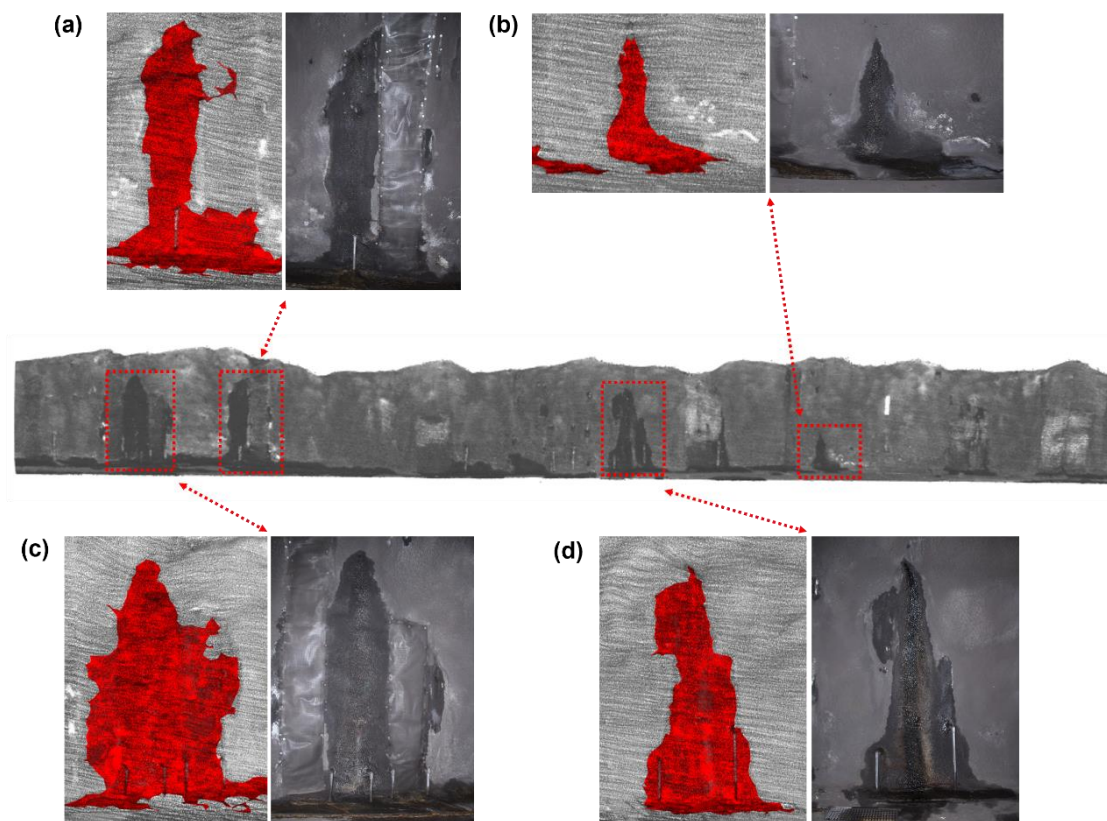
Figure 4.25: Comparison between extracted water leakage areas and RGB images of the red rectangular regions of interest

Water leaks in Figure 4.25 (a and c) were located where previous remedial work had been carried out. Although the leaks are not directly on the patch material but rather alongside each, parts of them were captured and recorded as a possible leakage area. This is specifically evident in Figure 4.25 (c). The additional leaks on the opposite sides of the patch suggested that the repair work was perhaps not as successful and additional patching needs to be carried out or a more detailed subsurface investigation considered. Leakages shown in Figure 4.25 (b and d) showed good agreement with the RGB images and seemed to match the leakage shape very well. Although the extracted leakage areas are not extracted with millimeter accuracy, the speed at which these inspections can be carried out is extremely advantageous while still capturing locations of the leaks and closely estimated leakage areas. The ability to conduct inspections remotely while capturing and generating a virtual copy of the infrastructure asset is an additional benefit.

Water leakage information of the tunnel section from Park to Rosebank station (green), gathered from a visual assessment, notes the section as suffering from continuous water leakages. The method in which these leakages are recorded in the visual assessment is very

simplistic. The start and end points where continuous leakages are observed is recorded and a note is added. A visual assessment conducted on the 21st June 2021 stated chainage 860 m to E1 was experiencing water leakage and the notes were that the water running from the leaks was continuous. For a section of almost a kilometre in length (860 m to E1/ 0 m), simply stating 'continuous water leaks' does not provide maintenance managers and engineers with any quantitative information from which to base their decisions.

A total of six 50 m sections in this chainage range were scanned and demonstrated the ability to extract quantitative information of the observed water leakage areas. The 50 m section, in the work presented above, is for the section from chainage 446 to 396 m. This section was chosen to present as it recorded the highest number of leakage areas.

4.4.3 Summary

Figure 4.26 summarises the entire process, moving from the point cloud in its raw form through extraction, filtration, complex surface generation and finally applying tolerances to the possible identified leakage areas. Quantitative information can then be gathered for specific water leakage areas by evaluating and querying the information of each.
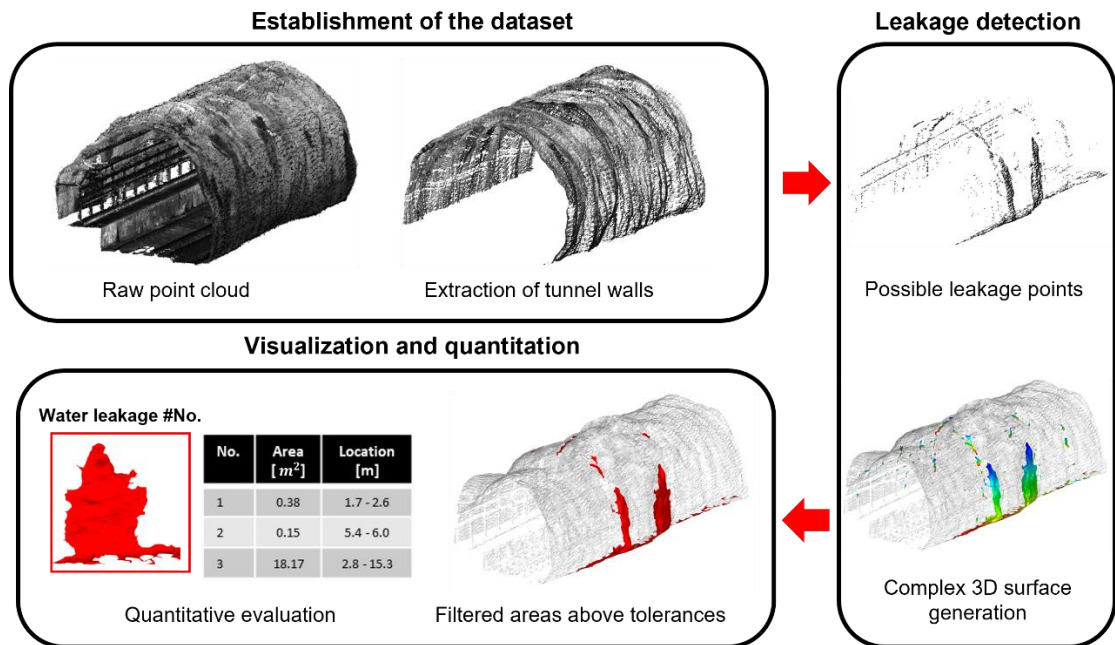
Figure 4.26: Schematic of proposed workflow for water leakage area extraction

A timeline of the entire process, documented from the initial start-up of the Hovermap right up until the final end result, is given in Figure 4.27. The end result provides a full digital 3D point cloud of the tunnel section with water leakage areas identified and mapped out with quantitative information pertaining to the location and size of each leakage area.

EQUIPMENT SETUP
Remove Hovermap from box, connect battery and turn on

TRANSFER FILE
The captured scan is transferred off the Hovermap onto a USB for further processing

MAPTEK WORKFLOW
Import the .laz file into Maptek and run the automated workflow and python scripts

END RESULT
Digital 3D point cloud of the tunnel section with water leakage areas identified and mapped

01:00   03:30   04:00   13:00   23:00   28:00   30:00 minutes

SCAN TUNNEL SECTION
Scan a 50 m tunnel section at a walking speed of ~0.5 m/s

EMESENT SOFTWARE
Generate a .laz point cloud file of the scanned section in Emesent in house software

EXTRACT LEAKAGE AREAS
Query all leakage areas and compare these with RGB images

Figure 4.27: Timeline of water leakage extraction process

The ability for leakage areas to be extracted from point clouds where data capture has the potential of being fully autonomous, removing the need for personnel to enter the tunnel, make this an attractive alternative to the current method. The workflow and method presented show potential for quick, cost-effective and widespread water leakage mapping with the capability of shorter revisit times. Scans can be conducted before and after remedial works to judge the effectiveness of the patch or at different seasons in the year to correlate this with rainfall events.

4.4.4 3D tunnel model (Twinning)

Just like photogrammetry which suffers from poor lighting, the same existed for the colourised scan, as video footage captured from the Go-Pro mounted at the base of the Hovermap is used to colourise the points. Figure 4.28 shows how colourisation and complex surface generation can yield a more complete digital twin of the infrastructure asset. As can be seen, colourised points are only visible where additional lighting in the tunnel was present. The poor coverage area is as a result of the reduced field of view of the Go-Pro and hence less points were colourised. Most of the points are coloured black as was the image captured by the video. More care and time should be spent on the areas were little or no points were observed.
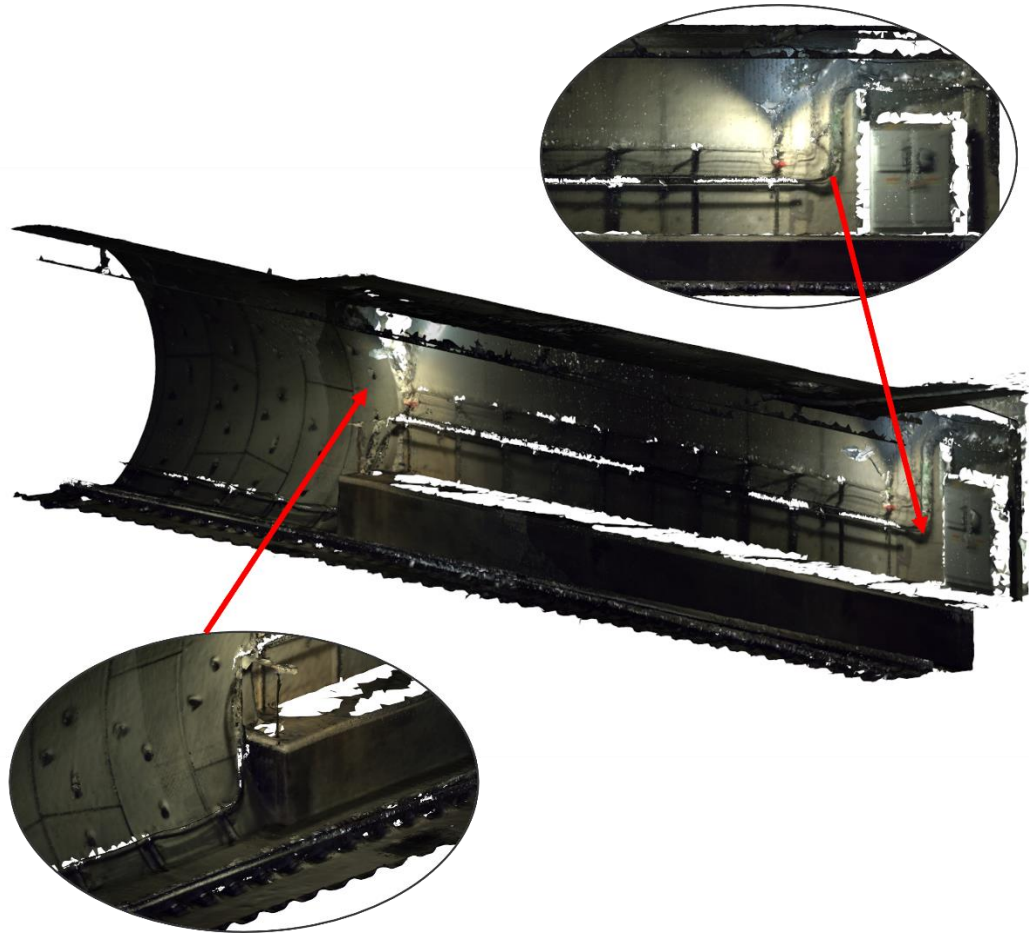
Figure 4.28: Close up of the colourization when additional lighting is provided

4.5   DISCUSSION

Although LiDAR surveying does not provide a panacea for solving the underlying problems of water leakage, it does provide a 3D virtual map of the scanned environment. With the applied workflow and intensity information captured from point clouds, the location and area of each leak is detectable. Such information is of great benefit to engineers and maintenance managers as it allows them to observe the tunnel's current condition remotely and better plan remedial work in a systematic and rational manner. It reduces the need for personnel to enter tunnels for initial visual assessments and is an effective means of collecting the necessary data for offsite measurements and analysis. The speed at which surveys can be carried out with complete point clouds ready in a matter of minutes, provides a powerful tool for tunnel maintenance managers to exploit.

5 CONCLUSIONS AND RECOMMENDATIONS

This Chapter summarises the findings of the experimental work performed and relates back to the study objectives outlined in Chapter 1. Recommendations for future work and research are also provided.

5.1 CONCLUSIONS

The conclusions made with regard to this study are summarised in this section.

5.1.1 Coloured targets

The following conclusions are made regarding the tested colour targets and the effect colour and surface roughness has on the backscattered energy:

- High precision measurements should be carried out preferably on brighter diffuse coloured surfaces without specular reflection characteristics.
- Semi-gloss black shows extremely unstable range measurement estimates at all distances and incidence angles, but particularly for close range scans. The conclusion for the erroneous readings was due to a high specular reflection component which resulted a sharp decrease in point density.
- Rough coloured targets showed steadier intensity readings for different incidence angles as opposed to smooth targets which recorded spikes for targets scanned at 0°.
- Dark colours recorded the lowest intensities and were the most stable with increasing distance and incidence angle.
- Ambient lighting showed to have little influence on range estimates and intensity readings, with an average SD of 2.1 mm and 3 units respectively for scans conducted under different lighting conditions.

5.1.2 Concrete targets

Due to the multiplicity of common building materials, only concrete surfaces were reviewed. Different degrees of roughness and states of saturation of the concrete targets were of specific interest. The following conclusions are made in this regard:

- The SD of range measurements for all concrete targets at different distances and states of saturation was between 10 and 18 mm, which is below the published 30 mm accuracy of the Hovermap system.

- The dolomite targets all showed a lower average intensity compared to the granite targets of similar roughness. This was due to the difference in colour of the aggregate.

- Saturation of the targets resulted in a definite decrease in the recorded intensity values. The average intensity value reduced between 70 and 80 % for each target when comparing the dry and saturated states.

- Specular reflections, where an increase in intensity was recorded, were prevalent for the saturated targets scanned at 0° for all roughness's. This was due to the high backscatter energy and highlight phenomenon effect.

- The point cloud intensity of the different concrete targets was not significantly influenced by ambient lighting conditions. Dry and saturated targets recorded max differences of 8 and 1 intensity units respectively for different lighting conditions.

5.1.3 Tunnel scans

Conclusions of the laboratory test results provided additional insight into the effect/implications of colour, roughness, saturation and illumination. The following conclusions were of importance for tunnel investigations:

- All surfaces are dark in the tunnel and give lower intensity readings. Rough coloured targets showed less variability and eliminated the highlight phenomenon that was observed for smooth targets.
- An increase in target roughness of a showed to decrease the recorded intensity.
- Intensity readings of saturated targets showed minimal variation across the different degrees of roughness, but did show a slight difference between dolomite and granite stone. Saturated targets recorded higher intensities at 0° but with intensity and proximity filtering this was eliminated.
- Minimal external lighting was present in the tunnels. Saturated rough concrete targets showed minimal difference when scanned in different ambient lighting conditions, as did the dark rough coloured targets.

The following conclusions were made with regard to the capability of extracting water leakage areas in underground tunnels using point cloud intensity data alone:

- The methodology and incorporated workflow proved capable of extracting water leakages in underground tunnels in a fast and efficient way.
- The extracted 3D surface leakages showed good visual agreement with the RGB images taken of the physical water leaks in the section.

- Erroneous leakage detection on some patches of previous repaired leaks was noted.
- Quantitative information of each leak location and surface area was collected and tabulated.

Besides the methods inability to extract leakage outlines with millimetre accuracy, it does provide a quick and efficient means of obtaining quantitative water leakage information. This all whilst still collecting a digital 3D point cloud twin of the section for additional calculations.

5.2   RECOMMENDATIONS

The following were identified as recommendations for further research into the topic:

- An in-depth 3D scan measurement distribution of the Hovermap LiDAR system should be analysed, similar to work done by Morales et al. (2018).

- Further investigate the near distance effects of the Hovermap LiDAR and saturation like effect at intensity values of 100 for the 2 m distance scans.

- Use a line scanner with nanometre accuracy to better measure the difference in surface roughness. This will aid in characterising and comparing surfaces of the same roughness more accurately and account for laser specific scanning errors.

- Investigate false detection of leakages on the patch repairs and incorporate additional computer vision and deep learning techniques to correct for such, without significantly increasing processing time.

- Test the workflow for a longer tunnel section and automate the reporting of leakage areas, linking the same leakage areas of previous scans together and providing a direct comparison between scans conducted at different epochs.

- Attempt using external lighting to illuminate the tunnel and capture a full colourised point cloud. Successive non-colourised point clouds can then be captured and water leakages extracted. These extracted leakage areas can then be overlain on the colourised point cloud to provide a more complete digital representation of the tunnels current condition. This would aid maintenance managers and nontechnical persons gain a better visual representation of the current leakage areas in the tunnel.

- Repeat scans at different epochs to compare leakage areas (Summer vs. Winter) and check for signs of deformation by subtracting two scans from one another.

6   REFERENCES

Allen, C., Averso, M., Hargraves, C. and McNeil, S. (2015). Guide for the Preservation of Highway Tunnel Systems. *Transportation Research Board*, Project No. NCHRP 14-27.

Ångström, A. (1925). The albedo of various surfaces of ground. *Geografiska Annaler*, *7*(4), pp.323-342.

Arastounia, M. (2012). Automatic classification of lidar point clouds in a railway environment. University of Twente, Master's thesis. *Retrieved from the internet: URL: http://essay.utwente.nl/84784/1/arastounia.pdf. Date:4 January 2021*

Arastounia, M. (2016). Automated as-built model generation of subway tunnels from mobile LiDAR data. *Sensors*, *16*(9), 1486.

Ariyachandra, M.R.M.F. and Brilakis, I. (2019). Understanding the Challenge of Digitally Twinning the Geometry of Existing Rail Infrastructure. *Proceedings of the 12th FARU International Research Conference, Colombo, Sri Lanka (Faculty of Architecture Research Unit), December*, pp.25-32.

Ariyachandra, M.R.M.F. and Brilakis, I. (2020). Digital Twinning of Railway Overhead Line Equipment from Airborne LiDAR Data. *Proceedings of the 37th International Symposium on Automation and Robotics in Construction (ISARC),* pp.1270-1277.

Attard, L., Debono, C.J., Valentino, G. and Di Castro, M. (2018). Tunnel inspection using photogrammetric techniques and image processing: A review. *ISPRS Journal of Photogrammetry and Remote Sensing*, *144*, pp.180-188.

Azman, B., Bull, G. and Amirah, N. (2015). A brief History of LiDAR. *Earth Science*.

Baltsavias, E.P. (1999). Airborne laser scanning: basic relations and formulas. *ISPRS Journal of Photogrammetry and Remote Sensing, 54(2-3),* pp.199-214.

Baylis, C.N.C., Kewe, D.R. and Jones, E.W. (2020). Mobile drone LiDAR structural data collection and analysis. In *Proceedings of the Second International Conference on Underground Mining Technology,* Australian Centre for Geomechanics, pp. 325-334.

Blaskow, R. and Schneider, D. (2014). Analysis and correction of the dependency between laser scanner intensity values and range. *The International Archives of Photogrammetry, Remote Sensing and Spatial Information Sciences*, *40*(5), p.107.

Bolkas, D. (2019) Terrestrial laser scanner intensity correction for the incidence angle effect on surfaces with different colours and sheens. *International Journal of Remote Sensing, 40(18),* pp.7169-7189.

Bolkas, D. and Martinez, A. (2017). Effect of target color and scanning geometry on terrestrial LiDAR point-cloud noise and plane fitting. *Journal of Applied Geodesy*, *12*(1), pp.109-127.

Bula, J., Derron, M.H. and Mariethoz, G. (2020). Dense point cloud acquisition with a low-cost Velodyne VLP-16. *Geoscientific Instrumentation, Methods and Data Systems*, *9*(2), pp.385-396.

CETU (Centre d'Études des Tunnels) (2015). Road tunnel civil engineering inspection guide, Book:1 from disorder to analysis, from analysis to rating. *Retrieved from the Internet: URL:http://www.cetu.developpement-durable.gouv.fr/IMG/pdf/guide_inspection-book1_hv.pdf. Date:16 February 2021*

Chen, S.E., Liu, W., Bian, H. and Smith, B. (2013). 3D LiDAR scans for bridge damage evaluations. Published in *Forensic Engineering 2012: Gateway to a Safer Tomorrow,* pp.487-495.

CRAIC (2021). UV-visible-NIR, fluorescence, photoluminescence & raman microspectrophotometers. CRAIC Technologies. *Retrieved from the internet: URL:* http://www.microspectra.com/. *Date:14 August 2021*

Dawood, T., Zhu, Z. and Zayed, T. (2020). Deterioration mapping in subway infrastructure using sensory data of GPR. *Tunnelling and Underground Space Technology*, *103*, p.103487.

El Masri, Y. and Rakha, T. (2020). A scoping review of non-destructive testing (NDT) techniques in building performance diagnostic inspections. *Construction and Building Materials*, *265*, p.120542.

Emesent (2020). Hovermap HF1 Specification. Milton, Queensland, 4064, Australia. *Retrieved from the Internet: URL: https://www.emesent.io/hovermap/#mapping-specifications. Date: 8 Jan 2021.*

Evans, P. (2021). Improving convergence monitoring using lidar data at Rio Tinto's Argyle diamond mine. *Retrieved from the internet: URL: www.emesent.io. Date: 1 October 2021*

Filgueira, A., González-Jorge, H., Lagüela, S., Díaz-Vilariño, L. and Arias, P. (2017). Quantifying the influence of rain in LiDAR performance. *Measurement*, *95*, pp.143-148.

Flammini, F., Pragliola, C. and Smarra, G. (2016). Railway infrastructure monitoring by drones. *International Conference on Electrical Systems for Aircraft, Railway, Ship Propulsion and Road Vehicles & International Transportation Electrification Conference, November (ESARS-ITEC)*, pp. 1-6. IEEE.

Flohrer, C. (2010). Non-destructive testing methods for building diagnosis – state of the art and future trends. In *Non-Destructive Evaluation of Reinforced Concrete Structures*, pp. 14-29. Woodhead Publishing.

Frangopol, D.M. and Tsompanakis, Y. (2014). Maintenance and safety of aging infrastructure. *Structures and infrastructures book series* (10). CRC press.

Gastineau, A., Johnson, T. and Schultz, A. (2009). Bridge Health Monitoring and Inspections Systems–A Survey of Methods. Published by Minnesota Department of

Transportation. *Retrieved from the Internet: URL:* [*http://conservancy.umn.edu/*](http://conservancy.umn.edu/) [*bitstream/handle/11299/150962/Mn_DOT 2009-29. pdf*](http://conservancy.umn.edu/bitstream/handle/11299/150962/Mn_DOT 2009-29.pdf). *Date:8 January 2021*

Geng, Y., Wang, Z., Jia, L. and Qin, Y. (2020). Comparison of Lidar Point Cloud Features in Railway Environment. *IEEE International Conference on Computational Intelligence and Virtual Environments for Measurement Systems and Applications, June, (CIVEMSA)*, pp.1-6.

Glennie, C.L., Kusari, A. and Facchin, A. (2016). Calibration and stability analysis of the VLP-16 laser scanner. *ISPRS Annals of Photogrammetry, Remote Sensing & Spatial Information Sciences*, *9*.

Hanke, K., Grussenmeyer, P., Grimm-Pitzinger, A. and Weinold, T. (2006). First experiences with the Trimble GX scanner. In *ISPRS Comm. V Symposium*, *September, 36*, pp.1-6.

Hoult, N.A. and Soga, K. (2014). Sensing solutions for assessing and monitoring tunnels. In *Sensor technologies for Civil Infrastructures*, pp. 309-346. Woodhead Publishing.

Hu, Z.N., Xie, Y.L., Xu, G.P., Bin, S.L., Zhang, H.G., Lai, H.P., Liu, H.Z. and Yan, C.G. (2018). Segmental joint model tests of immersed tunnel on a settlement platform: A case study of the Hongkong-Zhuhai-Macao Bridge. *Tunnelling and Underground Space Technology*, *78*, pp.188-200.

Huang, H., Cheng, W., Zhou, M., Chen, J. and Zhao, S. (2020). Towards automated 3D inspection of water leakages in shield tunnel linings using mobile laser scanning data. *Sensors*, *20(22),* p.6669.

Huang, Z., Fu, H., Chen, W., Zhang, J. and Huang, H. (2018). Damage detection and quantitative analysis of shield tunnel structure. *Automation in Construction*, *94*, pp.303-316.

Janků, M., Cikrle, P., Grošek, J., Anton, O. and Stryk, J. (2019). Comparison of infrared thermography, ground-penetrating radar and ultrasonic pulse echo for detecting delaminations in concrete bridges. *Construction and Building Materials*, *225*, pp.1098-1111.

Javadnejad, F., Gillins, D.T., Parrish, C.E. and Slocum, R.K. (2019). A photogrammetric approach to fusing natural colour and thermal infrared UAS imagery in 3D point cloud generation. *International Journal of Remote Sensing*, *41*(1), pp.211-237.

Javadnejad, F. (2017). Small Unmanned Aircraft Systems (UAS) for Engineering Inspections and Geospatial Mapping. Oregon State University. *Retrieved from the Internet: URL:* [*http://ir.library.oregonstate.edu/concern/gradute_thesis_or_dissertations/6969z572s*](http://ir.library.oregonstate.edu/concern/gradute_thesis_or_dissertations/6969z572s). *Date:27 January 2021*

Jin, J., De Sloover, L., Verbeurgt, J., Stal, C., Deruyter, G., Montreuil, A.L., De Maeyer, P. and De Wulf, A. (2020). Measuring surface moisture on a sandy beach based on corrected intensity data of a mobile terrestrial lidar. *Remote Sensing*, *12*(2), p.209.

Jones, E.W. (2020). Mobile LiDAR for underground geomechanics: learnings from the teens and directions for the twenties. *Underground Mining Technology, 1982*, pp.3-26.

Jones, E.W., Sofonia, J., Canales, C., Hrabar, S. and Kendoul, F. (2020). Applications for the Hovermap autonomous drone system in underground mining operations. *Journal of the Southern African Institute of Mining and Metallurgy*, *120(1),* pp.49-56.

Kaasalainen, S., Jaakkola, A., Kaasalainen, M., Krooks, A. and Kukko, A. (2011). Analysis of incidence angle and distance effects on terrestrial laser scanner intensity: Search for correction methods. *Remote Sensing*, *3*(10), pp.2207-2221.

Kashani, A.G., Olsen, M.J., Parrish, C.E. and Wilson, N. (2015). A review of LiDAR radiometric processing: From ad hoc intensity correction to rigorous radiometric calibration. *Sensors, 15(11),* pp.28099-28128.

Kasireddy, V., Wei, Y. and Akinci, B. (2020). Use Cases for Owners and Maintainers. In *Infrastructure Computer Vision*, pp. 169-201. Butterworth-Heinemann.

Kersten, T., Mechelke, K., Lindstaedt, M. and Sternberg, H. (2008). Geometric accuracy investigations of the latest terrestrial laser scanning systems. In *FIG working week*, *June*, pp.14-19.

Kidd, J.R. (2017). Performance evaluation of the Velodyne VLP-16 system for surface feature surveying. University of New Hampshire, Durham, Master Thesis. *Retrieved from the Internet: URL: https://scholars.unh.edu/thesis/1116*. *Date:8 January 2021*

Kim, M.K., Sohn, H. and Chang, C.C. (2015). Localization and quantification of concrete spalling defects using terrestrial laser scanning. *Journal of Computing in Civil Engineering*, *29*(6), p.04014086.

Kim, M.K., Thedja, J.P.P. and Wang, Q. (2020). Automated dimensional quality assessment for formwork and rebar of reinforced concrete components using 3D point cloud data. *Automation in Construction*, *112*, p.103077.

Konishi, S., Kawakami, K. and Taguchi, M. (2016). Inspection method with infrared thermometry for detect void in subway tunnel lining. *Procedia Engineering*, *165*, pp.474-483.

Kukko, A., Kaasalainen, S. and Litkey, P. (2008). Effect of incidence angle on laser scanner intensity and surface data. *Applied Optics*, *47*(7), pp.986-992.

Kumar, S., Chattopadhyay, G., Reddy, V. and Kumar, U. (2006). Issues and Challenges with Logistics of Rail Maintenance. In *Proceedings of the Second International Intelligent Logistics Systems Conference*, pp. 16.1-16.10.

Labsphere (2021). Reflectance reference targets, standards and accessories. *Retrieved from the internet: URL:* https://www.labsphere.com/labsphere-products-solutions/materials-coatings-2/targets-standards/. *Date: 15 May 2021*

Lassiter, H.A., Whitley, T., Wilkinson, B. and Abd-Elrahman, A. (2020). Scan pattern characterization of Velodyne VLP-16 Lidar Sensor for UAS Laser Scanning. *Sensors*, *20*(24), p.7351.

Leingartner, M., Maurer, J., Ferrein, A. and Steinbauer, G. (2016). Evaluation of sensors and mapping approaches for disasters in tunnels. *Journal of Field Robotics*, *33*(8), pp.1037-1057.

Leslar, M., Perry, G. and McNease, K. (2010). Using mobile lidar to survey a railway line for asset inventory. In *Proceedings of the ASPRS 2010 Annual Conference, San Diego, CA, USA*, pp. 26-30.

Lidén, T. (2015). Railway infrastructure maintenance: A survey of planning problems and conducted research. *Transportation Research Procedia*, *10*, pp.574-583.

Lu, Z., Zhu, F., Shi, L., Wang, F., Zeng, P., Hu, J., Liu, X., Xu, Y. and Chen, Q. (2019). Automatic seepage detection in cable tunnels using infrared thermography. *Measurement Science and Technology*, *30*(11), p.115902.

Ma, L., Li, Y., Li, J., Wang, C., Wang, R. and Chapman, M.A. (2018). Mobile laser scanned point-clouds for road object detection and extraction: A review. *Remote Sensing*, *10*(10), p.1531.

Malacara, D. (2011). Color Vision and Colorimetry: Theory and Applications, *Second Edition,* SPIE Press, Bellingham, WA.

Maptek (2021). Maptek Workbench, version 2021.3. PointStudio, version 2021.1. Point cloud computer software. Adelaide, Australia. https://www.maptek.com/

Menendez, E., Victores, J.G., Montero, R., Martínez, S. and Balaguer, C. (2018). Tunnel structural inspection and assessment using an autonomous robotic system. *Automation in Construction*, *87*, pp.117-126.

Morales, J., Plaza-Leiva, V., Mandow, A., Gomez-Ruiz, J.A., Serón, J. and García-Cerezo, A. (2018). Analysis of 3D scan measurement distribution with application to a multi-beam lidar on a rotating platform. *Sensors*, *18*(2), p.395.

Mosalam, K.M., Takhirov, S.M. and Park, S. (2014). Applications of laser scanning to structures in laboratory tests and field surveys. *Structural Control and Health Monitoring*, *21*(1), pp.115-134.

Nakano, K., Tanaka, Y., Suzuki, H., Hayakawa, K. and Kurodai, M. (2020). On Practical Accuracy Aspects of Unmanned Aerial Vehicles Equipped with Survey Grade Laser Scanners. *The International Archives of Photogrammetry, Remote Sensing and Spatial Information Sciences, 43,* pp.343-348.

Neumann, T., Dülberg, E., Schiffer, S. and Ferrein, A. (2016). A rotating platform for swift acquisition of dense 3D point clouds. In *International Conference on Intelligent Robotics and Applications, August,* pp. 257-268.

OSHA (1999). Occupational Safety and Health Administration Technical Manual. *Government Institutes, 1(0). Retrieved from the internet: URL:* https://www.osha.gov/dts/osta/otm/. *Date: 1 March 2021*

Pandrol (2020). Ultrasonic Rail Testing. *Retrieved from the internet: URL:*https://www.pandrol.com/ product/ultrasonic-rail-testing/. *Date: 1 March 2021*

Péntek, Q., Allouis, T., Strauss, O. and Fiorio, C. (2018). Developing and validating a predictive model of measurement uncertainty for multi-beam lidars: Application to the Velodyne VLP-16. In *Proceedings of the Eighth International Conference on Image Processing Theory, Tools and Applications, November (IPTA)*, pp. 1-5. IEEE.

Pesci, A. and Teza, G. (2008). Effects of surface irregularities on intensity data from laser scanning: an experimental approach. *Annals of Geophysics, 51(5/6)*.

Pesci, A. and Teza, G. (2008). Terrestrial laser scanner and retro-reflective targets: an experiment for anomalous effects investigation. *International Journal of Remote Sensing, 29(19)*, pp.5749-5765.

Pfeifer, N., Höfle, B., Briese, C., Rutzinger, M. and Haring, A. (2008). Analysis of the backscattered energy in terrestrial laser scanning data. *International Archives of the Photogrammetry, Remote Sensing and Spatial Information Science*, *37*, pp.1045-1052.

Puente, I., Akinci, B., González-Jorge, H., Díaz-Vilariño, L. and Arias, P. (2016). A semi-automated method for extracting vertical clearance and cross sections in tunnels using mobile LiDAR data. *Tunnelling and Underground Space Technology*, *59*, pp.48-54.

Puente, I., González-Jorge, H., Martínez-Sánchez, J. and Arias, P. (2013). Review of mobile mapping and surveying technologies. *Measurement*, *46*(7), pp.2127-2145.

Puente, I., Núñez-Nieto, X., Prego, F.J. and Lorenzo, H. (2016). Non-Destructive Testing of Tunnels: Application of LiDAR and GPR Technologies. *Non-Destructive Techniques for the Evaluation of Structures and Infrastructure*, *11*, p.169-184.

Rees, W.G. (2013). Physical principles of remote sensing. *Cambridge University press (Third Edition), p.56-64*.

Ripley, B.D. (1977). Modelling spatial patterns. *Journal of the Royal Statistical Society: Series B (Methodological)*, *39*(2), pp.172-192.

Robeson, S.M., Li, A. and Huang, C. (2014). Point-pattern analysis on the sphere. *Spatial Statistics*, *10*, pp.76-86.

Sánchez-Rodríguez, A., Riveiro, B., Soilán, M. and González-deSantos, L.M. (2018). Automated detection and decomposition of railway tunnels from Mobile Laser Scanning Datasets. *Automation in Construction*, *96*, pp.171-179.

Sofonia, J.J. (2020a). Hovermap Accuracy Evaluation. Accuracy | Posts & Poles. *Retrieved from the internet: URL: www.emesent.io. Date: 16 January 2021*

Sofonia, J.J. (2020b). Georeferencing Hovermap point cloud using 'best-fit' sphere registration in CloudCompare. *Retrieved from the internet: URL: www.emesent.io. Date: 16 January 2021*

SparkFun (2021). SparkFun Triad Spectroscopy Sensor - AS7265x (Qwiic). *Retrieved from the internet: URL: https://www.sparkfun.com/products/15050. Date:14 August 2021*

Su, Z., Jamshidi, A., Núñez, A., Baldi, S. and De Schutter, B. (2019). Integrated condition-based track maintenance planning and crew scheduling of railway networks. *Transportation Research Part C: Emerging Technologies*, *105*, pp.359-384.

Suchocki, C. and Katzer, J. (2016). An example of harnessing Terrestrial Laser Scanner for remote sensing of saturation of chosen building materials. *Construction and Building Materials*, *122*, pp.400-405.

Suchocki, C. and Katzer, J. (2018). Terrestrial laser scanning harnessed for moisture detection in building materials - Problems and limitations. *Automation in Construction*, *94*, pp.127-134.

Suchocki, C., Damięcka-Suchocka, M., Katzer, J., Janicka, J., Rapiński, J. and Stałowska, P. (2020). Remote detection of moisture and bio-deterioration of building walls by time-of-flight and phase-shift terrestrial laser scanners. *Remote Sensing*, *12*(11), p.1708.

Suchocki, C., Katzer, J. and Panuś, A. (2017). Remote sensing to estimate saturation differences of chosen building materials using terrestrial laser scanner. *Reports on geodesy and geoinformatics*, *103*(1), pp.94-105.

Suchocki, C., Katzer, J. and Rapiński, J. (2018). Terrestrial laser scanner as a tool for assessment of saturation and moisture movement in building materials. *Periodica Polytechnica Civil Engineering*, *62*(3), pp.694-699.

Tan, K. and Cheng, X. (2016). Correction of incidence angle and distance effects on TLS intensity data based on reference targets. *Remote Sensing*, *8*(3), p.251.

Tan, K., Cheng, X., Ju, Q. and Wu, S. (2016). Correction of mobile TLS intensity data for water leakage spots detection in metro tunnels. *IEEE Geoscience and Remote Sensing Letters*, *13*(11), pp.1711-1715.

Tan, K., Zhang, W., Shen, F. and Cheng, X. (2018). Investigation of TLS intensity data and distance measurement errors from target specular reflections. *Remote Sensing*, *10*(7), p.1077.

Tatoglu, A. and Pochiraju, K. (2012). Point cloud segmentation with LIDAR reflection intensity behavior. *IEEE International Conference on Robotics and Automation*, pp.786-790.

Valença, J., Dias-da-Costa, D., Gonçalves, L., Júlio, E. and Araújo, H. (2014). Automatic concrete health monitoring: assessment and monitoring of concrete surfaces. *Structure and Infrastructure Engineering*, *10*(12), pp.1547-1554.

Valença, J., Puente, I., Júlio, E., González-Jorge, H. and Arias-Sánchez, P. (2017). Assessment of cracks on concrete bridges using image processing supported by laser scanning survey. *Construction and Building Materials*, *146*, pp.668-678.

Voegtle, T. and Wakaluk, S. (2009). Effects on the measurements of the terrestrial laser scanner HDS 6000 (Leica) caused by different object materials. *Proceedings of The International Society for Photogrammetry and Remote Sensing, ISPRS2009*, *38*, pp.68-74.

Voegtle, T., Schwab, I. and Landes, T. (2008). Influences of different materials on the measurements of a terrestrial laser scanner (TLS). In *Proceedings of the XXI Congress, The International Society for Photogrammetry and Remote Sensing, ISPRS2008*, *37*, pp.1061-1066.

Wang, C.K. and Lu, Y.Y. (2009). Potential of ILRIS3D intensity data for planar surfaces segmentation. *Sensors*, *9*(7), pp.5770-5782.

Wang, J.H. (2018). Lifecycle cost and performance analysis for repair of concrete tunnels. In *Eco-efficient repair and rehabilitation of concrete infrastructures*, 23, pp.637-672. Woodhead Publishing.

Wehr, A. (2008). LiDAR systems and calibration. *Topographic Laser Ranging and Scanning: Principles and Processing*, Chapter 4, pp.129-159.

Wulf, O. and Wagner, B. (2003). Fast 3D scanning methods for laser measurement systems. *International conference on control systems and computer science, July (CSCS14)*, pp. 2-5.

Xu, T., Xu, L., Li, X. and Yao, J. (2018). Detection of water leakage in underground tunnels using corrected intensity data and 3D point cloud of terrestrial laser scanning. *IEEE Access*, *6*, pp.32471-32480.

Xue, F., Lu, W., Chen, Z. and Webster, C.J. (2020). From LiDAR point cloud towards digital twin city: Clustering city objects based on Gestalt principles. *ISPRS Journal of Photogrammetry and Remote Sensing*, *167*, pp.418-431.

Yoo, C. (2017). Effect of water leakage in tunnel lining on structural performance of lining in subsea tunnels. *Marine Georesources & Geotechnology*, *35*(3), pp.305-317.

Yu, P., Wu, H., Liu, C. and Xu, Z. (2018). Water leakage diagnosis in metro tunnels by integration of laser point cloud and infrared thermal imaging. *The International Archives of the Photogrammetry, Remote Sensing and Spatial Information Sciences*, *42(3)*, pp.2167-2171.

Zan, Y., Li, Z., Su, G. and Zhang, X. (2016). An innovative vehicle-mounted GPR technique for fast and efficient monitoring of tunnel lining structural conditions. *Case Studies in Non-destructive Testing and Evaluation, 6*, p.63-69.

Zhu, L. and Hyyppa, J. (2014). The use of airborne and mobile laser scanning for modelling railway environments in 3D. *Remote Sensing*, *6*(4), pp.3075-3100.

Zoeteman, A. (2001). Life cycle cost analysis for managing rail infrastructure. *European Journal of Transport and Infrastructure Research*, *1*(4), p. 391-413.